ABSTRACT

Title of Dissertation: ULTRA-LOW-LOSS SILICON NITRIDE WAVEGUIDE GRATINGS AND THEIR APPLICATIONS IN ASTROPHOTONICS

Yiwen Hu, Doctor of Philosophy, 2020

Dissertation Directed By: Professor Mario Dagenais
Department of Electrical and Computer Engineering

Recent progresses in silicon photonics have enabled many exciting applications in data communications, sensing, quantum information, and astrophotonics. Astrophotonics is an emerging research field which aims to apply the fast-evolving photonics technology to astronomy. Compared with the silicon-on-insulator (SOI) based silicon photonics, silicon nitride (SiN) based silicon photonics inherits many prominent characteristics such as CMOS compatibility and fabrication flexibility. Furthermore, SiN-based photonics excels in applications strongly associated with low loss level and wide transparent window. All these features are all very attractive for astronomical instrumentation. Typical applications of astrophotonic components are photonic lanterns, frequency combs, highly selective optical filters, and on-chip

spectroscopy. Specifically, the scope of this dissertation covers the astrophotonic filters and spectroscopy, from the design, fabrication to characterization. The photonic components which they are based on are ultra-low-loss SiN waveguide and waveguide gratings.

The fabrication techniques of ultra-low-loss SiN photonic devices will be first discussed. I will demonstrate several methods to reduce the waveguide and grating losses, including the optimization of SiN deposition, e-beam lithography, etching, cladding oxide deposition, and thermal annealing. In the third chapter, an efficient waveguide characterization approach is developed for measuring losses in on-chip waveguides. This approach is based on measuring the transmission of a Fabry-Perot Bragg grating cavity formed by two highly reflective and low loss Bragg grating mirrors. In the fourth chapter, I will discuss on the design and characterization of a high performance integrated arbitrary filter from 1450 nm to 1640 nm. The filter's target spectrum is chosen to suppress the night-sky OH emission lines, which is critical for ground-based astronomical telescopes. To reduce the device footprint, the designed 50-mm-long 55-notch filter is mapped to a compact spiral waveguide. The last topic of this dissertation is on-chip spectroscopy with arrayed waveguide grating (AWG). Different with conventional AWG used in WDM telecommunication applications, this astrophotonic spectroscopic AWG particularly needs a large free spectral range (FSR) and a flat focal-plane for the following up free-space cross disperser. The basic principle and preliminary experimental results of AWG will be first presented, followed by discussions of two AWG designs with flat output-plane.

Ultra-Low-Loss Silicon Nitride Waveguide Gratings and Their Applications in Astrophotonics

by

Yiwen Hu

Dissertation submitted to the Faculty of the Graduate School of the
University of Maryland, College Park, in partial fulfillment
of the requirements for the degree of
Doctor of Philosophy
2020

Advisory Committee:
Professor Mario Dagenais, Chair
Professor Edo Waks
Professor Martin Peckerar
Professor Miao Yu
Professor Sylvain Veilleux, Dean's Representative

© Copyright by
Yiwen Hu
2020

Preface

The basis for this dissertation originally stemmed from the Keck Foundation research proposal written by Prof. Veilleux, Prof. Dagenais, and several other scientists in NASA Goddard and Australia in 2013. It is aiming to advance astronomical instrumentation for ground and space telescopes. Since 2017, this project is followed up by the grants from National Science Foundation and NASA. With the combined efforts in Dagenais group in UMD ECE and Veilleux group in UMD Astronomy, many exciting accomplishments have been achieved in the past years. I am really honored and proud to be able to participate in most of these works.

A publication list is attached in the next page, which includes all journal publications related with this dissertation. The main results in Chapter 2, Chapter 3 and Chapter 4 are presented in [1] and [2] of the list. Chapter 5 includes the main unpublished results on AWG spectrometer.

Publication List

[1] **Y. Hu**, S. Xie, J. Zhan, Y. Zhang, S. Veilleux and M. Dagenais, "Integrated Arbitrary Filter with Spiral Gratings: Design and Characterization," *J. Light. Technol.*, doi: 10.1109/JLT.2020.2992758.

[2] **Y.-W. Hu**, Y. Zhang, P. Gatkine, J. Bland-hawthorn, S. Veilleux, and M. Dagenais, "Characterization of low loss waveguides using Bragg gratings," *IEEE J. Sel. Top. Quantum Electron.*, vol. 24, no. 4, pp. 1–8, 2018.

[3] S. Xie, Y. Zhang, **Y. Hu**, S. Veilleux, and M. Dagenais, "On-chip Fabry-Perot Bragg grating cavity enhanced four-wave mixing," *ACS Photonics*, vol. 7, no. 4, pp. 1009–1015, 2020.

[4] J. Zhan, Y. Zhang, **Y. Hu**, S. Xie, S. Veilleux, and M. Dagenais, "Investigation of backward cladding-mode coupling in Bragg gratings implemented on a Si3N4 waveguide platform," *J. Opt. Soc. Am. B*, vol. 36, no. 12, p. 3442, 2019.

[5] S. Xie, J. Zhan, **Y. Hu**, Y. Zhang, S. Veilleux, J. Bland-Hawthorn, and M. Dagenais, "Add-drop filter with complex waveguide Bragg grating and multimode interferometer operating on arbitrarily spaced channels," *Opt. Lett.,* vol. 43, no. 24, p. 6045, 2018.

[6] P. Gatkine, S. Veilleux, **Y. Hu**, J. Bland-Hawthorn, and M. Dagenais, "Arrayed waveguide grating spectrometers for astronomical applications: new results," *Opt. Express*, vol. 25, no. 15, pp. 17918-17935, 2017.

[7] T. Zhu, **Y. Hu**, P. Gatkine, S. Veilleux, J. Bland-Hawthorn, and M. Dagenais, "Ultrabroadband high coupling efficiency fiber-to-waveguide coupler using

Si3N4/SiO2 waveguides on silicon," *IEEE Photonics J.*, vol. 8, no. 5, pp. 1–12, 2016.

[8] T. Zhu, **Y. Hu**, P. Gatkine, S. Veilleux, J. Bland-Hawthorn, and M. Dagenais, "Arbitrary on-chip optical filter using complex waveguide Bragg gratings," *Appl. Phys. Lett.*, vol. 108, no. 10, p. 101104, 2016.

Acknowledgements

First of all, I would like to express my sincere gratitude to my advisor Prof. Mario Dagenais and co-advisor Prof. Sylvain Veilleux for their continual help and guidance during the course of my PhD. They have inspired me to realize the power of concentration and critical reasoning. My projects would not have been completed without their instructions and encouragement. I would also like to thank my other committee members, Prof. Martin Peckerar, Prof. Edo Waks and Prof. Miao Yu for their assistance and suggestions on my research and dissertation.

I am very thankful to Tiecheng Zhu and Yang Meng, who are our group's PhD alumni and have helped me considerably in the first two years of my PhD career. I also need to thank Yangi Yao and Wei-Lun Hsu who have helped a lot on the fabrication process.

Yang Zhang, Shengjie Xie and Jiahao Zhan are my PhD colleagues and have worked closely with me from generating research inspirations to experimental characterization. They have always been sources of invaluable discussions and I am extremely grateful. Pradip Gatkine and I started the work on AWG together, and he can always provide insightful ideas. I also need to thank Feifei Chen, a visiting PhD student from China, for her preliminary work on Bragg grating cavities. To Joey Brock, Niloy Acharjee and Trisha Chakraborty, it is always a great pleasure to discuss with you on topics of SOI Bragg gratings and optical phased array.

For my nano-fabrication work, the staff of the Maryland NanoCenter was very helpful. I am grateful to John Abrahams, Tom Loughran, Jonathan Hummel, and Mark

Lecates. I would also like to thank Dr. Jiancun Rao for his patient guidance on SEM experiments.

Finally, I want to express deep thanks to my family. I thank my parents for their continuous and unparalleled love, despite the long distance between us. My special thanks go to my wife, Jing Men, for her understanding and persistence in the past few years while we are both pursuing for PhD degree in different locations. She has always been helping me get through difficult times in the most positive way.

Table of Contents

ABSTRACT i

Preface ii

Publication List iii

Acknowledgements v

Table of Contents vii

List of Tables x

List of Figures xi

Chapter 1: Introduction 1

1.1 Ultra-Low-Loss Si3N4 Waveguide and Waveguide Gratings 2

1.2 Astrophotonics: The Application of Integrated Photonics to Astronomy 5

Chapter 2: Silicon Nitride Waveguide Design and Fabrication 8

2.1 Waveguide and Fiber-to-Chip Coupler Design 8

2.2 Overview of the Fabrication Process 11

2.3 LPCVD Si_3N_4 12

2.4 e-Beam Lithography 13

2.4.1 20 kV EBL with Resist PMMA 13

2.4.2 100 kV EBL with Resist ma-N 2403 15

2.4.3 100 kV EBL with Resist ZEP520A 17

2.5 Ion-Coupled-Plasma (ICP) Reactive-Ion Etching (RIE) 18

2.6 PECVD Cladding SiO_2 19

2.6.1 Advantages and Challenges of PECVD SiO_2 Film 19

2.6.2 Silane Recipe 20

2.6.3 Standard TEOS Recipe 22

2.6.4 Optimized TEOS Recipe with Silane Oxide Cover 25

2.6.5 Further Discussions on PECVD TEOS 26
2.7 Thermal Annealing 27
2.8 Summary 30

Chapter 3: Integrated Waveguide Characterization with Grating Cavities 32
3.1 Bragg Grating Modeling and Design 32
3.1.1 π-Phase-Shifted Bragg Grating 34
3.1.2 Bragg Grating Fabry-Perot Cavity 35
3.1.3 Loss Terms in the Model 35
3.2 Experimental Results 36
3.2.1 π-Phase-Shifted Bragg Grating 36
3.2.2 Bragg Grating Fabry-Perot Cavity 38
3.2.3 Record Loss Reduction with Optimized Fabrication 41
3.3 Further Discussions 42
3.3.1 Lower Limit of Measurable Waveguide Loss 42
3.3.2 Lower κ Grating 44
3.3.3 Loss Measurement Bandwidth 44
3.4 Summary 45

Chapter 4: Arbitrary Spiral Complex Filter for OH Emission Suppression 46
4.1 Background 46
4.2 Layer Peeling Algorithm 49
4.2.1 Discrete Layer Peeling (DLP) 50
4.2.2 Continuous Layer Peeling (CLP) 51
4.3 Optimization on Discrete Layer-Peeling 52
4.3.1 Frequency Domain and Time Domain DLP 52
4.3.2 Non-Uniformity Issue 54
4.4 Spiral Complex Grating Design 59
4.4.1 Spiral Curve Geometry 59
4.4.2 Mode Index's Sensitivity on Waveguide Width 61
4.4.3 Critical Bending Radius 62
4.5 Implementation in MATLAB and FIMMPROP 63

4.5.1 Key Algorithms for Inverse Scattering and Direct Scattering 63
4.5.2 Spiral Complex Structure Realization 65
4.5.3 Reducing Grating Assembly Time.. 68
4.6 Experimental Results 69
4.6.1 Device Characterization.. 69
4.6.2 Effect from Cladding Mode Coupling 73
4.6.3 Effect from Waveguide Dispersion... 74
4.6.4 Effect from Fabrication Imperfections.. 75
4.7 Summary 76

Chapter 5: On-chip Astronomical Spectroscopy with Arrayed Waveguide Gratings 78
5.1 Basic Principles of AWG... 78
5.2 Theoretical Framework 80
5.3 Experiment Results of Rowland-Type AWG 82
5.4 Flattened Rowland-Type AWG 85
5.4.1 Comparison of the Standard and Flattened Rowland AWG 85
5.4.2 Effect of Focal-Plane Offset 87
5.5 Three-Stigmatic-Point AWG 89
5.5.1 Aberration Study of Rowland-Type AWG 89
5.5.2 Three-Stigmatic-Point AWG 90
5.6 Summary 94

Chapter 6: Conclusions and Outlook 95

Bibliography 98

List of Tables

Table 3-1 PSBG (centered at 1629 nm) fine fitting results for Figure 3.2. [a] The center peak intensity is the maximum transmission the center peak can reach. The center peak intensity will be exactly 0 dB if both the grating loss α_g and cavity loss α_c are 0. [b] The linewidth measured in experiment is 2.2 pm.... 38

Table 3-2 BGFP (centered at 1625.8 nm) fine fitting results for Figure 3.4. [a] Modeling uses α_g = 0.41 dB/cm. [b] The experimental linewidth is 1.6 pm. 41

Table 3-3 12 mm BGFP Modeling Results Related with Figure 3.6 [a] Modeling uses grating loss 0.1 dB/cm. 43

Table 4-1 Grating notch depth differences caused by dispersion. [a] denotes the widths of narrow – wide part of a simple Bragg grating. 74

List of Figures

Figure 1.1 The set up for the on-sky tests of the FBG OH emission filter. A multi-mode fiber is used to collect the starlight; followed by a photonic lantern to separate the multi-mode light signal into several single mode fibers. Complex FBGs will filter out the OH emission lines before they can enter a spectrograph. Figure reproduced with permission from ref. [24], © 2011 NPG. 6

Figure 2.1 (a) Waveguide illustration for a cross section dimension 2 μm × 100 nm. (b) TE mode profile at 1550 nm. (c) TM mode profile at 1550 nm. 8

Figure 2.2 Coupling efficiency with varying coupler waveguide width. Simulated for TE and TM modes at 1550 nm for (a) UHNA3 fiber and (b) PM 1550-XP fiber. 9

Figure 2.3 Mode profile for coupler waveguide dimension 100 nm × 700 nm. (a) TE mode. (b) TM mode. 10

Figure 2.4 Summary diagram of the fabrication process. 11

Figure 2.5 SEM of device patterned by PMMA lift-off recipe. (a) Sub-micro waveguide showing large stitching error in the vertical direction. (b) Rectangular Bragg gratings with width 5-7 μm. Horizontal stitching error can be observed. (c) Tilted view of an etched 2 μm (W) x 100 nm (H) waveguide showing rough sidewall. (d) Top view of a phased shifted grating, showing that the boundary is not very smooth. 14

Figure 2.6 SEM of device patterned by ma-N recipe. SEM of two fabricated devices. (a) A segment of the spiral CWBG. (b) Zoomed-in view of (a). (c) Tilted and further zoomed-in view of (a). (d) Tilted view of another uniform grating used as an FPBG mirror. 16

Figure 2.7 SEM of device patterned by ZEP recipe. (a) Tilted view of a grating with width variation 4um-7um (b) Tilted view of three 250 nm wide waveguides with 250 nm spacing. Etching depths are all 100 nm. 17

Figure 2.8 Illustration of the bending waveguide design for measuring linear propagation loss. We made five waveguides on the chip with length difference of 0, 7, 14, 21, and 28 mm. The corresponding loss results are shown in Fig. 2.9. 21

Figure 2.9 Linear propagation loss of Si_3N_4 /SiO_2 waveguide, extracted from the sample in Figure 2.8. The error bars are shown as the shaded area. 22

Figure 2.10 Transmission of a phase-shifted Bragg grating fabricated with 2 μm PECVD TEOS top cladding. They are measured 1 hour (a) and 12 hours (b) after the deposition process is finished. 24

Figure 2.11 Transmission of a PSBG device fabricated with 5 μm TEOS oxide top cladding covered by 1 mm silane oxide. Measured 1 hour (a) and 17 hours (b) after the deposition. 25

Figure 2.12 Waveguide propagation loss for TE mode after annealing. The measurement is done with the same sample in Figure 2.9, but after 2-hour annealing at 1150C. The error bars are shown as the shaded area............ 28

Figure 2.13 SEM of a 2.7 – 3.2 μm Bragg grating before (a) and after (b) 1-hour 1150 C annealing. Images courtesy of Shengjie Xie. 29

Figure 2.14 Measured spiral losses for two spiral waveguides with 500 μm inner radius (black) and 750 μm inner radius (red). The 750 μm inner radius sample is annealed in 1150C. implies N-H content is very low in TEOS films. 30

Figure 3.1 (a) Illustration of the Bragg grating design. For PSBG, cavity length L_0=Λ ~ 550 nm. For BGFP, we made the cavity length L_0 = 1 mm, 3 mm and 6 mm. (b) Tilted view of the 2 μm ×100 nm straight waveguide. (c) Top view

of the λ/4 PSBG; the π phase shifted part can be recognized in the figure center. 33

Figure 3.2 PSBG grating experimental (black solid line) and theoretical fitting (dashed lines) results. In (a)(c), the wavelength range is 4 nm. In (b)(d), the wavelength range is 20 pm. Fitting parameters: (1558 nm) $n_1 = 1.47584$, $n_2 = 1.47691$; $\Delta n = 0.00107$, $\kappa = 10.81$ cm^{-1}, stopband width $\Delta\lambda = 0.563$ nm. (1629 nm) $n_1 = 1.47171$, $n_2 = 1.47273$; $\Delta n = 0.00102$, $\kappa = 9.85$ cm^{-1}, $\Delta\lambda = 0.561$ nm. 37

Figure 3.3 Experimental and simulation curves for Bragg grating cavity with length (a) 1 mm, (b) 3 mm and (c) 6mm. For the blue simulation curve, we use grating loss 0.41 dB/cm and cavity (straight waveguide) loss 0.24 dB/cm. The wavelength range is 4 nm in all four panels. The y axes are set to be the same. Fitting parameters: $n_1 = 1.47860$, $n_2 = 1.47979$; $\Delta n = 0.00119$, $\kappa = 11.5$ cm^{-1}, $\Delta\lambda = 0.649$ nm. 39

Figure 3.4 The enlarged figure for BGFP transmissions. Red, blue and green lines denotes cavity loss $\alpha_c = 0.14$ dB/cm, 0.24 dB/cm and 0.34 dB/cm. Grating loss α_g is set as 0.4 dB/cm. (a) 1 mm cavity with linewidth 2.0 pm. (b) 3 mm cavity with linewidth 1.8 pm. (c) 6 mm cavity with linewidth 1.6 pm. Note that the legend in (a) also holds for (b) and (c). The x range are all 8 pm, y axes are set to be the same. 40

Figure 3.5 Waveguide and grating loss characterization from device with optimized fabrication. The grating loss is extracted as 0.26 dB from (a) π-phase shift FPBG. The waveguide loss is extracted as 0.10 dB from (b) 6mm FPBG. (c),(d) are zoomed-in views of (a),(b). 41

Figure 3.6 BGFP simulation to demonstrate its potential for measuring very low loss coefficients. We keep the grating loss $\alpha_g = 0.1$ dB/cm, and set the cavity loss $\alpha_c = 0$, 0.001 and 0.01 dB/cm. 43

Figure 4.1 Spectrum atlas of the night-sky OH emission. [36] 47

Figure 4.2 Validation results for grating designs with (a) DLP $\Delta = 4$ μm, (b) CLP $\Delta\text{CLP} = \Delta/2 = 2$ μm, and (c) CLP $\Delta\text{CLP} = \Delta/4 = 1$ μm. The target spectra (red dotted line) are the same: 55 notches with -20 dB depth. All transmissions are validated with the CMT model.................................... 51

Figure 4.3 Comparison of *t*-DLP and *f*-DLP for an arbitrary filter design with 15dB/30dB alternating notch depths. (a) DLP layer size is 4 μm. (b) DLP layer size is 8 μm. Grey ovals indicate the irregular reconstructed notches in the *t*-DLP algorithm. Both *t*-DLP and *f*-DLP have the non-uniformity issue. 53

Figure 4.4 *f*-DLP modified by a sinc function for a target spectrum with (a) alternating 15dB/30dB notch depths and (b) uniform 30dB notch depths. Validation plots show that the modified *f*-DLP does not have the non-uniformity issue. 58

Figure 4.5 Illustration of a spiral complex grating. The top panel shows the index profile of the 50 mm grating. The bottom panel shows the whole grating, assembled by a series of layers with different coupling coefficient q_i....... 60

Figure 4.6 (a) Mode index study for waveguides with 100 nm and 300 nm thicknesses. (b) Simulated bending loss in TE and TM modes at 1550 nm for 3 μm x 100 nm and 2 μm x 100 nm waveguides.. 61

Figure 4.7 (a) Console commands for the 726-th grating section executed in FIMMPROP. (b) Plan view illustration of the section joint showing tilt angle θL and θR. (c) Assembly processing time for each grating layer (section). 67

Figure 4.8 SEM of fabricated grating segments defined by the sampled discrete rectangles (a) and continuous sinusoidal expression (b)............................ 68

Figure 4.9 SEM of two fabricated devices. (a) A segment of the spiral CWBG. (b) Zoomed-in view of (a). (c) Tilted and further zoomed-in view of (a). (d) Tilted view of another uniform grating used as an FPBG mirror. 70

Figure 4.10 (a) Experimentally measured transmission of a reference spiral and a CWBG spiral with 3 μm average width. (b) 2 μm average width CWBG with 55-notch design showing that the deepest notches lie near the bandwidth center. (c) 3 μm average width CWBG with 43-notch design showing that the deepest notches are shifted to the right from the bandwidth center. Note that the notches in (b) and (c) are all normalized to 0 dB to compare notch depths. 71

Figure 4.11 The study on cladding-mode coupling. Transmission of (a) 100 nm thick Si_3N_4 with 2 – 2.2 μm wide single-notch grating; (b) 100 nm thick Si_3N_4 with 2 – 2.4 μm wide single-notch grating; (c) 60 nm thick Si_3N_4 with 4 – 6 μm wide single-notch grating; (d) 7-notch CWBG with FWHM ~ 0.8 nm. 72

Figure 4.12 Normalized transmission of a well-defined notch and a disturbed notch. (a) The zoomed-in view of a single notch in Figure 4.10(a). (b) The transmission of a 2 μm width spiral CWBG with fabrication errors. 75

Figure 5.1 Layout of a typical AWG. Figure reproduced with permission from ref. [91], © 1996 IEEE. 79

Figure 5.2 Illustration of the geometry design of an $N \times N$ AWG. Figure reproduced with permission from ref. [95], © 2001 IEEE. 80

Figure 5.3 FPR region in a Rowland-type AWG. Figure reproduced with permission from ref. [91], © 1996 IEEE. 82

Figure 5.4 (a) A typical AWG design with dimension 2 μm × 100 nm. (b-d) Optical images of the fabricated AWG as designed in (a). Images are taken after ICP etching and before PECVD SiO_2 deposition.. 83

Figure 5.5 TE and TM of AWG transmission for the AWG in Figure 5.2. The waveguide dimension is 2 µm x 100 nm. 3-dB channel width is measured as 7nm.. 84

Figure 5.6 FPR layout of (a) a standard Rowland AWG and (b) a flattened Rowland AWG. 85

Figure 5.7 AWG simulation for (a) a Rowland-type AWG and (b) a flat focal-plane AWG. The first channel Ch-1 and the last channel Ch-21 are labeled. The two transmissions are very similar with negligible differences................ 86

Figure 5.8 AWG simulation for a flat focal-plane AWG with shift (a) 10 µm and (b) 20 µm. The defocus aberration causes broader channel width and larger crosstalk. 87

Figure 5.9 AWG simulation for a flat focal-plane AWG with shift (a) -10 µm and (b) -20 µm. 88

Figure 5.10 Aberration-free focal positions of the Rowland-type AWG. The aberration-free focal positions all fall on the Rowland curve..................................... 90

Figure 5.11 Aberration-free focal positions of the Rowland-type AWG and 3-stigmatic-point AWG. 91

Figure 5.12 (a) Grating curve comparison in X-Y coordinate system. (b) Focal positions comparison for the center wavelength of the 21 wavelength channels...... 92

Figure 5.13 Comparison of the arrayed waveguide properties for 3-stigmatic-point (blue) and Rowland (black) AWG. (a) The distance between neighboring arrayed waveguide, measured as the curve length along $u(w)$. (b) The extra length for each arrayed waveguide, in excess of the standard Rowland length difference $\Delta L = m\lambda c/n$wg. 93

Chapter 1: Introduction

A challenge in today's photonics integration circuits (PIC) is to incorporate various functionalities together while balancing the performance and footprint. Among different IPC platforms, silicon photonics is one of the most prominent in recent years [1]. The main advantages of silicon photonics platform are the CMOS compatible fabrication and high index contrast, especially when compared with doped silica glass platform. For the typical silicon-on-insulator wafer chip, electro-optic modulators and germanium photodetectors can be monolithically integrated. By using wafer bonding, III–V materials can also be integrated, which will help to achieve on-chip optical amplification and lasing. These features, coupled with the high refractive index contrast between silicon and cladding oxide, can enable the manufacturing of densely integrated electronic photonic components at low costs and high volumes [2]–[4]. SOI is also an attractive platform for nonlinear optics, thanks to its large Kerr nonlinearity. However, its relatively high on-chip loss and two-photon absorption (TPA) in the telecommunication band also bring challenges in the losses, crosstalk, and fabrication tolerance, which limit their practical implementations.

In recent years, silicon nitride (SiN) based silicon photonics have attracted a lot of attention. It is similar with SOI in many aspects, but replaces silicon with SiN as the device layer. SiN does not suffer from two photon and free carrier absorption over the telecommunication band. SiN photonic components are also less temperature sensitive owing to a thermo-optic coefficient that is about five times smaller than that of Si [5], [6]. Furthermore, the lower index contrast of Si3N4 waveguides with SiO2 compared

to Si waveguides reduces the waveguide losses due to sidewall roughness scattering. Till now, several groups have achieved ultra-low-loss < 0.01 dB/cm, and has demonstrated high quality factor Q > 10 million [7]–[11]. The optical transparent spectral range of SiN is much broader than silicon in the near-infrared and visible wavelength range, making it suitable for many other applications other than telecommunication, such as biosensing and frequency combs.

1.1 Ultra-Low-Loss Si3N4 Waveguide and Waveguide Gratings

Dielectric waveguide is the fundamental building block for PICs. The loss level of the waveguides could significantly affect the device performance in various applications. In the last decade, we have seen significant improvement for on-chip losses. Several groups have demonstrated low propagation loss waveguides [12]–[16]. In fact, losses as small as 0.1 dB/m and 0.9 dB/m have now been reported in weakly and strongly confined waveguides, respectively [8], [17], [18]. Ultra-low losses in long waveguides (> 1 m) have been measured using a coherent optical frequency domain reflectometry technique [17], [18]. The waveguides with losses less than 0.1 dB/m were fabricated by wafer bonding a thermal oxide layer as the upper cladding and resulted in a waveguide with ultra-low confinement and reduced scattering losses at the core-cladding interfaces [17]. Ring resonators with high quality factor $Q > 10^6$ have also been fabricated in low loss waveguides and often have been used to extract the loss coefficient in these waveguides [8], [14]. Applications of ultra-low loss waveguides are envisioned in optical gyroscopes[19], dispersion compensation[20], packet-switched networks [21], optical filters [22], optomechanical sensing [23]and in astrophotonics [24].

The term “waveguide gratings” in this dissertation exclusively refers to two type of devices: waveguide Bragg gratings (WBGs) and arrayed waveguide gratings (AWGs). Waveguide gratings play very important roles in PICs and their performances are strongly associated with the advancement of low-loss waveguide technology.

WBGs share many common characteristics with fiber Bragg gratings (FBGs). Since the discovery of photosensitivity in optical fibers [25], there has been great interest in the FBGs. The ability to inscribe Bragg gratings in these photosensitive fibers has revolutionized the field of telecommunications and optical fiber-based sensor technology. If these achievements can be transferred onto the integrated platform, it can potentially bring many benefits to the device footprint, performance, and cost. The waveguide Bragg grating structures is commonly achieved by physically corrugating the silicon waveguide. Besides the uniform Bragg gratings, there are also aperiodic (chirped) gratings [26], which displays a linear variation in the grating pitch, designed as chirp. There is also an even more complicated type of Bragg grating, termed as the complex waveguide Bragg grating (CWBGs) [22], [27], [28]. CWBGs usually have an algorithm determined, complex coupling coefficient profile to realize a spectrum with desired properties. These WBGs have been used to implement various functionalities such as dispersion compensation, filter, coupler, sensor. Based on the low loss WBGs, we can implement a type of resonator, we call it Fabry-Perot Bragg grating cavities (FPBG). One distinctive characteristic of WG resonators is that their photonic bands can be as flexible as photonic crystal cavities, while its Q can potentially match that of a ring cavity (> 10 million). With state-of-the-art technologies, up to several

centimeters long low-loss grating resonators can be fabricated with unprecedented quality.

Since Smit's invention in 1988 [29], AWG has soon become a key device in WDM optical communication systems. AWG is essentially a type of optical phased array. By controlling the phase relationship between the beams emitted by the individual elements of the array, the focal point of wavefront can be changed without mechanical movements. It has been used to perform functions such as wavelength (de)multiplexing, wavelength filtering, and optical routing. Emerging AWG applications include chemical and biological sensing, space-based sensing, optical coherence tomography, and spectroscopy [30]. This dissertation is focused on the adoption of AWG for on-chip spectroscopy. The main research targets for AWG spectrometers include low-loss, low crosstalk, high resolution, flat-top passband, and broad spectral range. Another unique target I will be studying on is the flat output focal plane, which differs from traditional AWG designs with a curved focal plane. This target is brought by the specific need of an ultra-broad spectral wavelength range, which is desired for astronomical spectroscopy. When light reaches the output focal plane, different grating orders needs to be further differentiated by a free space cross-dispersion set-up. A flat focal plane could minimize the optical aberration and helps to increase the detection capability of faint starlight. It can also facilitate the placement of 1-d detector array on the output facet, to form a fully chip-scale narrower band spectrometer.

1.2 Astrophotonics: The Application of Integrated Photonics to Astronomy

Astrophotonics lies at the interface of astronomy and photonics. In fact, the increased efficiency with which photons are collected by modern instruments has revolutionized the field of observation astronomy [31]. Over the past decade, astrophotonics is developing very fast in response to the ever-increasing demands of astronomical instrumentation. Most astronomical projects are photon-starved which means that insertion losses must be kept to the lowest possible level. The manipulation of faint light requires the optical components to achieve its theoretical limits within various harsh environment for either on ground or in space platforms.

Traditionally, optical telescope components used by astronomers are very complicated, expensive, and in many cases bulky [32], [33]. The design and construction of the next generation of astronomical instruments pose even bigger challenges. Simply scaling up existing technology leads to highly ineffective and costly instruments. The emerging of astrophotonics could advance the use of photonic technology in astronomy. However, there are still many challenges ahead. For example, for a given spectral band, astronomers usually seek to achieve a bandwidth $\Delta\lambda \sim \lambda$ that is beyond the reach of most photonic devices today.

In 2009, Joss Bland-Hawthorn has summarized some key areas related with astrophotonics [31]. Here I will discuss about three of them.

(i) Frequency combs for ultra-high precision spectroscopy to detect planets around nearby stars;

(ii) Ultrabroadband fiber Bragg gratings to suppress unwanted background;

(iii) Planar waveguides to miniaturize astronomical spectrographs.

Optical frequency combs provide equidistant frequency markers in the infrared, visible and ultraviolet, and can be used to link an unknown optical frequency to a radio or microwave frequency reference [34], [35]. Since their inception, frequency combs have triggered substantial advances in optical frequency metrology and precision measurements. In astronomy, the combination of a laser frequency comb with a Fabry–Perot filtering cavity has been suggested as a promising approach to achieve very high Doppler shift resolution. This can significantly help to search for extrasolar planets. More details in this area is beyond the scope of this dissertation.

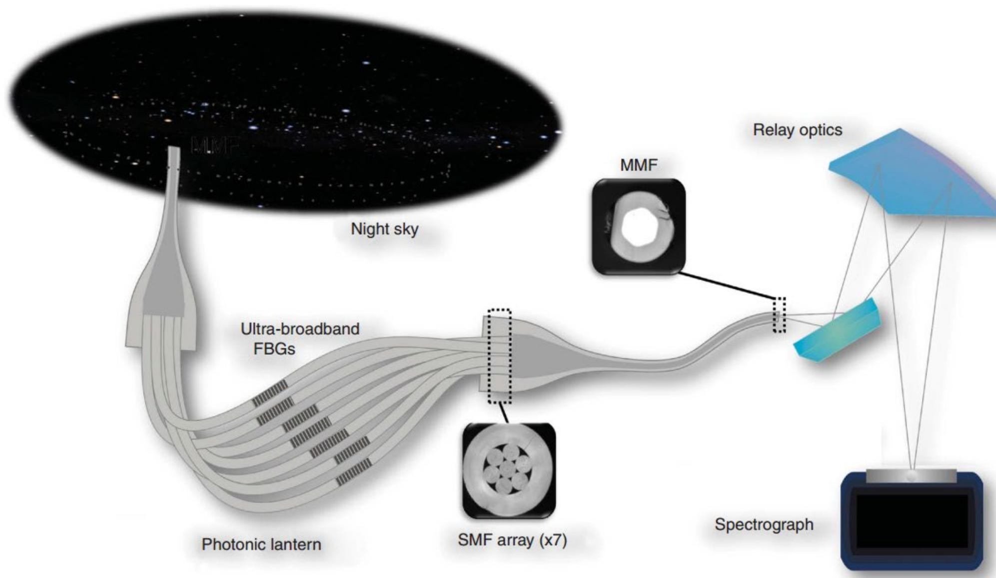

Figure 1.1 The set up for the on-sky tests of the FBG OH emission filter. A multi-mode fiber is used to collect the starlight; followed by a photonic lantern to separate the multi-mode light signal into several single mode fibers. Complex FBGs will filter out the OH emission lines before they can enter a spectrograph. Figure reproduced with permission from ref. [24], © 2011 NPG.

The extreme brightness and variability of the night sky at near infrared has been a long-lasting problem for on-ground astronomical observation [36]. These background emission lines mostly result from de-excitation of OH radicals in the Earth's

atmosphere. When astronomers use ground-based telescopes to collect the faint starlight from the universe, these OH emission lines will also enter the aperture of the telescope and limit its sensitivity and resolution. The astronomical community has long envisioned the prospect of selectively removing these lines, while retaining high throughput between them [24]. Traditionally, this type of filter has only been achieved with FBGs, as shown in Figure 1.1. They are characterized by the large spectral range, high rejection ratio, irregular notches, and narrow notch width. In Chapter 3, I will systematically study the approaches to implement them on an integrated platform with CWBGs, which can bring many benefits for the device performance, cost, and footprint.

Another promising application of photonics to astronomical instrumentation is the miniaturization of near-infrared (NIR) spectrometers for large ground- and space-based astronomical telescopes [37]–[39]. Currently, most astronomical spectrometers are based on discrete optical elements resulting in a costly and bulky design. Integrated photonic spectrometers, on the other hand, are cheaper to mass produce, more suitable for complex light manipulation and tuning, and much less susceptive to surrounding environment variations. My efforts on this topic will be presented in Chapter 5, with a focus on low-loss, broad spectral range, and flat-focal-plane AWG design.

Chapter 2: Silicon Nitride Waveguide Design and Fabrication

2.1 Waveguide and Fiber-to-Chip Coupler Design

Ultra-low-loss silicon nitride waveguide was first demonstrated using extremely thin (40 nm) SiN films [12], [17], which can be adopted for narrow-notch filters and reference cavities for laser stabilization. On the other end, the weakly guided optical modes and millimeter-scale bending radii make it challenging for compact photonic circuits or nonlinear applications. For AWGs, large bending radii of arrayed waveguides will make the device footprint to appreciably increase. For high *Q* ring resonators, weakly guide mode is also undesired for compact designs.

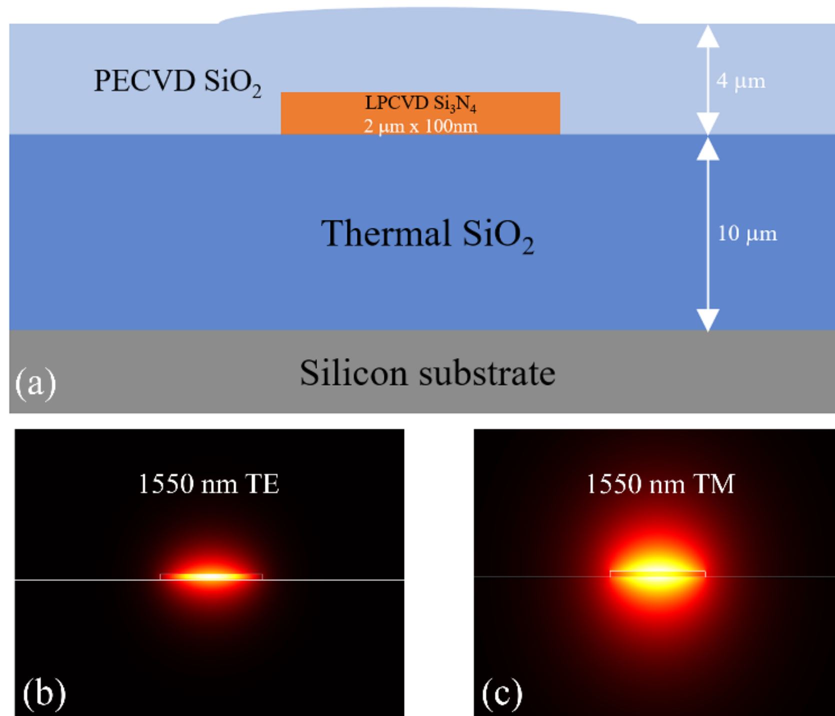

Figure 2.1 (a) Waveguide illustration for a cross section dimension 2 μm × 100 nm. (b) TE mode profile at 1550 nm. (c) TM mode profile at 1550 nm.

Thicker SiN waveguide design can help to put more components on a single chip as it has a higher mode confinement factor. However, it is more difficult to achieve ultra-low loss due to fabrication challenges and complexities [7], [8]. For the discussions in this chapter, I will focus on SiN waveguide with core thickness 100 nm, as shown in Figure 2.1. This core dimension is chosen for getting a reasonably confined mode with acceptable propagation loss. Additionally, 2 μm width is selected to ensure operation in single mode at a wavelength of 1.4 μm and above.

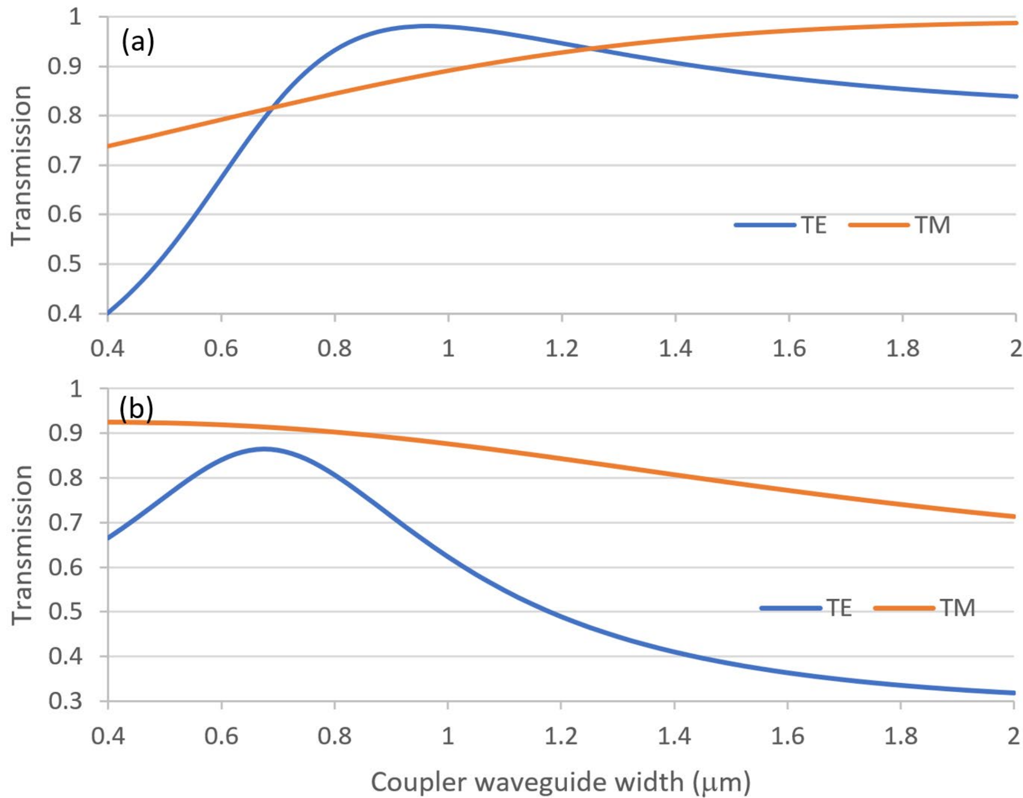

Figure 2.2 Coupling efficiency with varying coupler waveguide width. Simulated for TE and TM modes at 1550 nm for (a) UHNA3 fiber and (b) PM 1550-XP fiber.

Fiber-to-chip coupling is a critical aspect of integrated photonics. Although it has been extensively studied for over a decade [40], [41] there are still remaining challenges to achieve a low-loss and high-throughput coupling. There are two types of fiber coupling commonly used for silicon photonics, grating coupling, and edge

coupling. Grating coupling is a cleaving-free coupling technique, which can facilitate the fabrication process. However, edge coupling can provide a low-loss, high-bandwidth, and polarization-independent optical connection. In our group, we use an edge coupler scheme which employs a reverse taper with a coupler waveguide to achieve ultra-high coupling efficiency. Theoretical and experimental demonstration of this scheme are presented in our previous paper [42], which shows a coupling efficiency over 90% for a single facet.

In Figure 2.2, we simulate the coupling efficiency for TE and TM mode with polarization maintaining fiber Thorlabs PM 1550-XP and high NA fiber Thorlabs UHNA3. There are two types of fiber we mainly use for fiber coupling. Although the TM mode's coupling efficiency is quite decent, the ultra-high bending loss limits its usage for 100 nm SiN device. PM fiber's main advantages are its polarization purity and coupling position tolerance (because of large fiber mode size). To achieve ultra-high coupling efficiency, however, UHNA3 fiber is the better choice. For coupling at wavelength of 1.55 μm, the optimal coupler width is about 900 nm for UHNA3 and 700 nm for PM fiber. In experiment, these values might slightly differ.

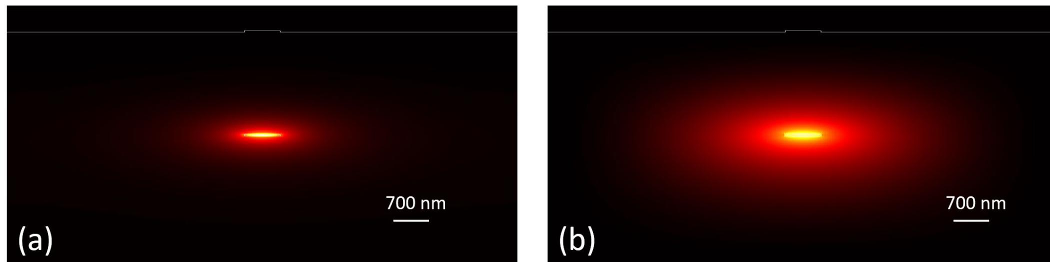

Figure 2.3 Mode profile for coupler waveguide dimension 100 nm × 700 nm. (a) TE mode. (b) TM mode.

The mode profiles of TE and TM modes for a coupler dimension of 100 nm × 700 nm are shown in Figure 2.3. Both are weakly confined, especially for the TM mode.

The large mode size makes highly efficient fiber coupling possible. Below are the specs of the two fibers at 1550 nm, provided by Thorlabs.

PM 1550-XP

core (cladding) diameter: 8.5 (125) μm

core (cladding) index: 1.449393 (1.444023)

UHNA3

core (cladding) diameter: 1.8 (125) μm

core (cladding) index: 1.49359 (1.45129)

2.2 Overview of the Fabrication Process

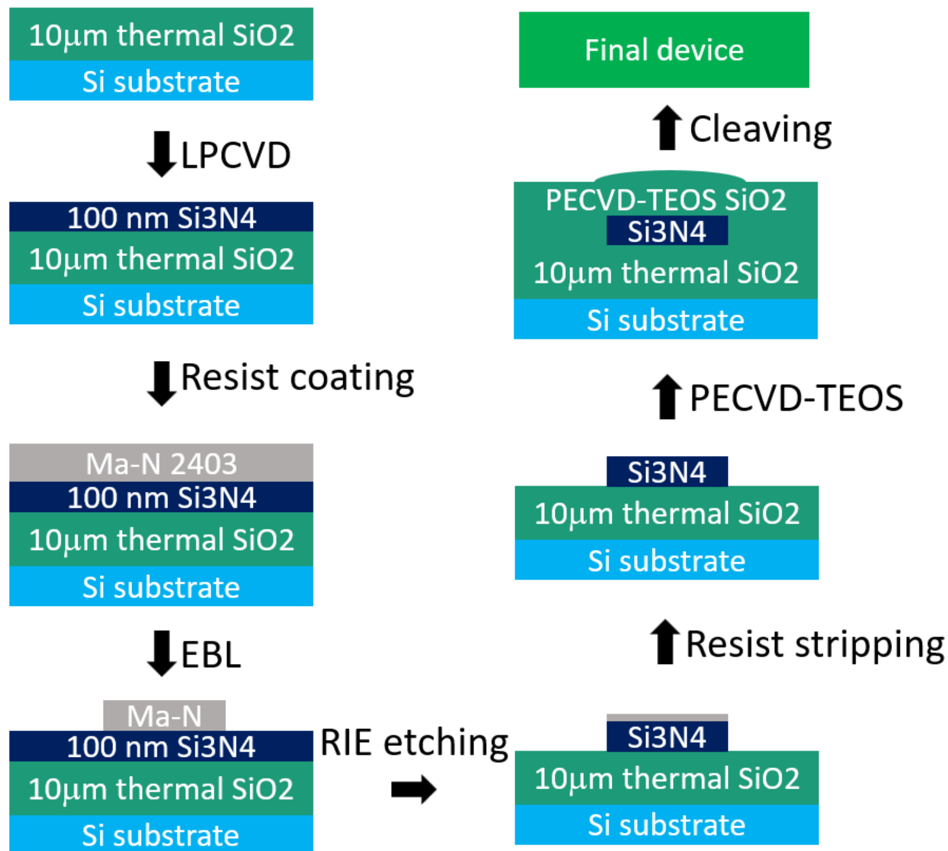

Figure 2.4 Summary diagram of the fabrication process.

The starting step of the fabrication is to thermally grow 10 μm thick SiO_2 on top of a silicon wafer, which can effectively reduce the substrate leakage to the silicon substrate. The next step is to deposit 100 nm LPCVD Si_3N_4 as the device layer. If using negative e-beam resist, we just need to perform the e-beam lithography and use the developed resist as the etching mask. If using positive e-beam resist, we need an extra lift-off process after EBL and form a metal mask for etching. Afterwards, we etch out the pattern with reactive ion etching (RIE). Subsequently, we strip the resist or metal mask, and deposit the top cladding SiO_2 with PECVD. The final step is to cleave the sample on the input and out ends for fiber edge coupling. The rest of this chapter will discuss optimization strategies for these individual steps to reducing the SiN waveguide losses.

2.3 LPCVD Si_3N_4

To obtain low loss SiN waveguides, the capability to deposit SiN film with high quality is necessary. In standard CMOS processes, SiN can be deposited either by plasma-enhanced chemical vapor deposition (PECVD) or by low pressure chemical vapor deposition (LPCVD). A crack-free SiN film with several um thickness can be grown by PECVD at a temperature below 500 C. The gas mixture used is usually SiH_4, NH_3 and N_2. The challenge for the PECVD SiN film prepared by PECVD is its large intrinsic absorption loss near 1.5 um due to N-H bond, which is formed during the deposition [43]. LPCVD can provide SiN film with good uniformity both in thickness and material quality. Although there exist issues such as high stress, slow growth rate and high deposition temperature, it is still the most popular method for low loss platforms.

The source gases used in LPCVD are dichlorosilane (SiH_2Cl_2, or DCS) and ammonia (NH_3). The gas ratio between DCS and NH_3 could significantly affect the film stress and the material absorption, and there is a tradeoff between these two material properties [44]. For example, low-stress SiN films can be grown using a large DCS/NH_3 ratio with a large thickness, but such films usually have a high hydrogen content, similar with what is observed in PECVD SiN. Decreasing the DCS to NH_3 ratio can reduce the N-H content, but the stress of the film increases significantly.

These two types of LPCVD SiN are experimentally demonstrated with the Tystar CVD furnace in the Maryland NanoCenter. The high DCS/NH_3 ratio type corresponds to the low stress nitride recipe. The LPCVD parameters are set as: chamber pressure 250 mT; DCS flow rate 50 sccm; NH_3 flow rate 10 sccm; temperature 835 C. The optical waveguide loss turns out to be too high to give a meaningful optical measurement result. The low DCS/NH_3 ratio SiN is generally used for stoichiometric Si_3N_4 deposition. The LPCVD parameters are set as: chamber pressure 250 mT; DCS flow rate 20 sccm; NH_3 flow rate 60 sccm; temperature 770 C. The deposition rate is only 2.5 nm/min with this recipe, but ultra-low waveguide loss can be achieved.

2.4 e-Beam Lithography

2.4.1 20 kV EBL with Resist PMMA

For photonic research purposes, e-beam lithography (EBL) is the preferred fabrication method because of its accuracy and fast prototyping capability. A conventional EBL recipe I have tried is to use 950PMMA A2 or 495PMMA A4 (MicroChem) positive-tone resist with 20kV Raith e-Line e-beam system. After e-

beam exposure and development, a thin (10 - 20 nm) layer of Chromium (Cr) is deposited on the chip surface with an Angstrom NexDep Ebeam evaporator. Afterwards we can form a reverse Cr mask with a lift-off process using Remover PG.

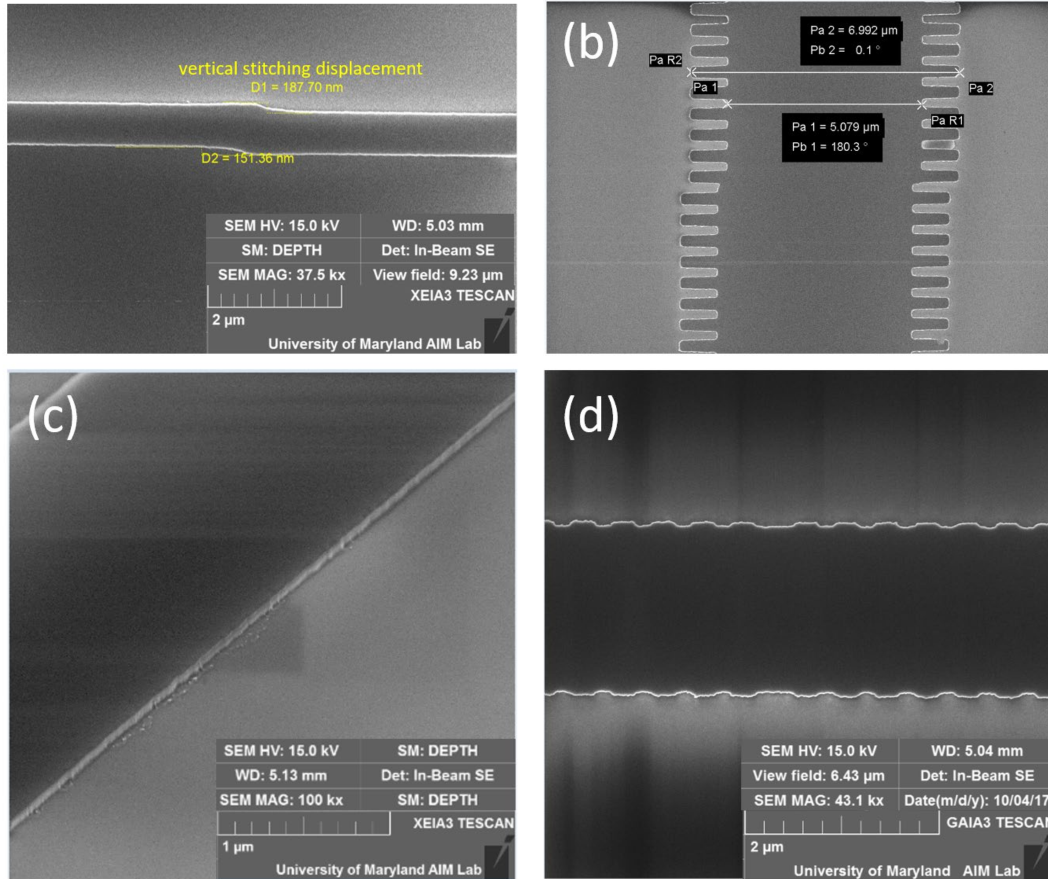

Figure 2.5 SEM of device patterned by PMMA lift-off recipe. (a) Sub-micro waveguide showing large stitching error in the vertical direction. (b) Rectangular Bragg gratings with width 5-7 µm. Horizontal stitching error can be observed. (c) Tilted view of an etched 2 µm (W) x 100 nm (H) waveguide showing rough sidewall. (d) Top view of a phased shifted grating, showing that the boundary is not very smooth.

This process is quite successful for our early demonstrates of SiN waveguides and gratings [22], [42], [45]. However, it sometimes suffers from large stitching error between neighboring EBL writing fields, as seen in Figure cannot deliver ultra-smooth waveguide boundaries, as shown in Figure 2.5. There are two main reason which introduce this roughness. One reason is that the 20 kV EBL system cannot give

electrons high enough momentum to define high resolution patterns; the other reason is that the PMMA + Cr lift-off process tends to leave particles near the structure, which can be clearly seen from Figure 2.5(c).

2.4.2 100 kV EBL with Resist ma-N 2403

To improve the EBL quality, we adopted the 100 kV Elionix ELS-G100. Higher voltage can bring higher resolution and higher patterning speed. Besides, the stitching error is also substantially reduced, usually not observable by SEM any longer. We also use a negative-tone resist ma-N 2403 (Micro Resist Technology). By using negative resist, we do not need to use the lift-off process anymore. It is worth nothing here that there are some other high-resolution negative resist options other than the ma-N 2400 series. For example, Hydrogen-silsesquioxane (HSQ) is an inorganic, negative-tone resist with high resolution and ability to form a thick film. In fact, HSQ is generally regarded the highest resolution EBL resist, which can routinely demonstrate <10 nm resolution. Once exposed to the e-beam, HSQ is similar to SiO2 which makes it a good hard mask for Si or SiN etching. For photonic applications to our concern, which requires a large patterning area, the main issue for HSQ is its high dosage. With 100 keV energy of electron beam, the patterning requires exposure dose between 2000 and 8000 $\mu C/cm^2$, which is 10-20 times the optimal dosage for ma-N 2400 series resist. As a result, it is impractical to use HSQ in our experiments.

Below I list the standard EBL we use for ma-N 2403.

Preparation:

1) Spin coating ma-N 2403 for 30 s with 3000 rpm
2) Spin coating aquaSAVE (probably necessary) for 30 s with 3000 rpm

(aquaSAVE is an antistatic agent manufactured by Mitsubishi Chemical. It is used to prevent electrons from accumulating on the resist surface during electron beam lithography.)

3) Pre-bake for 60s with 95-105C

EBL:

1) 100 kV EBL with dosage 300-600 μc/cm^2

2) Rinse for 30s with DI water

3) Rinse for 45s with ma-D 525 developer

4) Rinse for 30s with DI water

5) Immerse in water for 5 mins

6) Blow dry with N_2

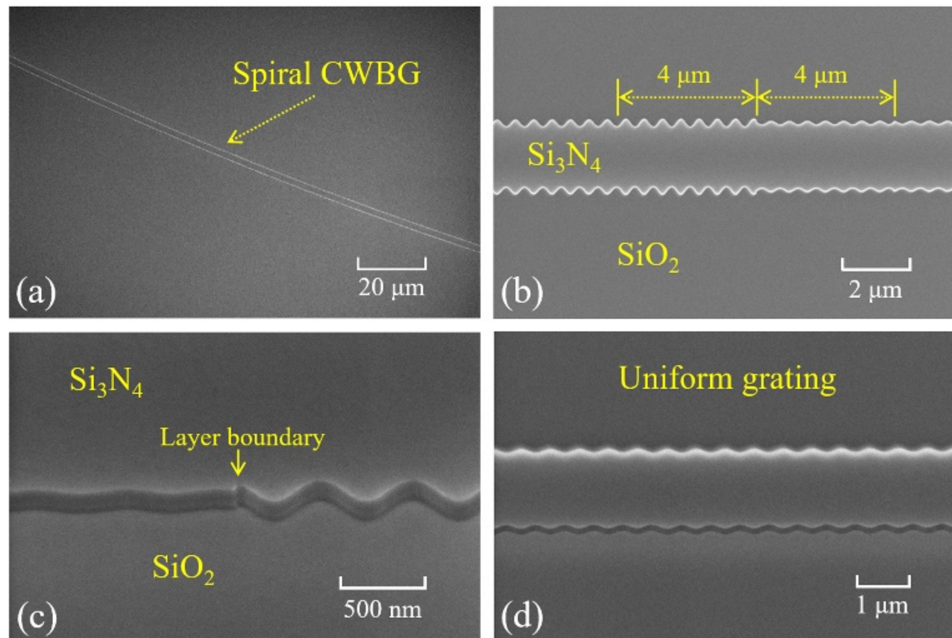

Figure 2.6 SEM of device patterned by ma-N recipe. SEM of two fabricated devices. (a) A segment of the spiral CWBG. (b) Zoomed-in view of (a). (c) Tilted and further zoomed-in view of (a). (d) Tilted view of another uniform grating used as an FPBG mirror.

With this optimized recipe, we can get much improved fabrication results, as shown in Figure 2.6. This is also the standard recipe we used for most fabrication work in this dissertation.

2.4.3 100 kV EBL with Resist ZEP520A

Another optimized recipe is to use ZEP520A, which is a high-performance positive e-beam resist which shows high resolution and high sensitivity. A lift-off process is still needed when going with ZEP520A. However, its advantage over PMMA is that the resist sidewall after development has an undercut profile, which is desired for lift-off processes [46]. In comparison, PMMA's sidewall usually has a foot profile, which tends to leave residuals during lift-off [46]. As a result, the post lift-off pattern will be much smoother with ZEP, as shown in Figure 2.7. The grating sidewall corrugation is well defined, which is important for low-loss applications.

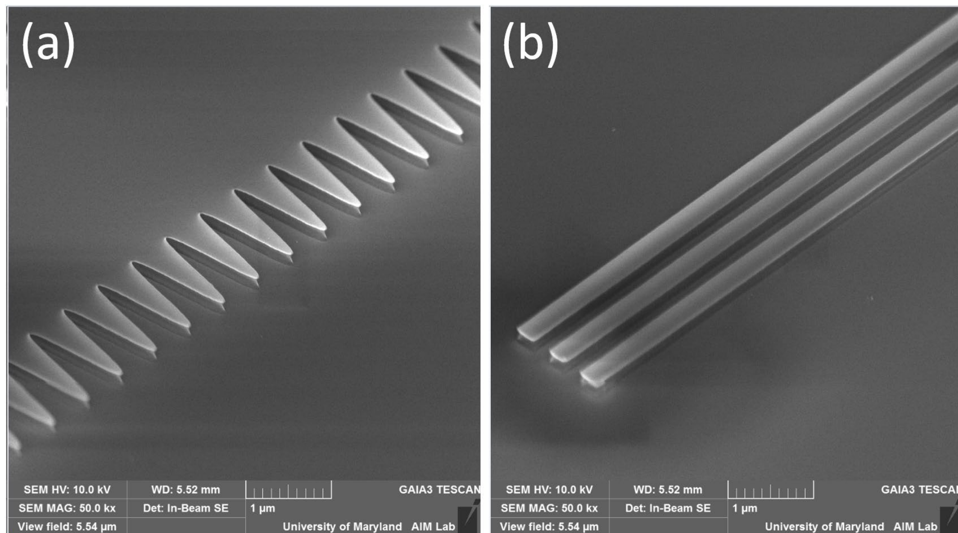

Figure 2.7 SEM of device patterned by ZEP recipe. (a) Tilted view of a grating with width variation 4um-7um (b) Tilted view of three 250 nm wide waveguides with 250 nm spacing. Etching depths are all 100 nm.

Below is the optimized ZEP recipe I used to fabricate the test samples above:

1) Spin coat ZEP520A on sample with 4500 rpm for 1min (resist thickness is around 300 nm)

2) Prebake with hotplate at 180 C for 5 min

3) Spin coat aquaSAVE with 4500 rpm for 30s

4) Expose with 100kV EBL system with 300 μC/cm^2 dose

5) Develop with ZED-N50 for 1 min, MIBK:IPA 1:3 for 30s and IPA for 30s

6) Ultrasonic liftoff for at least 1 min with remover PG

2.5 Ion-Coupled-Plasma (ICP) Reactive-Ion Etching (RIE)

When we go with the ma-N 2403 recipe, this organic resist is used as a soft mask for etching. The etching selectivity to SiN is about 1:1 to 1:5. With the recipe in Section 2.4.2, the coated resist is about 320 nm thick, which is capable of etching 300 - 400 nm SiN, depending on the etching recipes. Besides, a photoresist etching process for pre-etch descum is found beneficial for getting optimal pattern. The standard etching recipe I used is given below.

Etching:

1) Photoresist etch (Descum) with ICP etcher

   (Necessary step to get particle-free pattern. Etch down 50 nm photoresist with 15 s etching time. Parameters: RF power 30 W; ICP power 100 W; O2 40 sccm.)

2) 40s SiN etch 25W 500W SF_6 10 CHF_3 90 60nm

3) Twice ultrasonic cleaning with Remover PG, each 15 mins.

The gas SF_6 in step 2) can also be replaced with O_2. In fact, CHF_3/O_2 recipe is more popular for low loss waveguide etching, because O_2 can react with the resist residual to form carbon monoxide and carbon dioxide [7]. As for etching speed, CHF_3/O_2 and

CHF_3/SF_6 is almost the same in my experiments. To remove 100 nm thickness Si_3N_4, 55-60s etching time is needed. Step 3) is aiming to completely strip the organic soft mask away after etching. Since resists will become hardened after etching and more difficult for a residual-free removal, this is an essential and critical step the for ma-N recipe.

When going with positive resist recipes, step 1) will not be needed and step 3) is replaced with Cr removal with Chromium etchant 1020. Cr metal mask has a very high etching selectively to Si/SiN/SiO_2 and is more suitable for etching highly confined SiN waveguides or high aspect-ratio structures.

2.6 PECVD Cladding SiO_2

2.6.1 Advantages and Challenges of PECVD SiO_2 Film

For the SiN photonics platform, SiO_2 is the most popular cladding material. SiN/SiO_2 has a moderate index contrast such that the mode profile can be decently confined with little light scattering induced by surface roughness. Besides, the highly transparent SiO_2 film can also facilitate the device packaging. There are various SiO_2 deposition recipes available with CMOS compatible fabrication techniques. Currently, ultra-low-loss (< 1 dB/m, intrinsic $Q > 10^7$) structures have been realized with damascene thermal oxide [47], LPCVD low-temperature oxide (LTO) [7], LPCVD high-temperature oxide (HTO) [8], and LPCVD TEOS [17]. All of them have a relative low deposition rate and require a high temperature process varying from 700 – 1200 C. In most cases, the top cladding layer can only be deposited after the pattern is formed,

thus these processes are undesired or not usable for applications requiring low thermal budget or fast deposition rate.

Plasma enhanced chemical vapor deposition (PECVD) is an important SiO2 deposition process in semiconductor industry. PECVD is facilitated by plasmas of reactant gases rather than by high temperature [48]. It usually operates below 400 C, much lower than other CVD processes. However, it is only until recently when a UCSB group reported that TEOS is capable of delivering low loss results [9]. The reason is that there are still many challenges associated with high quality PECVD SiO_2 films, such as the film purity, uniformity, and density. At the Maryland NanoCenter, we have access to two recipes of PECVD SiO_2: PECVD Silane oxide and PECVD TEOS oxide. They can be run in an Oxford Plasmalab System 100 tool. Next, I will discuss my efforts to apply them into low-loss SiN photonics platform, respectively.

2.6.2 Silane Recipe

The nominal gas flow rates of silane-based oxide are 170 sccm of 5%SiH_4/95%N_2, 710 sccm of N_2O. Chamber pressure and 13.56 MHz RF power are set as 1000 mTorr and 20W. The deposition is performed with deposition rate 71 nm/min. The SiO_2 film such deposited is of high uniformity and stability. In fact, this type of film is preferred for many applications. For example, it is suitable to be deposited onto InP optoelectronic devices as a covering layer; it can be used as a durable mask material for subsequent dry etch processes; it can produce stable film properties even at 100 C deposition temperature. However, the critical disadvantage of this recipe is its high concentration of O-H and N-H bond inside the SiO_2 film. As a result, the film has large absorption near telecom bands and makes it undesired for ultra-low-loss applications.

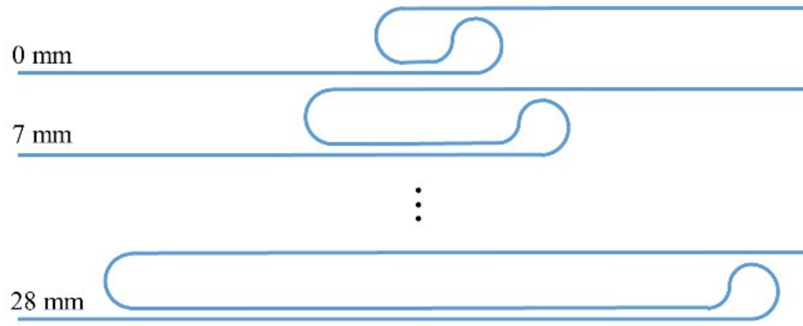

Figure 2.8 Illustration of the bending waveguide design for measuring linear propagation loss. We made five waveguides on the chip with length difference of 0, 7, 14, 21, and 28 mm. The corresponding loss results are shown in Fig. 2.9.

To quantify the effect of bond absorption, I fabricate uniform waveguides with PECVD Silane SiO_2 as the top cladding. The layout design is shown in Figure 2.8, different waveguides with length variations 0 mm, 7 mm, 14 mm, 21 mm, 28 mm are fabricated and measured. Two broadband sources centered at 1310 and 1550 nm are deployed to characterize the loss from 1200 to 1630 nm.

The unit distance loss can be extracted from the transmission with a linear fitting algorithm, as shown in Figure 2.9. The lowest loss occurs at the rightmost wavelength of the spectrum in Figure 2.9. Specifically, at 1630 nm, the TE loss is 0.16 ± 0.18 dB/cm, and the TM loss is 0.32 ± 0.13 dB/cm. However, when we move to a shorter wavelength like 1558 nm, TE loss is 0.68 ± 0.25 dB/cm, and TM loss is 0.79 ± 0.20 dB/cm.

There are two large absorption peaks near 1.4 µm and 1.5 µm which are brought by O-H and N-H bond absorption respectively [49]. The peak loss can reach up 5-5.5 dB/cm, which would significantly limit the photonic device performance.

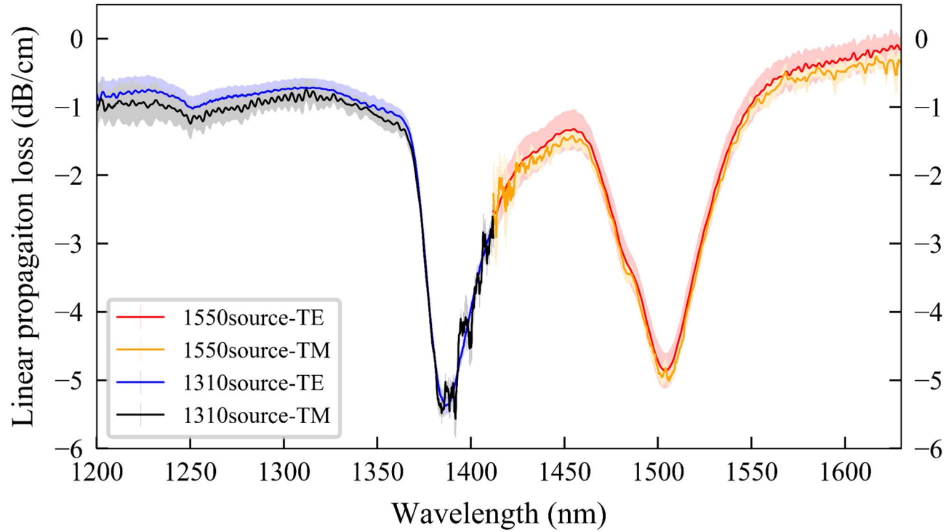

Figure 2.9 Linear propagation loss of Si_3N_4 /SiO_2 waveguide, extracted from the sample in Figure 2.8. The error bars are shown as the shaded area.

Another drawback for PECVD Silane recipe in low-loss applications is its relatively high refractive index (RI). I measured the film with Woollam spectroscopic ellipsometer. The RI near 1600 nm is 1.4632, much higher than the measured index of bottom thermal oxide cladding, which is only 1.4456. This difference will shift the optical mode center to the upper cladding, and allow the mode to see more the unpolished LPCVD SiN film's top surface roughness.

2.6.3 Standard TEOS Recipe

Tetraethoxysilane ($Si(OC_2H_5)_4$, commonly known as TEOS) has been used in plasma deposition systems since the 1970s [50]. It offers an alternative precursor to silane for PECVD SiO_2 processes in which low loss, conformal deposition of SiO_2 is required [48]. Unlike the highly flammable and toxic silane, TEOS is chemically stable, in liquid form and easier to handle. More importantly for our application, the TEOS oxide film doesn't have any N-H content, which inherently avoids the absorption peak near 1.5 μm.

Oxford Plasmalab System 100 has an integrated TEOS SiO_2 deposition solution. Either low frequency (LF) or high frequency (HF) RF field can be used to generate the plasma. The standard LF process recipe is as follows: 50 sccm of TEOS (Ar bubbler); 500 sccm of O_2; chamber pressure 500 mTorr; RF power 50 kHz, 40W. The deposition rate is 40-50 nm/min. With this recipe, up to 2 μm TEOS film can be deposited. Thicker films are not achievable because of cracking issues. However, the thickness uniformity and deposition rate stability of the deposited film are not as good as PECVD Silane film.

Another issue of LF TEOS oxide is its time varying film properties, which could significantly impair the device performance. Figure 2.10 shows two transmissions of a π-phase-shifted Bragg grating cavity measured at different times after the PECVD TEOS process. It is clear to see that the stopband center and cavity resonances both suffer a dramatic change. The cavity transmission is relatively regular when the deposited film is “fresh” to the outer environment. However, the transmission becomes disturbed when the device is exposed in air for a longer time. Generally, this time-dependent behavior could last 2-3 days until it becomes stable. The device we measured here is a π-phase-shifted Bragg grating (PSBG), which can be regarded as a Fabry-Perot cavity formed by two Bragg grating mirrors. Details about the Bragg grating cavity can be found in Chapter 3.

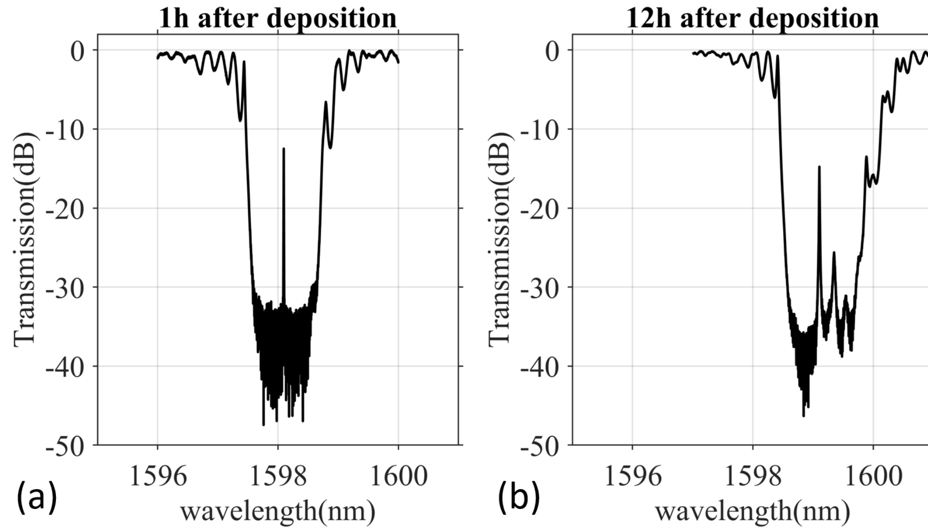

Figure 2.10 Transmission of a phase-shifted Bragg grating fabricated with 2 μm PECVD TEOS top cladding. They are measured 1 hour (a) and 12 hours (b) after the deposition process is finished.

The time-dependent behavior of TEOS film is also confirmed by the film stress measurement. I used the Flexus 2320 System to measure the LF TEOS film stress. This system determines the stress by optically measuring the change in the radius of curvature of a standard 4-inch wafer. The first measurement is done immediately after the deposition, and following measurements continue for several days until the stress value becomes stable. The results show that the stress of LF TEOS film is always compressive and changes from -50 MPa to about -200 MPa. The HF TEOS recipe use the standard PECVD RF frequency 13.56 MHz, and the corresponding film exhibits a much different property. Its stress is tensile, above 150 MPa at the beginning and changes to a compressive stress -50 MPa after several days. I also measured the PECVD silane film for comparison, which, on the other hand, has a very stable stress about -150 MPa.

The film index is also measured with a Woollam spectroscopic ellipsometer. The RI near 1600 nm is 1.4388, slightly lower than the cladding index of the bottom thermal

oxide 1.4456. This implies that the waveguide mode tends to be dragged down a little to the high-quality thermal oxide cladding, which is preferred for low-loss applications.

2.6.4 Optimized TEOS Recipe with Silane Oxide Cover

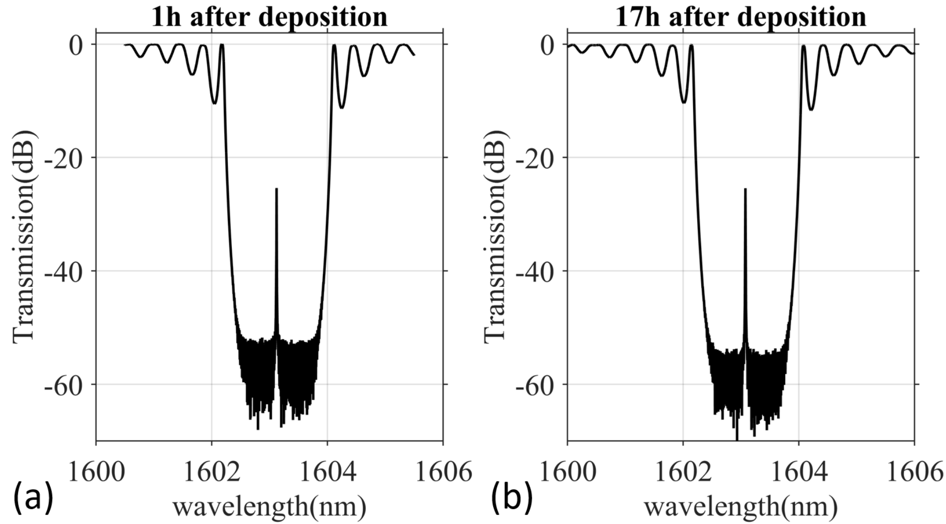

Figure 2.11 Transmission of a PSBG device fabricated with 5 μm TEOS oxide top cladding covered by 1 mm silane oxide. Measured 1 hour (a) and 17 hours (b) after the deposition.

Based on the information we have gathered, it can be deducted that the cracking of LF TEOS films could be caused by exposure to the atmospheric environment, rather than the intrinsic film stress itself. As a result, if we deposit a thin layer of silane oxide on top of LF TEOS oxide, we might be able to get a much thicker crack-free film. The experimental results validate this idea, as shown in Figure 2.11. The two transmissions measured at different times are very regular and similar. It implies a high-quality deposited film with stable properties not relying on the elapsed time. In experiment, a 500 nm (or less) thick silane oxide cover is found to be good enough for protecting 5 μm TEOS oxide film. However, a thicker (up to 6 μm) silane oxide cover is sometimes used when thicker top cladding is preferred.

Below are the detailed steps of this optimized recipe:

1) Pre-heat: process chamber 360 C; TEOS showerhead 75-80 C; TEOS oven 60 C; TEOS delivery line 80 C

2) 1-min N_2 Purge

3) 5-min TEOS recipe gases flow (no RF)

4) 1.5-hour TEOS oxide deposition (LF RF power = 40 W)

5) 3-min pump

6) 3-min N_2 purge

7) 3-min pump

8) 1-min silane recipe gases flow (no RF)

9) 15-min silane oxide deposition (HF RF power = 20 W)

Although this recipe works well, we still want to understand better why the significant improvement occurs. It turns out that similar phenomenon has been observed by many previous studies [51]–[54]. The generally accepted explanation is that the porous CVD oxide film can absorb water vapor in the ambient and film stress will become more compressive because of the absorbed water.

2.6.5 Further Discussions on PECVD TEOS

PECVD is a very flexible deposition method and there are a variety of system parameters to adjust for achieving different fabrication goals. In fact, these parameters are of great importance to the process outcome. Several studies demonstrated the stress control of silicon oxide using dual-frequency approach in PECVD TEOS [55], [56]. As is mentioned in 2.6.3, the LF and HF TEOS recipes have compressive and tensile stresses (when not affected by the atmospheric environment), respectively. By running two recipes alternatively, zero stress films could potentially be achieved [56]. One can

control the average oxide film stress by changing the fraction of the HF plasma and LF plasma. Similar results are also given in the Oxford Instruments training manual for PECVD TEOS.

In my experiment, this approach is not adopted because the measured LF TEOS film is already rather low -50 MPa. LF recipe itself is enough to hold up to 5-6 μm TEOS film when silane oxide cover exists. On the other hand, HF TEOS films have a much higher 150 MPa tensile stress. Besides, it is known that the HF plasma deposits more porous films than the LF plasma. Without the silane oxide cover, the critical thickness for crack-free HF TEOS films is about 1 μm, while the value is 2 μm for LF TEOS films. These factors increase the difficulty of finding a balanced recipe for achieving zeros stress films. However, for ultra-thick deposition above 10 μm, we expect this dual frequency approach to be much more beneficial.

2.7 Thermal Annealing

There is no nitrogen content involved in the deposition process of thermal oxide and PECVD TEOS oxide, so the N-H absorption peak near 1.5 μm will not exist. However, as discussed in 2.3, the LPCVD SiN process can also introduce N-H bond. For a complete removal of N-H bond, high temperature thermal annealing is still needed.

We first test the annealing results for waveguides cladded with PECVD silane oxide. The sample measured in Figure 2.9 is annealed 2 hours at 1150 C. The after annealing loss curve is shown here in Figure 2.12. The absorption peak near 1.5 μm indeed drops from 5 dB/cm to 1.5 dB/cm. It can also be seen that the measurement

error increased after annealing. A possible reason is that the annealing process introduced larger coupling efficiency fluctuation among different waveguides.

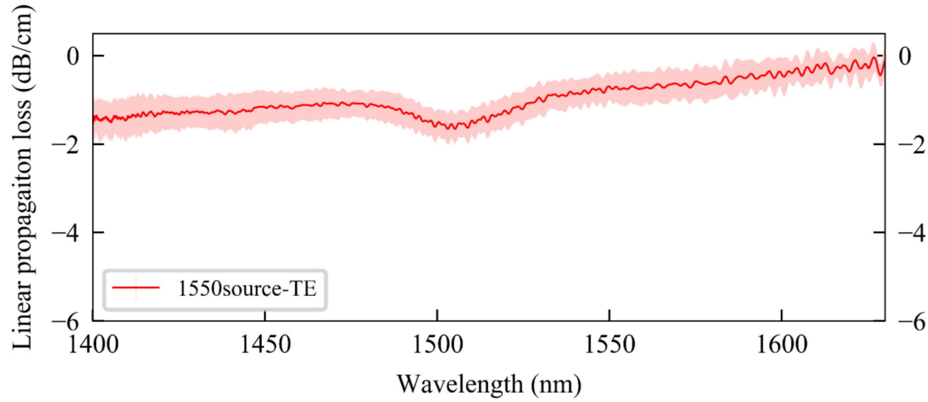

Figure 2.12 Waveguide propagation loss for TE mode after annealing. The measurement is done with the same sample in Figure 2.9, but after 2-hour annealing at 1150C. The error bars are shown as the shaded area.

Longer annealing time is expected to further improve the loss result in Figure 2.12. However, the SiN and SiO_2 films will undergo a reflow process at such high temperature. On the one hand, this is acceptable or preferable for linear waveguides and ring cavities because a moderate reflow could improve the boundary smoothness. On the other hand, the reflow process could introduce non-uniformity for patterned structures, which is extremely undesirable for long or complicated waveguide gratings. Any non-uniformity during the annealing process, which is almost inevitable, could alter the grating strength/period and impair the grating performance. As seen in Figure 2.13, there is a significant change of the Bragg grating sidewall corrugation before and after the annealing.

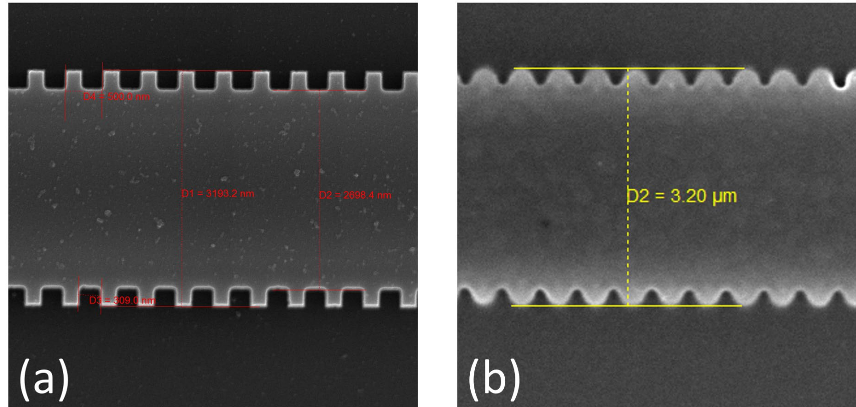

Figure 2.13 SEM of a 2.7 – 3.2 μm Bragg grating before (a) and after (b) 1-hour 1150 C annealing. Images courtesy of Shengjie Xie.

A solution to this issue is that we perform the thermal annealing before the EBL patterning. In this case, the top cladding could not be annealed such that the O-H bond absorption of PECVD TEOS film near 1.4 μm will still exist. However, for spectral range above 1.45 μm, the loss curve is satisfying, as seen in the black curve of Figure 2.14. It is extracted from a 6-cm-long spiral waveguide and a 1-cm-long reference straight waveguide with PECVD TEOS top cladding. The spiral waveguide's minimum bending radius is 500 μm, which brings some bending loss at longer wavelengths. Overall, three dominant losses are illustrated, which are the O-H bonding loss in the PECVD TEOS SiO_2; the N-H bonding loss in the LPCVD Si_3N_4 and the spiral bending loss. We can see that PECVD TEOS oxide film can indeed significantly reduce the absorption loss near 1.5 μm. The peak loss value is only about 0.5 dB/cm, much lower than the 5 dB/cm value in Figure 2.9. Better result is obtained after if the device is annealed 1-hour at 1150 C before EBL, which is shown as the red curve. The N-H absorption peak is not observable anymore. And the lowest loss is about 0.10 dB/cm for wavelengths above 1560 nm. Besides, the bending loss also disappears due to the increased spiral innermost radius (from 500 μm to 750 μm).

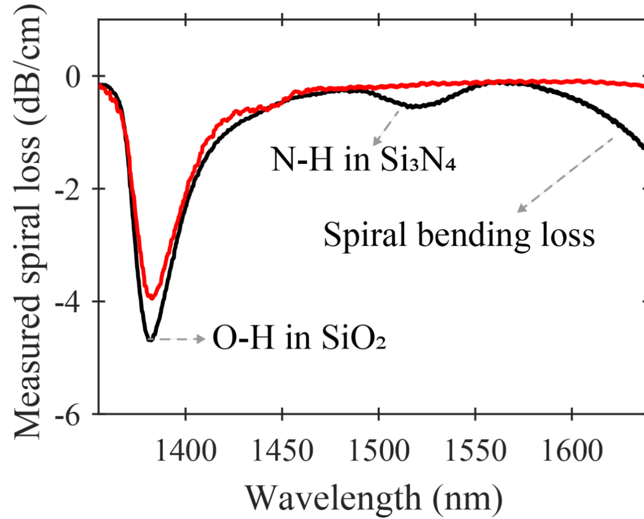

Figure 2.14 Measured spiral losses for two spiral waveguides with 500 μm inner radius (black) and 750 μm inner radius (red). The 750 μm inner radius sample is annealed in 1150C. implies N-H content is very low in TEOS films.

2.8 Summary

In this chapter, I have studied optimization methods from device design to the fabrication to reduce the loss on the SiN photonics platform. The main focus is to eliminate the N-H absorption peaks near 1.5 μm introduced in oxide and SiN film deposition. Combining all these efforts discussed, the linear waveguide loss range drops from 0.16 – 5 dB/cm to 0.10 dB/cm – 0.20 dB/cm between the wavelength range 1450 and 1640 nm.

There are still more improvements which can be done in the future. Currently we did not use chemical-mechanical planarization (CMP) to polish the material interfaces (SiN/SiO_2 and SiO_2/air), which is typically necessary for achieving loss values below 0.10 dB/cm. Moreover, if thicker (> 500 nm) crack-free LPCVD SiN film can be realized, the optical mode will be strongly confined to see less sidewall roughness and

have smaller loss. Recent studies show that defining crack-stopping trenches [7], [11], [57] or twist-and-grow deposition [10] could be viable approaches.

Chapter 3: Integrated Waveguide Characterization with Grating Cavities

In this chapter, a new approach is developed for measuring small losses in ultra-low-loss SiN waveguides. It is based on measuring the transmission of an on-chip Fabry-Perot cavity formed by two Bragg gratings and a passive waveguide in between. Different from other loss measurement methods based on FP cavity [58]–[60], we use highly reflective (R > 0.998) integrated gratings as the cavity mirror and a highly precise numerical fitting procedure, which brings us much higher loss measurement accuracy (around 0.01 dB/cm in experiment). This approach is particularly applicable to waveguides written by EBL whose lengths cannot be easily extended beyond several centimeters. Besides, since the cavity is formed on a straight structure and does not have any bending loss, this approach can operate equally well for optical modes with any confinement factor.

3.1 Bragg Grating Modeling and Design

On-chip gratings are important for various photonic applications, such as sensing, filters and lasers. Among different types of gratings, Bragg gratings is one of the most promising candidates to be generally employed in photonic integrated circuits (PICs), mostly for its simplicity and compatibility with uniform waveguides. On the other hand, when it comes to the ultra-low loss regime, their extra scattering loss poses a challenge for researchers to make them competitive with their ring resonator counterparts.

We aim at using Bragg gratings to implement high reflectivity, low loss cavities: phase-shifted Bragg gratings (PSBG) and Bragg grating Fabry-Perot cavities (BGFP). Furthermore, we demonstrate how to use them as a characterization tool for low loss waveguides. In this section, we will first focus on their modeling and design.

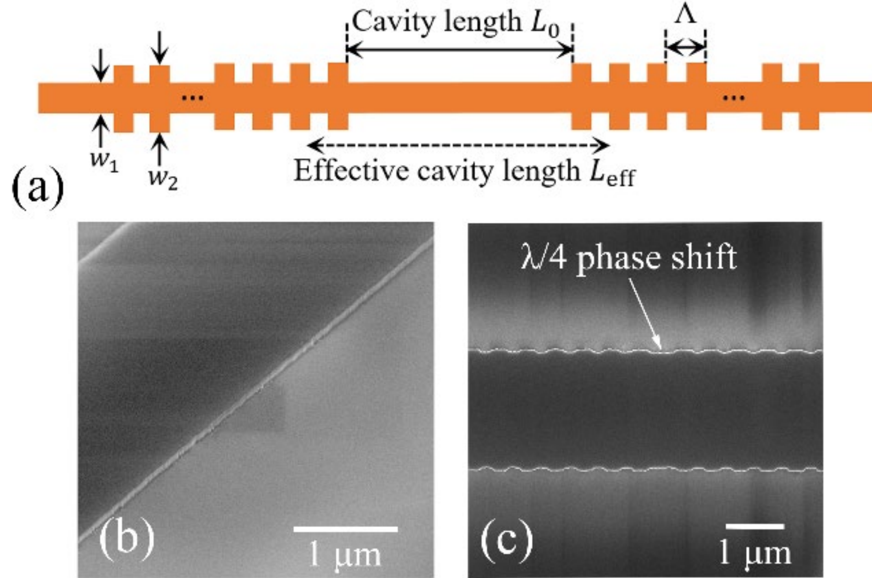

Figure 3.1 (a) Illustration of the Bragg grating design. For PSBG, cavity length L_0=Λ ~ 550 nm. For BGFP, we made the cavity length L_0 = 1 mm, 3 mm and 6 mm. (b) Tilted view of the 2 μm ×100 nm straight waveguide. (c) Top view of the λ/4 PSBG; the π phase shifted part can be recognized in the figure center.

Our theoretical model is based on the ABCD matrix method which is convenient to use for studying the transmission of optical waves in periodic structures. We will briefly discuss it, and a detailed theory can be found in [61]. What we consider here are two Bragg gratings with a physical cavity length L_0 in the center, as illustrated in Figure 3.1(a). In the design, the grating on each side consists of N pairs of alternating width (w_1 and w_2) waveguide segment with period $\Lambda = \lambda_c/2n_{eff}$. λ_c is the stopband center wavelength. Starting from basic electromagnetic equations, we can derive a matrix equation relating the field amplitude at two neighboring grating periods,

$$\begin{bmatrix} a_{n-1} \\ b_{n-1} \end{bmatrix} = \begin{bmatrix} A & B \\ C & D \end{bmatrix} \times \begin{bmatrix} a_n \\ b_n \end{bmatrix} \tag{3.1}$$

Here a_n and b_n are the electric field amplitude in the nth grating period for a right-traveling and a left-traveling plane wave. A, B, C, D are transfer coefficients determined by the electrical boundary conditions. For the uniform cavity part, $A = e^{ik_{1z}L_0/2}$, $B = C = 0, D = e^{-ik_{1z}L_0/2}$. Here k_{1z} is the propagation constant in width w_1 waveguide segment.

The coupling coefficient κ is an important concept in coupled mode theory, which is quite useful for grating design. For a 1-d grating discussed here, if we denote the larger index as n_1 and smaller index as n_2, κ can be roughly estimated as $\kappa = \pi/\lambda\ (n_1\text{-}n_2)$, and the stopband width is

$$\Delta\lambda \sim \frac{\lambda^2 |\kappa|}{\pi n_{eff}} \tag{3.2}$$

For the transmission calculation, we still need to know the effective indices for waveguide width w_1 and w_2 throughout the studied spectral range, which are obtained using the FIMMWAVE full-vectorial mode solver. Note that in the final fitting of the transmission curve, we still need to slightly adjust the index profile to account for the rounded edges of the grating structure (Figure 3.1(c)).

3.1.1 π-Phase-Shifted Bragg Grating

First, we design a π-PSBG (L_0=Λ) to get a narrow peak at the stopband center. The peak's linewidth and intensity are very sensitive to propagation loss, so we can use it to measure the grating loss α_g. To get high enough measurement resolution for state-of-the-art low loss waveguides, we want to design a PSBG with as narrow linewidth as possible, which requires a large κL_g for high reflection, where $L_g = N\Lambda$ is the grating

length. After careful theoretical and empirical studies, we choose w_1=2 μm, w_2=2.15 μm, corresponding to a moderate $\kappa \sim 10$ cm^{-1}, which is a compromise for low scattering loss and decent grating coupling efficiency. As $R \sim \tanh^2(\kappa L_g)$, in the layout design, we choose L_g to be around 3.5 mm to make κL_g large enough to get single side mirror reflection $R > 0.995$.

3.1.2 Bragg Grating Fabry-Perot Cavity

The Q of PSBG is dominated by the grating loss α_g. In order to measure uniform waveguide loss, we keep the same reflecting gratings and make L_0 much larger to form a Fabry-Perot cavity. Since the cavity loss is always smaller than the grating loss, photons will stay inside for longer time before leaking out. As a result, BGFP can have higher Q ($Q \sim \omega\tau$, τ is the photon lifetime) than PSBG. This is confirmed experimentally in the next section.

3.1.3 Loss Terms in the Model

Transmission matrix terms, A, B, C, D depends on 3 variables, k_{1z}, k_{2z} (propagation constant in width w_2 waveguide segment), and the grating period Λ. To take the loss terms into consideration, we only need to add an imaginary part to k_{1z} and k_{2z}. For example,

$$k_{1z} = n_1 \times \frac{2\pi}{\lambda} - i n_{\text{img}} \times \frac{2\pi}{\lambda} \tag{3.3}$$

Note that $\alpha = 4\pi n_{\text{img}}/\lambda$, and we have two loss terms, the grating loss α_g and the cavity loss α_c (for PSBG, $\alpha_c = \alpha_g$). By fitting our experimental and theoretical curve with different lengths cavities, we can extract both α_g and α_c.

3.2 Experimental Results

To characterize the transmission spectrum, we use a setup composed of a Keysight 81600B tunable laser and a Keysight N7744A power meter. The tunable laser triggers the power meter during the wavelength scanning for fast spectral measurement with 0.1 pm resolution. Polarization maintaining fibers are used for optical mode launch and collection. Fiber rotators are also employed for the TE/TM control. The fiber input and output coupling are accomplished by two Newport VP-25XL XYZR motorized stages with 10 nm minimum incremental motion.

3.2.1 π-Phase-Shifted Bragg Grating

In Section 2.6.2, we demonstrate the loss characterization method using length variation. However, the standard error is as high as 0.1 – 0.2 dB/cm. This is a main disadvantage of the length variation method, whose measurement error depends not only on the waveguide fabrication stability, but also on the coupling efficiency stability. It is undesirable for current low loss waveguide. Now we used two PSBG to demonstrate the loss fitting at two different wavelengths, 1558 and 1629 nm, and compare with the loss obtained in Section 2.6.2.

The fitting process is as follows: first, we scale and shift the index profile to fit the stopband position and width; next we adjust the grating loss α_g to find the best fitting curve, as shown in Figure 3.2. The fitting parameters are also shown in the caption. An important criterion is that we must use the same wavelength dependent effective index profile for the fitting curves. The 1558 nm PSBG has a larger index contrast than the

1629 nm PSBG because the shorter wavelength mode is more confined and more sensitive with width variation.

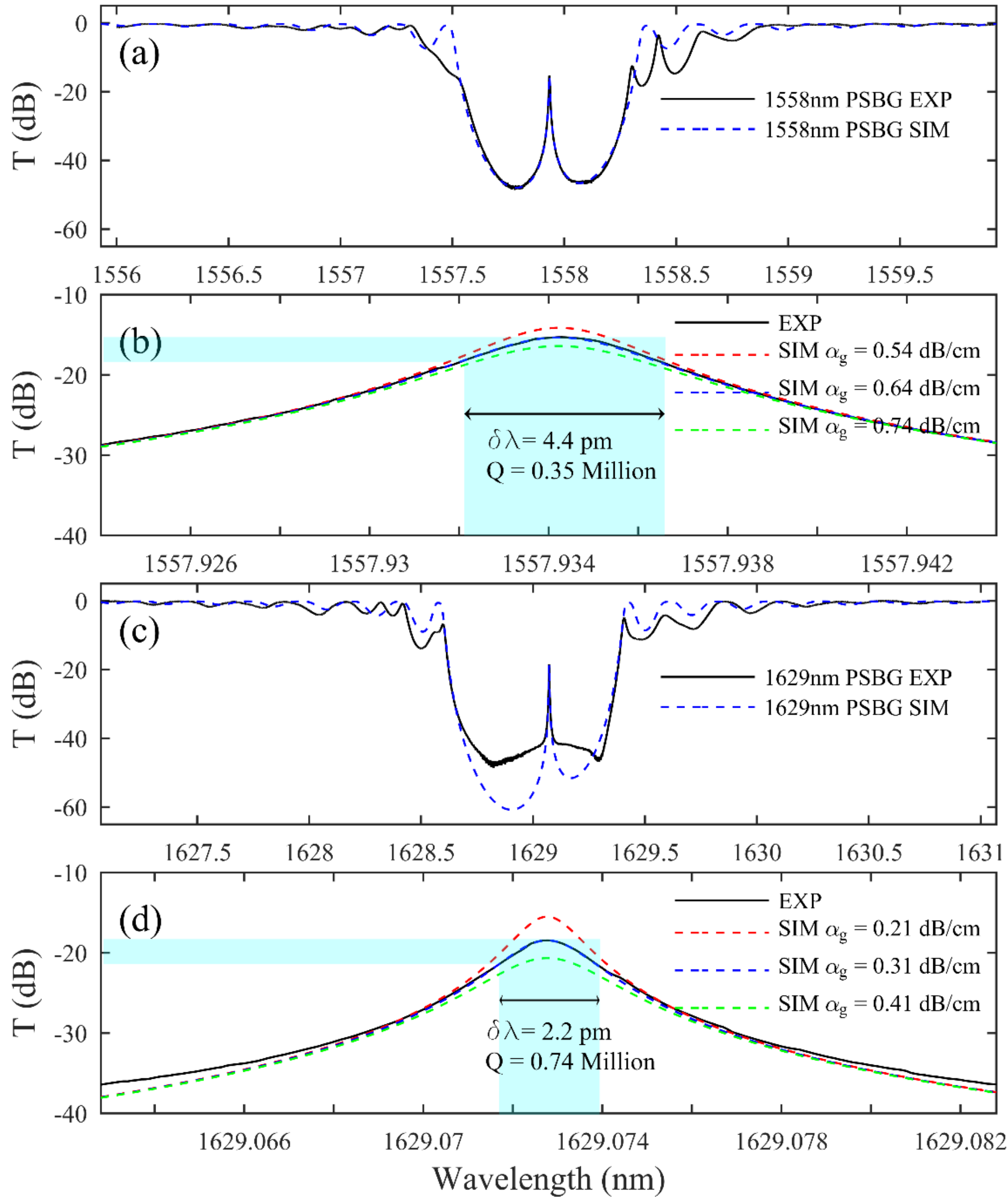

Figure 3.2 PSBG grating experimental (black solid line) and theoretical fitting (dashed lines) results. In (a)(c), the wavelength range is 4 nm. In (b)(d), the wavelength range is 20 pm. Fitting parameters: (1558 nm) $n_1 = 1.47584$, $n_2 = 1.47691$; $\Delta n = 0.00107$, $\kappa = 10.81$ cm^{-1}, stopband width $\Delta\lambda = 0.563$ nm. (1629 nm) $n_1 = 1.47171$, $n_2 = 1.47273$; $\Delta n = 0.00102$, $\kappa = 9.85$ cm^{-1}, $\Delta\lambda = 0.561$ nm.

From the theoretical fit, we get the grating loss $\alpha_g = 0.64$ dB/cm at 1558 nm and $\alpha_g = 0.31$ dB/cm at 1629 nm. Although we only plotted another two fitting curves with

± 0.1 dB/cm in Figure 3.2, the fitting accuracy can actually reach about ± 0.01 dB/cm with 0.1 pm wavelength resolution, as shown in Table 3-1.

For the 1629 nm PSBG, the narrowest linewidth we can get is 2.2 pm, corresponding to a $Q \sim 7.4 \times 10^5$. The extinction ratio (ER) of the 1558 nm grating is 50 dB, and that of the 1629 nm grating is 60 dB (limited to 50 dB in measurement by the uncoupled fiber input light).

L_0	Loss [dB/cm]	Center Peak intensity [a]	Linewidth [b]	Q
553 nm (=Λ)	0.29	-17.95 dB	2.06 pm	7.90×10^5
	0.31	-18.47 dB	2.19 pm	7.45×10^5
	0.33	-18.96 dB	2.31 pm	7.05×10^5

Table 3-1 PSBG (centered at 1629 nm) fine fitting results for Figure 3.2.
[a] The center peak intensity is the maximum transmission the center peak can reach. The center peak intensity will be exactly 0 dB if both the grating loss α_g and cavity loss α_c are 0.
[b] The linewidth measured in experiment is 2.2 pm.

3.2.2 Bragg Grating Fabry-Perot Cavity

We can extract the grating loss from the PSBG sample. However, we still cannot tell the exact straight waveguide loss. We fabricated three additional Bragg gratings with center length 1 mm, 3 mm and 6 mm. Thus, the transmission contains the information from both α_g and α_c. The fitting process is similar to that of the PSBG, and the results are shown in Figure 3.3.

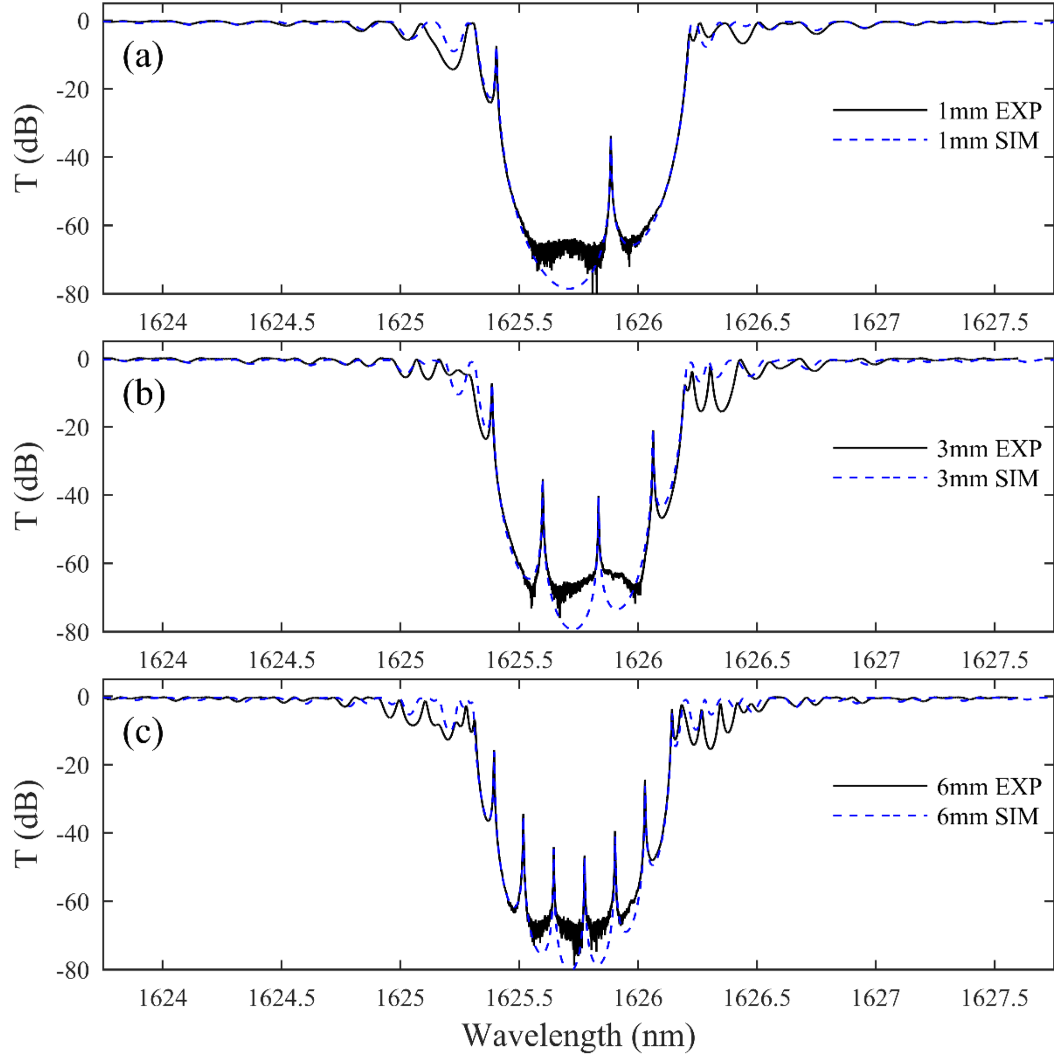

Figure 3.3 Experimental and simulation curves for Bragg grating cavity with length (a) 1 mm, (b) 3 mm and (c) 6mm. For the blue simulation curve, we use grating loss 0.41 dB/cm and cavity (straight waveguide) loss 0.24 dB/cm. The wavelength range is 4 nm in all four panels. The y axes are set to be the same. Fitting parameters: $n_1 = 1.47860$, $n_2 = 1.47979$; $\Delta n = 0.00119$, $\kappa = 11.5\ \mathrm{cm}^{-1}$, $\Delta\lambda = 0.649$ nm.

In this BGFP sample we kept the grating design parameters the same as for the PSBG sample. However, ER can reach -70 dB in experiment and -80 dB by fitting. A one-side mirror reflectivity $R \sim 0.998$ is achieved. There are two reasons that we get higher ER than in Figure 3.2. First, we increase the offset between the input and the output waveguides to reduce the background light intensity; secondly, we have higher

index contrast Δn due to a slightly thicker LPCVD Si_3N_4 layer, which can be confirmed in the Δn fitting parameters (0.00119 vs 0.00102).

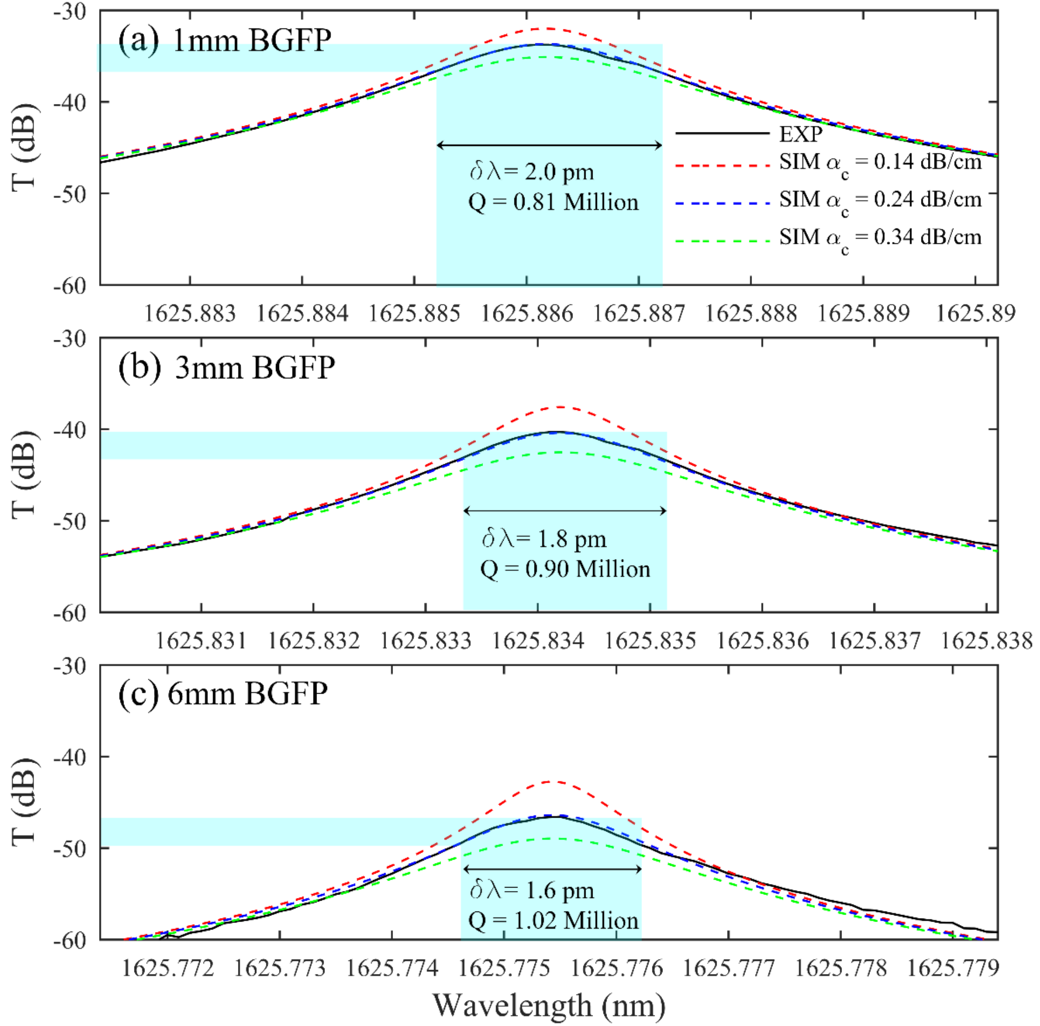

Figure 3.4 The enlarged figure for BGFP transmissions. Red, blue and green lines denotes cavity loss α_c = 0.14 dB/cm, 0.24 dB/cm and 0.34 dB/cm. Grating loss α_g is set as 0.4 dB/cm. (a) 1 mm cavity with linewidth 2.0 pm. (b) 3 mm cavity with linewidth 1.8 pm. (c) 6 mm cavity with linewidth 1.6 pm. Note that the legend in (a) also holds for (b) and (c). The x range are all 8 pm, y axes are set to be the same.

In the enlarged plots of Figure 3.4, it can be seen clearly that the longer cavity leads to a narrower linewidth, consistent with our expectations. The best Q we get is $1.02\times10^6 \sim \delta\lambda = 1.6$ pm. To our knowledge, this is the best Q obtained with on-chip Bragg gratings. From Table 3-2, we can see that decent loss resolution can be achieved.

L_0	Loss [dB/cm]	Center Peak intensity [a]	Linewidth [b]	Q
6 mm	0.22	-45.78 dB	1.51 pm	7.90×10^5
	0.24	-46.40 dB	1.62 pm	7.45×10^5
	0.26	-46.98 dB	1.73 pm	7.05×10^5

Table 3-2 BGFP (centered at 1625.8 nm) fine fitting results for Figure 3.4.
[a] Modeling uses α_g = 0.41 dB/cm. [b] The experimental linewidth is 1.6 pm.

We also studied the effective cavity length L_{eff} (illustrated in Figure 3.4) of BGFP. From Figure 3.3, we measured the FSR for each cavity. They are 0.481 nm, 0.234 nm and 0.129 nm, which corresponds to L_{eff} = 1.86 mm, 3.82 mm and 6.93 mm, respectively. The difference between L_{eff} and L_0 is quite stable, about 0.8-0.9 mm, which is favorable to design specific FSR cavities.

3.2.3 Record Loss Reduction with Optimized Fabrication

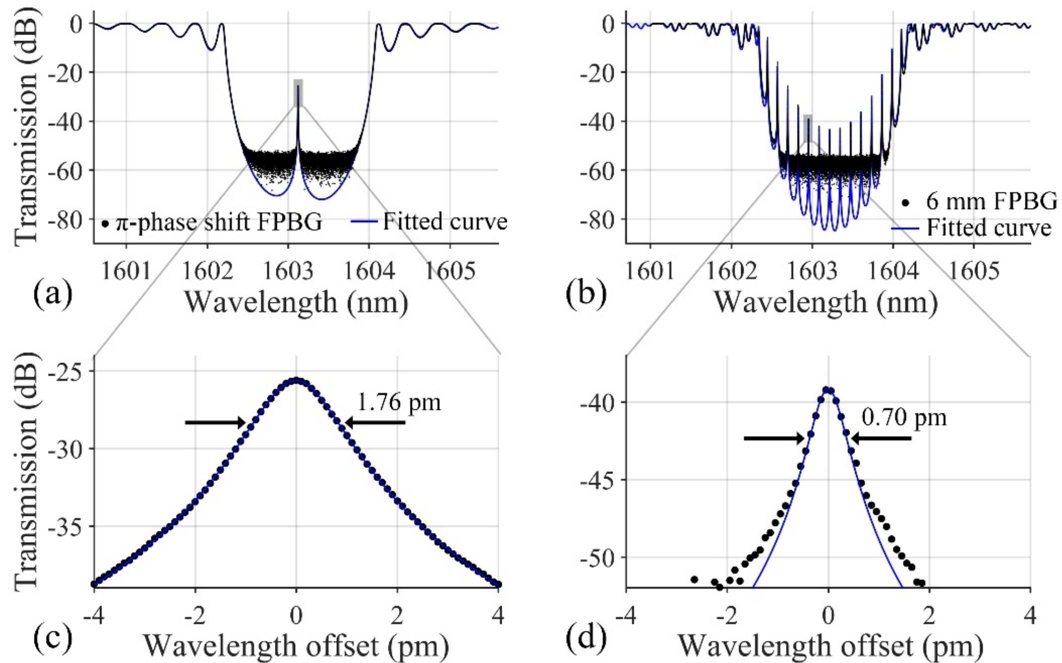

Figure 3.5 Waveguide and grating loss characterization from device with optimized fabrication. The grating loss is extracted as 0.26 dB from (a) π-phase shift FPBG. The waveguide loss is extracted as 0.10 dB from (b) 6mm FPBG. (c),(d) are zoomed-in views of (a),(b).

The discussions above are all based on devices fabricated with the PMMA EBL and PECVD silane oxide cladding. To validate the optimized fabrication process with 100 kV EBL (ma-N recipe, see Section 2.4.2) and PECVD TEOS oxide cladding (Section 2.6.3), we characterize devices such fabricated, with results shown in Figure 3.5. Here the cavity mirrors are 2-2.4 μm uniform Bragg gratings with 3000 periods on each side. A part of the grating mirror is shown in Figure 3.5(d). The fitted single mirror reflection is about 0.999. The loaded quality factor is 0.94 million for the π-phase shift FPBG and 2.3 million for the 6 mm FPBG. By fitting the experimental curve to our grating model, we determine that the grating mirror loss is 0.26 dB/cm and the uniform waveguide loss is 0.10 dB/cm. These are the record *Q* and loss values which our group have ever achieved with grating cavities.

3.3 Further Discussions

3.3.1 Lower Limit of Measurable Waveguide Loss

The waveguide samples discussed in this work don't have ultra-low losses. However, if we use a less confined waveguide mode and combine with some state-of-the-art EBL waveguide fabrication techniques [11], it is possible that losses down to 0.001 dB/cm can be achieved. So it is quite important to assess the lower limit of measurable waveguide loss.

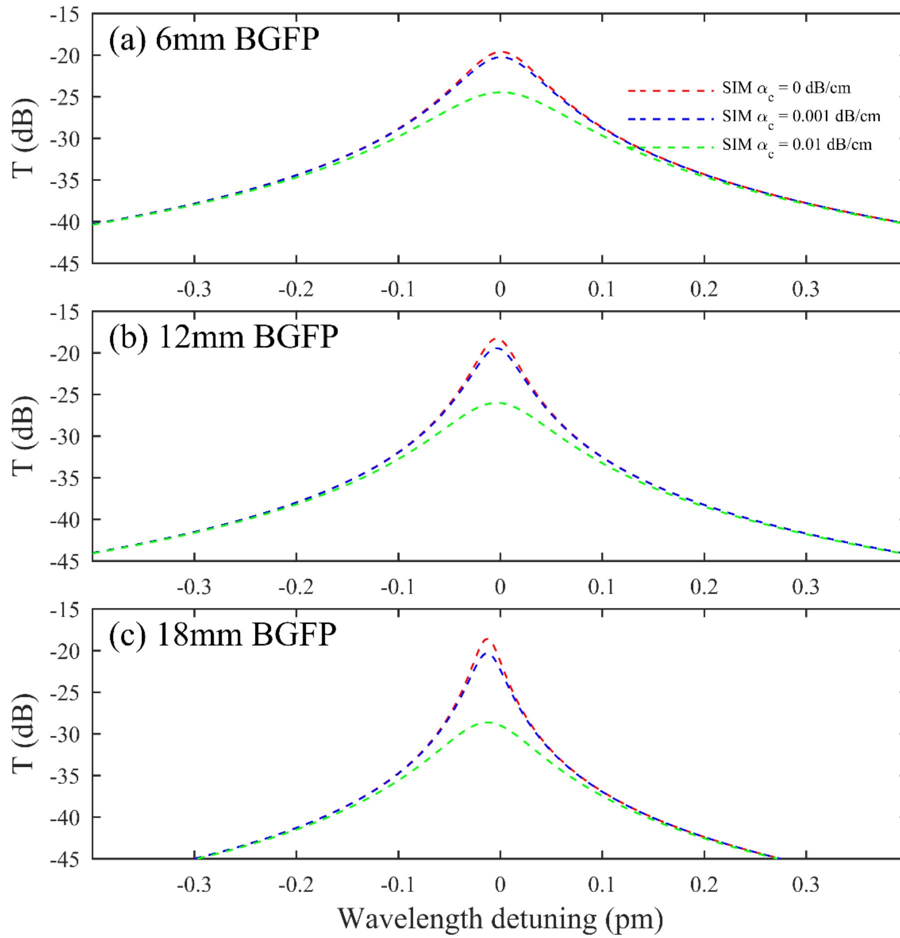

Figure 3.6 BGFP simulation to demonstrate its potential for measuring very low loss coefficients. We keep the grating loss α_g = 0.1 dB/cm, and set the cavity loss α_c = 0, 0.001 and 0.01 dB/cm.

Since our α_g can be 0.31 dB/cm, only 0.07 dB/cm higher than the straight waveguide loss, it is reasonable to assume that our current Bragg grating design introduces an extra scattering loss < 0.1 dB/cm. Now we can simulate whether our approach is applicable for the current best waveguide loss level ~ 0.001 dB/cm.

L_0	Loss [dB/cm][a]	Center Peak intensity	Linewidth	Q
12 mm	0	-18. 29 dB	0.041	3.97×10^6
	0.001	-19.45 dB	0.047	3.46×10^6
	0.01	-26.01 dB	0.100	1.63×10^6

Table 3-3 12 mm BGFP Modeling Results Related with Figure 3.6
[a] Modeling uses grating loss 0.1 dB/cm.

In Figure 3.6, we keep α_g = 0.1 dB/cm, and set α_c as 0, 0.001 and 0.01 dB/cm. If we look at the green curve, which stands for 0.01 dB/cm loss level, it is obvious that our approach can easily handle it even with cavity length 6 mm. For 0.001 dB/cm loss, however, we may have to use longer cavities to increase the sensitivity. In Table 3-3, we exhibited some numerical values extracted from Figure 3.6. For a 12 mm BGFP with α_c = 0.001 dB/cm, although the linewidth only changes by 0.006 pm compared with α_c = 0 dB/cm, the center peak intensity can drop more than 1 dB, which can easily be measured in the experiment without much difficulty.

3.3.2 Lower *κ* Grating

Another direction to optimize our approach is to use a lower κ grating for getting lower α_g. Now our grating κ is about 10 cm^{-1}. If we decrease it and increase L_g to keep κL_g a constant, we will also see an improvement in the loss measurement limit.

The underlying physics is that for the center cavity, its peak linewidth $\delta\lambda$ depends only on the loss terms α_g, α_c, L_{eff} and grating reflection κL_g. As long as κ drops and we extend L_g to keep the mirror reflectivity the same, the cavity Q will be increased. In experiment, a 1/10 factor decrease (κ = 1 cm^{-1}) is definitely achievable. Further reducing the grating κ might be limited by fabrication stability and accuracy.

3.3.3 Loss Measurement Bandwidth

Since we use a simple Bragg grating as a reflective mirror, there is only one stopband in the wavelength range of interest and the bandwidth is also quite narrow. To measure losses at different position, we have to use multiple waveguides or multiple cavities in a line. However, combined with the complex grating technologies we

developed for on-chip waveguides or fibers, the proposed approach is actually quite viable to be used for loss measurement with over 100 nm wavelength range. This is very attractive for ultra-fast, ultra-broadband loss characterization.

3.4 Summary

We have proposed an alternative method for measuring ultra-low loss coefficients in a waveguide, which is both accurate and efficient. The approach is particularly applicable to waveguides written by high resolution patterning techniques like e-beam lithography (EBL), whose lengths cannot be easily increased beyond several centimeters. This method is based on measuring the transmission of an optical cavity formed by two highly reflective (R > 0.998) simple Bragg gratings and a uniform waveguide between the two gratings whose length can be varied to increase the loss fitting accuracy. A theoretical model based on an ABCD matrix method is developed and used for the final loss value fitting. Experimentally, a cavity with extinction ratio over -70dB, and quality factor $Q = 1.02\times10^6$ is realized. The fitting results show a waveguide loss of 0.24 ± 0.01 dB/cm and a grating loss of 0.31 ± 0.01 dB/cm. By optimizing the fabrication process, the loss level is further reduced to 0.10 dB and measured Q reaches 2.3×10^6. The loss measurement limit and accuracy generally scale with the grating and waveguide loss, making this approach applicable to measure waveguide loss down to 0.001 dB/cm.

Chapter 4: Arbitrary Spiral Complex Filter for OH Emission Suppression

4.1 Background

In this chapter, I will discuss the design and characterization of a high performance integrated arbitrary filter from 1450 nm to 1640 nm. The filter's target spectrum is chosen to suppress the night-sky OH emission lines, which is critical for ground-based astronomical telescopes. This type of filter is featured by its large spectral range, high rejection ratio and narrow notch width. Historically it has only been successfully accomplished with fiber Bragg gratings. The technique we demonstrate here is proven to be very efficient for on-chip platforms, which can bring many benefits for device footprint, performance, and cost. For the design part, two inverse scattering algorithms are compared, the frequency domain discrete layer-peeling (*f*-DLP) and the time domain discrete layer-peeling (*t*-DLP). *f*-DLP is found to be superior for the grating reconstruction in terms of accuracy and robustness. A method is proposed to resolve the non-uniformity issue caused by the non-zero layer size in the DLP algorithm. The designed 55-notch filter is 50-mm-long and implemented on a compact Si_3N_4/SiO_2 spiral waveguide with a total length of 63 mm. Experimentally, we demonstrate that the device has an insertion loss as low as 2.5 dB, and that the waveguide propagation loss is as low as 0.10 dB/cm. We are also able to achieve uniform notch depths and 3-dB widths of about 28 dB and 0.22 nm, respectively.

Highly selective optical filters are fundamental building blocks for applications in many areas such as optical communications [62], [63], signal processing [64], [65],

optical sensing [66], quantum information [67], [68] and astronomy [24], [31]. Over the past decades, a lot of works in these areas have been done with fiber-optic technology, most prominently the fiber Bragg grating (FBG). With the development of fiber grating inscription methods, such as the phase mask and the direct writing technique, now people can fabricate ultra-long, complicated and accurate FBGs [69]–[71].

In recent years there has been an ever-increasing demand for on-chip optical interconnection which can realize most possible functions in a small footprint. Within these objectives, high performance on-chip arbitrary photonic filters are an important aspect [22], [72], [73]. As an example, for ground-based astronomical telescopes, several hundred lines are needed with precise positions and depths to suppress the night-sky OH emissions from the Earth's atmosphere (Figure 4.1).

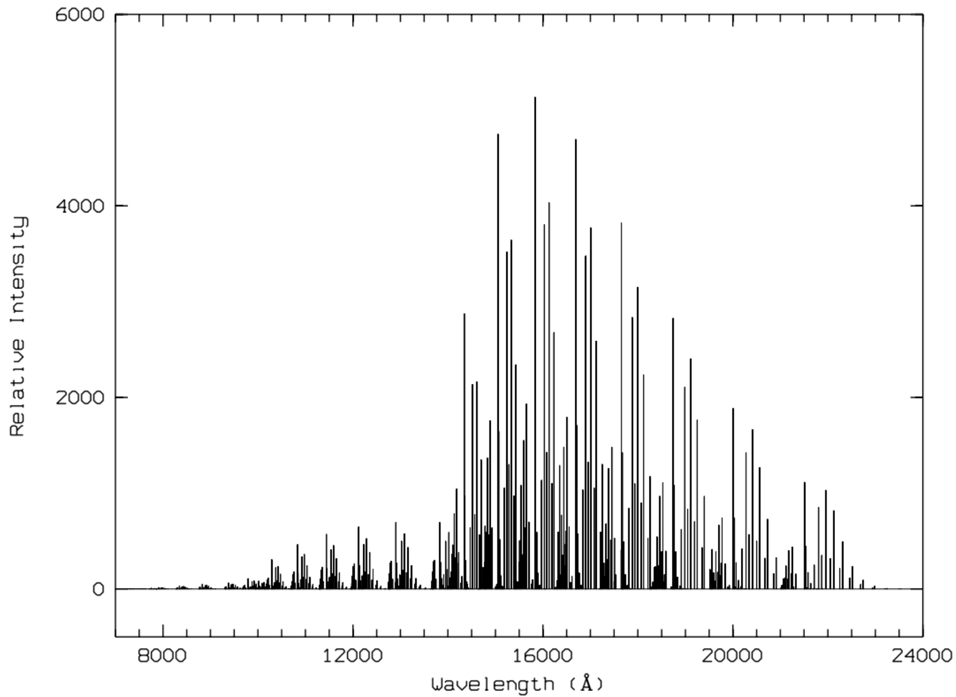

Figure 4.1 Spectrum atlas of the night-sky OH emission. [36]

These emission lines dominate the near infrared night sky spectra. They appear between 0.8 and 2.4 μm, and the brightest lines appear above 1.5 μm. The removal of these lines from the spectra is essential for ground based astronomical telescopes, because the intensities of these lines is several orders of magnitude above the sky emission from other sources. The absolute and relative intensities of these lines are strongly time dependent, caused by airflow waves in the upper atmosphere. For now, people care most about the emission lines with wavelengths below 1.7 μm. The reason is that the thermal background from the Earth's atmosphere, instrument and telescope becomes an issue beyond 1.7 μm. Besides, there is also an atmospheric cutoff from molecules in the Earth's atmosphere at 1.7-1.9 μm.

This type of OH suppression filter is characterized by its large spectral range, high rejection ratio and narrow notch width, which up to now is best achieved with complex Bragg gratings. Several studies have been carried out using FBGs to achieve this type of filter [24], [71], [74]–[76]. With the rapid advancements of various chip-based fabrication techniques, many exciting works have been done with integrated Bragg gratings [77]–[79]. However, the devices which can be used as this type of arbitrary filter are still rare. Our group is the first to demonstrate an arbitrary filter with complex waveguide Bragg grating (CWBG) on a Si_3N_4/SiO_2 CMOS compatible platform [22] . Nonetheless, there remain quite a few issues with the prototype device such as irregular notch depths, limited spectral range, and high insertion loss. These issues will severely limit our ability to put the integrated CWBG into practical use. The focus in this work is to resolve these issues and obtain a much-improved filter response.

The remainder of this chapter is organized as follows. In Section 4.2 and 4.3, we address the fundamentals of the Layer Peeling model and the optimization of the Discrete Layer Peeling algorithm. Next in Section 4.4, we discuss the details of the spiral waveguide design. Section 4.5 presents some key functions and code blocks in the MATLAB programming. Section 4.6 mostly includes the experimental results of device characterization. A brief conclusion is made in Section 4.7.

4.2 Layer Peeling Algorithm

The essence of the CWBG design is an inverse scattering (IS) problem. Intuitively the inverse scattering problem is complicated, especially compared to the direct spectrum computing from a given grating structure. However, Poladian [80] points out that the synthesis problem is actually as simple as the direct problem; one can find the grating structure from the reflection spectrum simply by propagating the fields along the grating structure, while simultaneously evaluating the grating strength using a simple causality argument. This approach is commonly known as the layer peeling algorithm [28].

Among various IS algorithms for grating reconstruction, the layer-peeling (LP) algorithm is one of the most popular because of its accuracy, robustness, and speed [28], [80]–[82]. Differentiated by the numerical implementation method, LP can be classified as discrete layer-peeling (DLP) or continuous layer-peeling (CLP). DLP is more adopted in recent works because of its high efficiency and self-consistency [28]. Furthermore, like many other electromagnetic field problems, DLP can be implemented in the frequency domain (*f*-DLP) or the time domain (*t*-DLP) [83]. The performance of both will later be discussed within our application scenario.

4.2.1 Discrete Layer Peeling (DLP)

First, we will provide a concise description of the DLP algorithm. Detailed discussions can be found in earlier works [22], [28]. DLP starts with a target spectrum which can be almost arbitrarily chosen. Then it divides a grating into N layers (also referred as pieces in this paper), with all layers having the same layer size (piece length) Δ. The whole grating has a length $N\times\Delta$ and can be reconstructed from the target spectrum with N iterations. In each iteration, the foremost layer of the remaining grating can be determined from the in-situ field by the law of causality. The next iteration is executed after the field propagate by a distance Δ and the previous layer is peeled off. The algorithm completes when the last layer is reached.

Once DLP finishes, the discrete layer adding (DLA) algorithm can be conveniently used to validate the reconstructed grating. DLA is a typical direct scattering (DS) algorithm, which is also important for filter design. However, we should mention that DLA is not a proper DS algorithm, which will be explained later in this section. A preferred DS algorithm is highly consistent with the experiment and can be used to value the performances of different IS models. In this section we use two DS models to validate our DLP. The first one is the piecewise transfer matrix T^{CMT} derived from the coupled-mode theory (CMT), with its pieces being the same as with DLP. It is the most intuitive validation model as LP is inherently based on CMT. The other one is the ABCD matrix model, in which we sample the sinusoidal-like grating into short rectangular segments, with the segment length much shorter than the grating period. The corresponding transfer matrix is derived by imposing the electromagnetic continuity conditions at segment boundaries [49]. Although this ABCD model is best

used for quasi-periodic structures, we will see later that it performs well for simulating our complex aperiodic gratings.

4.2.2 Continuous Layer Peeling (CLP)

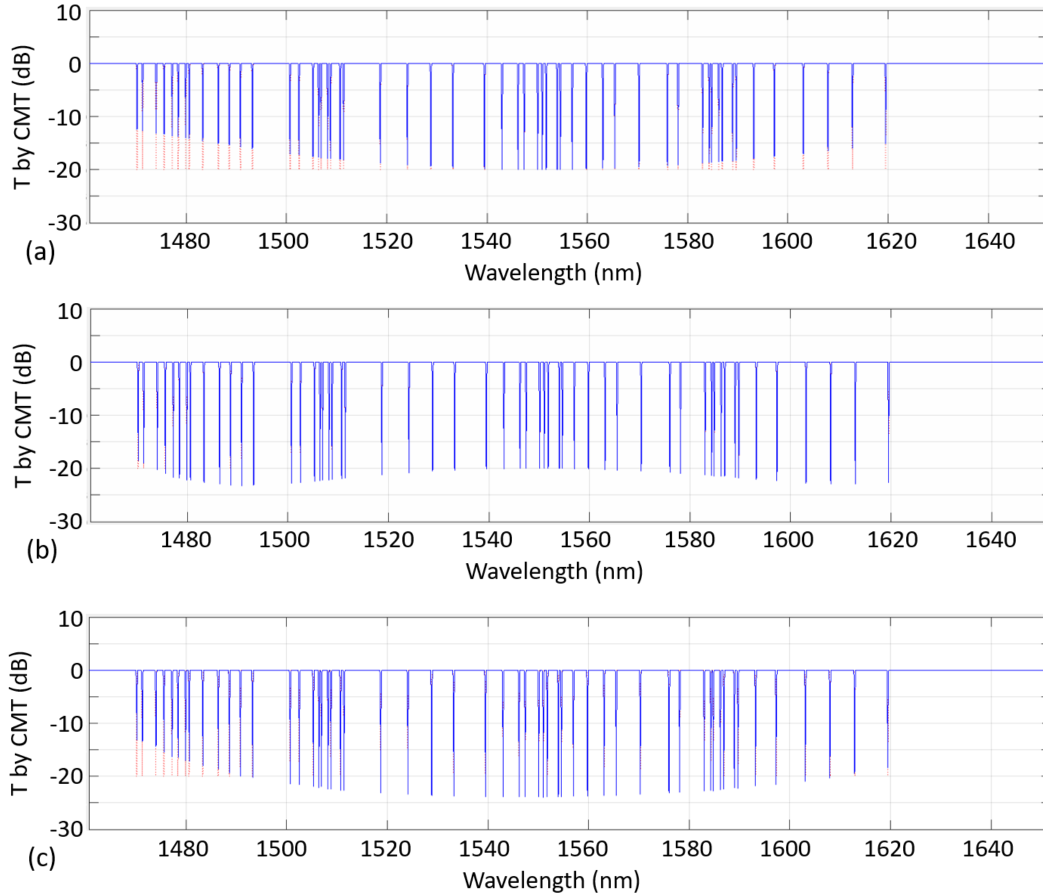

Figure 4.2 Validation results for grating designs with (a) DLP $\Delta\ =\ 4$ µm, (b) CLP $\Delta_{\mathrm{CLP}}\ =\ \Delta/2\ =\ 2$ µm, and (c) CLP $\Delta_{\mathrm{CLP}}\ = \Delta/4\ =\ 1$ µm. The target spectra (red dotted line) are the same: 55 notches with -20 dB depth. All transmissions are validated with the CMT model.

One disadvantage for DLP is that the physical model assumes that the gratings consist of discrete reflectors, which is inconsistent with the actual grating structure. On the other hand, in the CLP method, the coupling process is treated continuously, but discretization is introduced in the actual computation of the coupling coefficient and the propagation of the fields. In this case, we may think CLP could give a more accurate

result, but it turns out that the discretization step will always introduce the non-uniformity issue for the LP algorithm, which is the main topic in Section 4.3. Practically DLP is better than CLP in accuracy and robustness because it is a completely self-consistent model, although it does not match with the real world.

The CLP's algorithm implementation is quite different with the DLP, which is described in detail by Skaar [28]. For DLP, the layer size Δ is directly related with the spectral bandwidth δ_{BW} by $\delta_{BW}=\pi/\Delta$. Here we set $\Delta = 4$ μm. For CLP, however, Δ_{CLP} can be adjusted independently of δ_{BW}, which is an inherent advantage of CLP. In our simulation, it is found that Δ_{CLP} has to be set smaller than Δ, or the CLP algorithm will not converge. This phenomenon was also first noticed in [28]. It can be seen CLP and DLP give similar results, all close to but not the same with the target spectrum. If we only look at the bandwidth center, DLP is much more accurate. Besides, CLP is much more time consuming due to the smaller layer size required. As a result, the following discussions in this chapter will be focused on the DLP approach alone.

4.3 Optimization on Discrete Layer-Peeling

4.3.1 Frequency Domain and Time Domain DLP

To compare *f*-DLP and *t*-DLP, we select 55 lines and 36 lines near 1550 nm from the night-sky OH emission lines [36]. The target spectra are shown in the top two panels of Figure 4.3. They are determined by the following equations [84],

$$r_n = \frac{\sqrt{R_n}}{\cosh\{\operatorname{arcosh}(\sqrt{2}) \times [(\lambda - \lambda_n)/(w_n/2)]^2\}} \tag{4.1}$$

$$r_{\mathrm{sum}} = \left[1 - \prod_{n=1}^{N} (1 - |r_n|^2)\right]^{\frac{1}{2}} \tag{4.2}$$

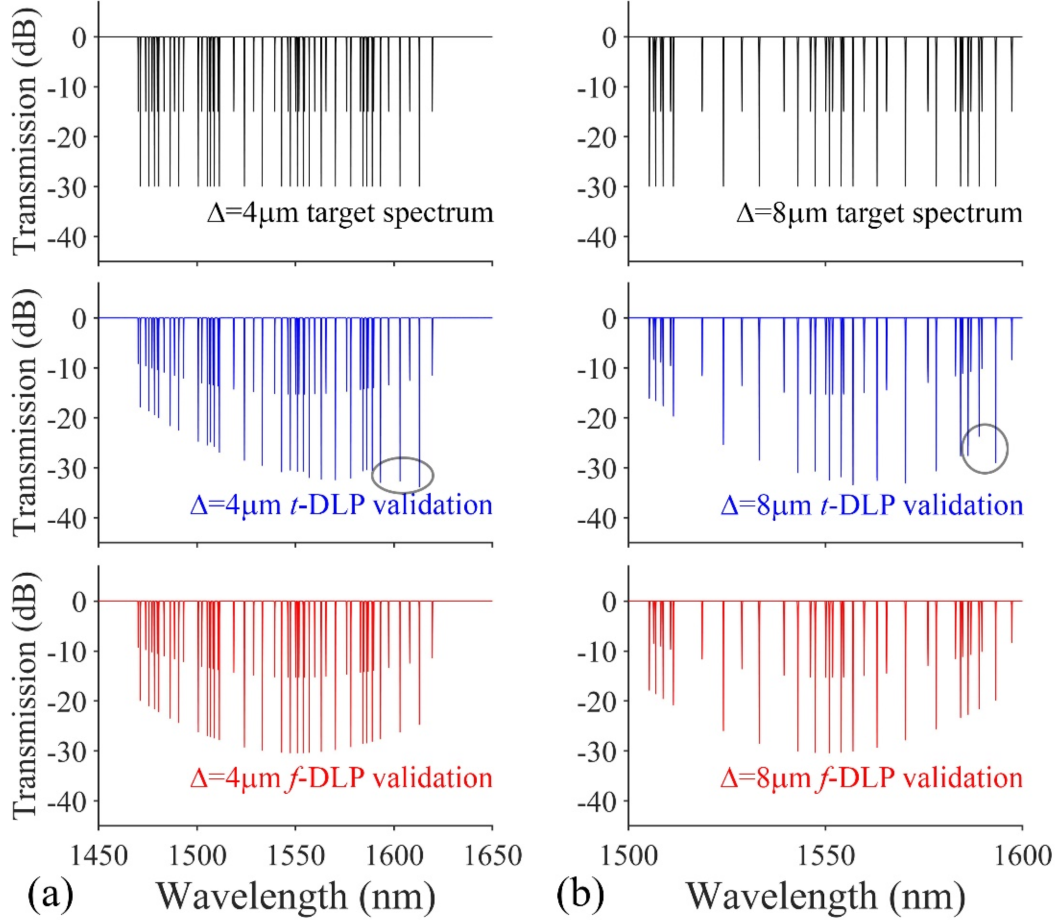

Figure 4.3 Comparison of *t*-DLP and *f*-DLP for an arbitrary filter design with 15dB/30dB alternating notch depths. (a) DLP layer size is 4 μm. (b) DLP layer size is 8 μm. Grey ovals indicate the irregular reconstructed notches in the *t*-DLP algorithm. Both *t*-DLP and *f*-DLP have the non-uniformity issue.

Here r_n is the reflection amplitude for the n-th notch with $n = 1, 2, 3\ldots N$, and r_{sum} is the total reflection amplitude. R_n is set so that the notch depths are 15 dB or 30 dB. The full width at half maximum (FWHM) w_n is set as 0.2 nm. r_{sum} is the total reflection amplitude. The layer size Δ is 4 μm in Figure 4.3(a), and is 8 μm in Figure 4.3(b). Note that Figure 4.3(b) has a narrower spectral range because the DLP algorithm's bandwidth $\delta_{\mathrm{BW}}=\pi/\Delta$.

We apply *t*-DLP and *f*-DLP to the two target spectra respectively and validate the four reconstructed gratings with the CMT model. As shown in Figure 4.3, for notches with 15 dB depth, *t*-DLP and *f*-DLP both work well. For 30 dB notches, however, *t*-DLP generates some irregularities at the longer wavelength side. It shows that *f*-DLP indeed gives more robust results. However, *t*-DLP has an edge over *f*-DLP in speed [82]. For the plots in Figure 4.3(a), the average calculating time is 5.36 s for *t*-DLP and 30.1 s for *f*-DLP. Above all, *f*-DLP is superior over *t*-DLP if precise control over individual notch lineshape is a top priority.

4.3.2 Non-Uniformity Issue

Another obvious issue in the validation plots is the non-uniform notch depths. In both *t*-DLP and *f*-DLP, the notch depths only match well with the target near the bandwidth center, and become shallower elsewhere, especially near the bandwidth boundaries. As we have mentioned, a non-zero Δ corresponds to a limited δ_{BW}. Here we choose a Δ of 4 μm, which corresponds to a wavelength span of about 190 nm. For most optical filter applications, it is much larger than the span of the target spectrum, so this issue will not be a huge concern. However, for our OH suppression filter it can cause serious performance impairment.

I would like to note that a larger spectral range is absolutely possible. For example, a bandwidth ~ 380 nm can be achieved with a Δ of 2 μm. With this, the layout design will still only take several minutes in MATLAB. However, the layout file generation time will cost much longer ~ 10 hours, which is mostly limited by FIMMWAVE. If the layout generation algorithm could optimized, such as taking advantage of CPU/GPU's

parallel computing capability, ~ μm spectral range filter design will be very reachable with a commercial PC.

We find that this non-uniformity issue is caused by the conflict between the discrete localized reflector model and the actual continuous grating structure. In the rest of this section, we will take *f*-DLP with $\Delta = 4$ μm as the example to elaborate. The target spectrum r_{sum} is sampled by M points to form a sampled target spectrum r_s. r_s and its corresponding pulse response h are a discrete Fourier transform (DFT) pair,

$$r_s(j) = \sum_{k=0}^{M-1} h(k) e^{i2\pi\cdot\delta_j\cdot k2\Delta/2\pi} \tag{4.3}$$

$$h(k) = \frac{1}{M}\sum_{j=0}^{M-1} r_s(j) e^{-i2\pi\cdot\delta_j\cdot k2\Delta/2\pi} \tag{4.4}$$

where δ_j, $j = 1, 2 \ldots M$ are equally spaced within $[-\pi/2\Delta, \pi/2\Delta] \sim [-4\times10^5, 4\times10^5]$, the detuning range of wavenumber δ. r_s should be perfectly reconstructed if M is large enough and we have the right pulse response h. To connect h with an actual grating structure, CMT transfer matrix T^{CMT} is used to analyze the field propagation. We denote q_n as the coupling coefficient of the n-th grating piece. For the target spectrum in this work, $|q_n|$ is relatively small, always less than 10^4 m^{-1}. Therefore $\delta \gg |q_n|$ for most of δ. The transfer matrix of the n-th grating piece T_n^{CMT} can then be simplified as

$$T_n^{\text{CMT}} \cong \begin{bmatrix} e^{i\delta\Delta} & q_n \sin\dfrac{(\delta\Delta)}{\delta} \\ q_n^* \sin\dfrac{(\delta\Delta)}{\delta} & e^{-i\delta\Delta} \end{bmatrix} \tag{4.5}$$

In the DLP model, the grating is assumed to consist of discrete localized reflectors. The reflector spacing corresponds to the pulse response interval. As a result, the more

accurate transfer matrix should not be T_n^{CMT}, but the product of a pure propagation matrix and a pure reflector matrix $T^{\Delta} \times T^{\rho}$, with

$$T^{\Delta} = \begin{bmatrix} e^{i\delta\Delta} & 0 \\ 0 & e^{-i\delta\Delta} \end{bmatrix} \tag{4.6}$$

$$T_n^{\rho} = \frac{1}{\sqrt{1-|\rho_n|^2}} \begin{bmatrix} 1 & \rho_n^* \\ \rho_n & 1 \end{bmatrix} \tag{4.7}$$

$$T^{\Delta} \times T_n^{\rho} \overset{|q_n\Delta| \ll 1}{\cong} \begin{bmatrix} e^{i\delta\Delta} & q_n\Delta \cdot e^{i\delta\Delta} \\ q_n^*\Delta \cdot e^{-i\delta\Delta} & e^{-i\delta\Delta} \end{bmatrix} \tag{4.8}$$

where $\rho_n = \frac{\tanh(|q_n|\Delta)q_n^*}{|q_n|}$ is the complex reflection coefficient. DLP is based on (4-3), (4-4), (4-6), (4-7), and we can see that under the discrete localized reflector assumption DLP is a very self-consistent model. In other words, the spectrum calculated by the discrete layer adding algorithm (DLA) will usually match well with the target in DLP (this is noticed but not explained in [28]). However, for an actual grating, the grating structure is continuous and T_n^{CMT} should be the transfer matrix to use for field propagation. This is the reason why non-uniformity occurs.

Our proposed method to fix this issue is explained below. When $\delta \gg |q_n|$, if we use

$$q_n^{\mathrm{adjust}} = q_n e^{i\delta\Delta} \cdot \frac{\delta\Delta}{\sin(\delta\Delta)} \tag{4.9}$$

$T^{\Delta} \times T_n^{\rho}$ becomes equal to T_n^{CMT} in (5). When $\delta \gg |q_n|$ is not satisfied, (5) will not hold. We choose the layer size Δ small enough such that $\delta\Delta \ll 1$ for these smaller δ, thus $q_n^{\mathrm{adjust}} \cong q_n$. In other words, we are not changing the original DLP near the bandwidth center, which is good because $T^{\Delta} \times T^{\rho}$ strictly equals to T^{CMT} at $\delta = 0$. As a result, the adjusted grating profile should be able to solve the non-uniformity issue.

Note that the amplitude adjustment factor in Eq. (4.9) is the reciprocal of a sinc function. However, for such a grating structure, it is very difficult to have a wavelength dependent coupling coefficient determined by Eq. (4.9). A feasible approach is to modify the target spectrum such that Eq. (4.9) "seems" to be satisfied. Specifically, with CMT we can calculate an equivalent $\tilde{q}$ according to the target notch depth and width. Next we calculate $\tilde{q}^{\mathrm{adjust}}$ from $\tilde{q}$ with Eq. (4.9) and modify each notch's depth and width in the original target spectrum according to $\tilde{q}^{\mathrm{adjust}}$. Two target spectra such modified are shown in the top of Figure 4.4. We apply *f*-DLP to them, and the CMT validation plots show that the non-uniformity indeed disappears. The ABCD validation plots below show a very similar transmission, although the notch depths are not as uniform as the CMT's (notch depths are slightly shallower at the longer wavelengths).

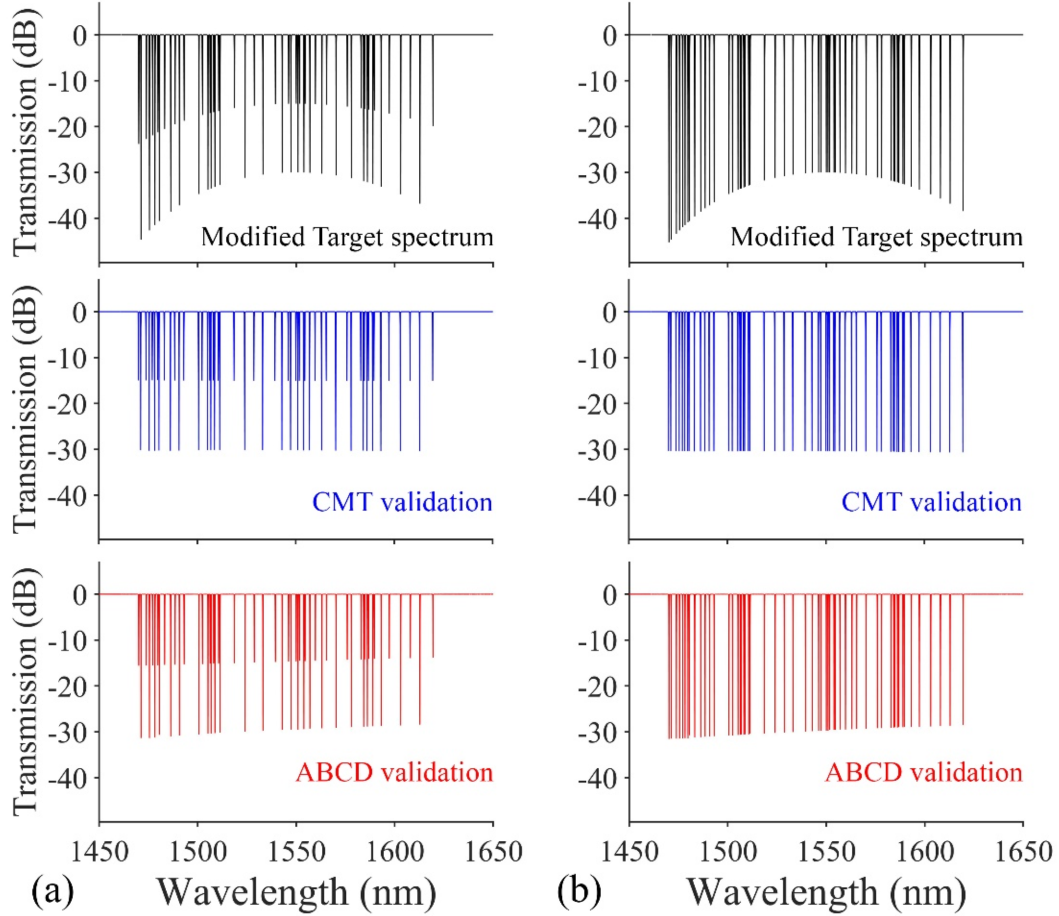

Figure 4.4 *f*-DLP modified by a sinc function for a target spectrum with (a) alternating 15dB/30dB notch depths and (b) uniform 30dB notch depths. Validation plots show that the modified *f*-DLP does not have the non-uniformity issue.

Above all, the non-uniformity issue of DLP vanishes after we resolve the conflict between the discrete model and the actual continuous grating segments. Since CLP uses T^{CMT} for a continuous coupling process, we may think that it will not have this issue. This is not true by our study, with similar non-uniformity phenomenon also found in CLP. In fact, the fundamental problem lies in the discretization process itself, which is inevitable for any numerical implementation of LP. In either DLP or CLP, the discretization process needs to assume that the grating is uniform over a certain distance, which does not fully obey causality unless $\Delta \rightarrow 0$.

4.4 Spiral Complex Grating Design

4.4.1 Spiral Curve Geometry

For the 30 dB/0.2 nm filter design we discussed in this paper, gratings of several cm or even longer are typically required. By mapping the complex grating onto a spiral waveguide structure, we can significantly reduce the footprint for better fabrication uniformity (e.g. less stitching error) and efficient chip integration. Meanwhile, we also need to carefully design the spiral structure so that it brings minimal negative impact when compared with a straight structure. Furthermore, different from a simple spiral waveguide, for the spiral complex grating design, we must consider the geometry of each grating piece and combine them together.

The Archimedean spiral is used to define the spiral curve. In a polar coordinate system, it can be written as

$$\rho = \frac{\Delta r}{2\pi}\theta \tag{4.10}$$

where Δr determines the spiral waveguide spacing. The arc length of this curve when angular coordinate goes from 0 to θ is

$$s(\theta) = \frac{\Delta r}{4\pi}\left[\theta\sqrt{1+\theta^2} + \ln\left(\theta + \sqrt{1+\theta^2}\right)\right] \tag{4.11}$$

The slope of the curve at θ is

$$m = \frac{\theta + \tan\theta}{1 - \theta\tan\theta} \tag{4.12}$$

The spiral curve geometry is determined from Eq. (4.10) and Eq. (4.11). Specifically, we design a counter-clockwise spiral and a clockwise spiral in the layout. The two spirals are connected with two half circles with radius ρ_0. ρ_0 is chosen to be

larger than the critical bending radius to avoid noticeable bending loss. Note that the grating structure is mapped onto the full curve in Figure 4.5. This full curve includes two spirals, two half circles, and two short straight regions at the input/output ends. For any required grating length, we adjust ρ_0, Δr and the length of the straight region so that a satisfactory curve is obtained.

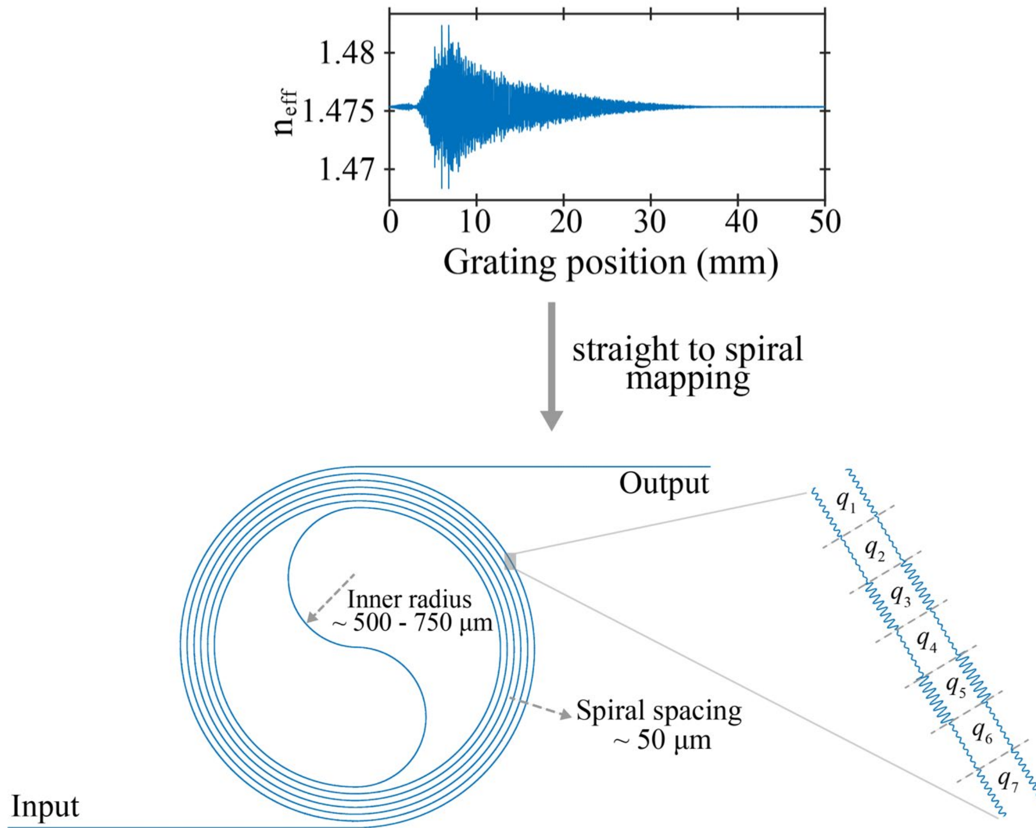

Figure 4.5 Illustration of a spiral complex grating. The top panel shows the index profile of the 50 mm grating. The bottom panel shows the whole grating, assembled by a series of layers with different coupling coefficient q_i.

Once we have the curve geometry, we discretize the continuous curve into short straight pieces. Each piece is a layer in DLP, and contains a grating structure with a uniform coupling coefficient q_i. For the design we use here, the length of each piece is Δ = 4 µm and the 50-mm-long grating corresponds to N = 12500 pieces. They are all positioned according to the starting phase θ_i and the slope m_i, with i = 1, 2, 3 … 12500.

m_i is calculated from θ_i by Eq. (4.12), and θ_i is determined by $\theta_i = \theta_{i-1} + \varphi_i$, where φ_i is the angular coordinate change brought by the *i*-th grating piece.

The grating profile calculated from *f*-DLP based on the target spectrum in Figure 4.4(b) is shown on the top of Figure 4.5. We map this 50-mm-long grating to a spiral waveguide layout in FIMMPROP with MATLAB scripting. As is illustrated, it consists of two straight regions, two Archimedean spirals and two connecting half circles. It is worth noting that this in-plane straight to curve mapping procedure is not a distance preserving transformation, and will inevitably introduce geometric errors. The inner side of the waveguide grating will suffer a length cut, while the outer side of grating will suffer a length extension. However, our experimental results in Section V show that this error is negligible for our application.

4.4.2 Mode Index's Sensitivity on Waveguide Width

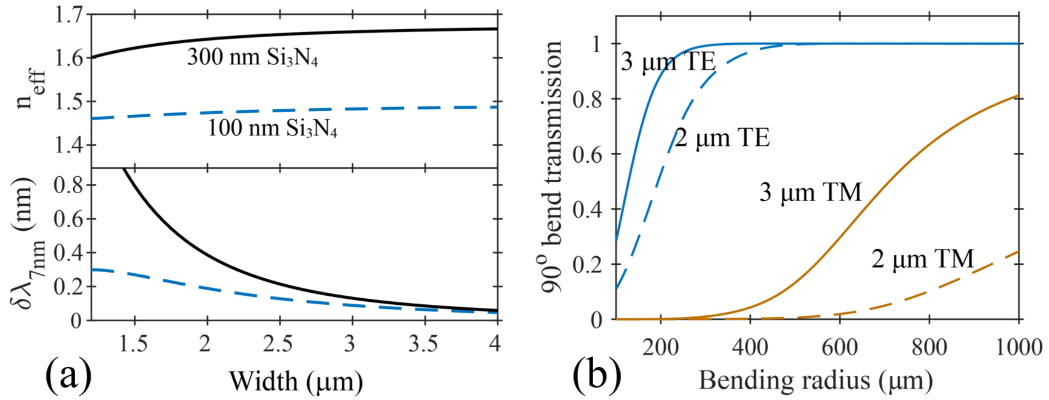

Figure 4.6 (a) Mode index study for waveguides with 100 nm and 300 nm thicknesses. (b) Simulated bending loss in TE and TM modes at 1550 nm for 3 μm x 100 nm and 2 μm x 100 nm waveguides.

As illustrated in Figure 4.5, the 50-mm-long grating device is curled to a size of 1 mm – 1.5 mm, much smaller than its fiber counterpart which typically cannot be bent. The footprint is mainly limited by the critical bending radius and can be further reduced

if we use a thicker Si_3N_4 waveguide. This can be proved from the top part of Figure 4.6(a), where we simulate the mode indices for waveguides with 100 nm and 300 nm Si_3N_4 thicknesses. Note that a higher mode index implies a stronger mode confinement.

On the other hand, there is another trade-off factor to consider when choosing the Si_3N_4 thickness. For the thicker nitride waveguide, its mode index is higher, but is also more sensitive to width variations. This is undesired for narrow filter design because for any lithography system, the minimum feature δw it can provide is limited. Here we assume that the single side width variation $\delta w/2 = 7$ nm, which is the line width limit for our Elionix electron-beam lithography (EBL) system, and denote n_1, n_2 as the mode index for width w and $w + \delta w$, respectively. For a sinusoidal Bragg grating, the notch width limit $\delta\lambda$ can be estimated as $\delta\lambda = \lambda(n_2\text{-}n_1)/(n_2+n_1)$. The simulation result is plotted in the bottom figure of Figure 4.6(a). If we want $\delta\lambda < 0.2$ nm, 300 nm thick waveguide needs to have a width over 2.6 μm, and 100 nm thick waveguide needs to have a width over 2.0 μm. Considering that the single mode width limit is ~1.3 μm for 300 nm and ~3 μm for 100 nm, the 100 nm Si_3N_4 is chosen for the final design.

4.4.3 Critical Bending Radius

Compared with a conventional straight CWBG design, the spiral design could potentially bring noticeable bending losses. In Figure 4.6(b), we simulate the transmission of TE and TM modes propagating through a 90-degree bend waveguide section in FIMMWAVE. Two Si_3N_4 core dimensions are studied: 2 μm (W) × 100 nm (H) and 3 μm × 100 nm. We will focus on the TE mode because of its stronger mode confinement and much lower bending loss [49]. In the simulation, the critical bending

radius for TE mode is about 500 μm for the 2 μm wide waveguide and 300 μm for the 3 μm wide waveguide. In the experiment, however, the critical radius will be larger due to light scattering from surface/boundary roughness.

4.5 Implementation in MATLAB and FIMMPROP

4.5.1 Key Algorithms for Inverse Scattering and Direct Scattering

In this section, four most important Matlab functions which we used for grating reconstruction are listed, including CLP, *f*-DLP, *t*-DLP for inverse scattering, and CMT validation algorithm for direct scattering.

```
%Continuous Layer Peeling Algorithm
function [ rho, q ] = Function_Layer_Peeling_CLP( N, r_initial, delta,
delta_z  )
    rho = zeros(1,N);
    q = zeros(1,N);
    r = r_initial;
    for n = 1:N
        rho(n) = mean( r ) ;
        %calculate the q function
        q(n) = -1/delta_z*rho(n)' ;
        %using CMT matrix for CLP
        gamma = 1*sqrt(abs(q(n))^2-delta.^2);
        mat_A =
cosh(gamma.*delta_z)+1i.*delta./gamma.*sinh(gamma*delta_z);
        mat_B = q(n)./gamma.*sinh(gamma*delta_z);
        mat_C = q(n)'./gamma.*sinh(gamma*delta_z);
        mat_D = cosh(gamma.*delta_z)-
1i.*delta./gamma.*sinh(gamma*delta_z);
        r_new = (mat_C+mat_D.*r)./(mat_A+mat_B.*r);
        r = r_new;
    end
end
```

```
%Discrete Layer Peeling Algorithm in Frequency Domain
function [ rho, q ] = Function_Layer_Peeling( N, r_initial, delta,
delta_z  )
    rho = zeros(1,N);
    q = zeros(1,N);
    r = r_initial;
    for n = 1:N
        rho(n) = mean( r ) ;
        r_new = exp(-1i*2*(delta )*delta_z) .* ( r - rho(n) ) ./ ( 1 -
rho(n)' * r );
        q(n) = - 1/delta_z*atanh( abs(rho(n)) ) * ( rho(n) )' /
abs(rho(n)) ;
        r = r_new;
    end
end

%Discrete Layer Peeling Algorithm in Time Domain
function [ rho, q ] = Function_Layer_Peeling_Time( N,
h_hann_and_shifted, delta_z  )
    center=round(length(h_hann_and_shifted)/2);
    h0=1*h_hann_and_shifted(center+1:center+N);
    h0(h0>0.0535)=0.0535;%A pulse response cutoff is usually needed
    rho = zeros(1,N);
    q = zeros(1,N);
    arry_U= [1, zeros(1,N-1)];
    arry_V=h0;
    fprintf('Layer peeling...');
    progress=20;
    progess_step=20;
    tic;
    for n = 1:N
        if mod(n,N*progess_step/100)==0
            fprintf([num2str(progress) '%%..']);
            progress=progress+progess_step;
        end
        rho(n) = arry_V(1)/arry_U(1) ;
        %calculate the q function
        q(n) = - 1/delta_z*atanh( abs(rho(n)) ) * ( rho(n) )' /
abs(rho(n)) ;
        arry_U = (1-abs(rho(n))^2)^(-0.5)*(arry_U-rho(n)'*arry_V);
        arry_V = (1-abs(rho(n))^2)^(-0.5)*(-rho(n)*arry_U+arry_V);
        arry_V= circshift(arry_V,-1);
    end
    time_cost=toc;
    fprintf('Time domain layer peeling time: %g s \n',time_cost);
    fprintf('Layer peeling done.\n');
end
```

```
%Validation Algorithm Based on Coupled Mode Theory
%CMT use q to simulate backward
progression=0;
percent_step=5;
ABCD_time=zeros(1,M);
MatrixCMT_N=[ones(1,M); zeros(1,M)];
Matrix_temp=MatrixCMT_N;

for count_CMT=1:partial_N
    tic;
    q_CMT=partial_q(partial_N+1-count_CMT);
    gamma=sqrt(abs(q_CMT)^2-delta.^2);
    if mod(count_CMT-1,round( partial_N *percent_step/100))==0
        fprintf('%d%% done.',progression);
        progression=progression+percent_step;

        fprintf('  Total time %g s. \n', sum(ABCD_time(1,1:count_CMT)))
    else
    end
    %TE mode
    A_CMT =
cosh(gamma.*delta_z_mod)+1i.*delta./gamma.*sinh(gamma*delta_z_mod);
    B_CMT = q_CMT./gamma.*sinh(gamma*delta_z_mod);
    C_CMT = q_CMT'./gamma.*sinh(gamma*delta_z_mod);
    D_CMT = cosh(gamma.*delta_z_mod)-
1i.*delta./gamma.*sinh(gamma*delta_z_mod);
    Matrix_temp=1./(A_CMT.*D_CMT-B_CMT.*C_CMT).*[D_CMT.*Ma-
trix_temp(1,:)-B_CMT.*Matrix_temp(2,:);-C_CMT.*Ma-
trix_temp(1,:)+A_CMT.*Matrix_temp(2,:)];
    ABCD_time(1,count_CMT)=toc;
end

Matrix_0_CMT=Matrix_temp;

reflection_CMT=Matrix_0_CMT(2,:)./Matrix_0_CMT(1,:);
angle_r_CMT=angle(reflection_CMT);

Reflection_CMT=abs(reflection_CMT).^2;

transmission_CMT=1./(Matrix_0_CMT(1,:));
angle_t_CMT=angle(transmission_CMT);
Transmission_CMT=abs(transmission_CMT).^2;
```

4.5.2 Spiral Complex Structure Realization

The final layout file of the spiral filter is generated via two consecutive steps. First, the spiral curve geometry is determined by parameters such as total length, waveguide spacing and circle radius. Second, the grating segments are assembled piece by piece in FIMMPROP, with pre-calculated positions and tangent angles.

```
% Determine Spiral Curve Structure
WF_size=250e-6;% EBL writing filed check for minimizing stitching error
Spiral_radius_step=95e-6;
Spiral_radius_0=(13+0.25)*Spiral_radius_step;%0.25 is needed to guaran-
tee the strucutre direction
Spiral_phase_0=Spiral_radius_0*2*pi/Spiral_radius_step;%Initial phase
in RAD
WF_check=2*Spiral_radius_0/WF_size;
% spiral phase calculation
% + for CW spiral, - for CCW spiral
% calculate how many turns needed for the spiral, the residual part
will be put at the ending straight WG region
% spiral eq: R(p)=deltaR/(2pi)*p. p is the phase in RAD.
% arc length: S(p)=0.5*deltaR/(2pi)*(p*sqrt(1+p^2)+log(p+sqrt(1+p^2))
Spiral_turns=1;
Spiral_s0=0.5*Spiral_radius_step/(2*pi)*(Spiral_phase_0*sqrt(1+Spi-
ral_phase_0^2)+log(Spiral_phase_0+sqrt(1+Spiral_phase_0^2)));
Spiral_s=0;%half spiral length
Spiral_length=0;%total spiral length, two half circle included
% find the maximum turns that make Spiral_length < CWBG length
temp=Spiral_phase_0;
while 1
    temp=Spiral_phase_0-Spiral_turns*2*pi;
    if temp < 0
        fprintf('Spiral setting error! \n');
        break;
    end
    %spiral_s is smallest at the beginning
    Spiral_s=Spiral_s0-0.5*Spiral_ra-
dius_step/(2*pi)*(temp*sqrt(1+temp^2)+log(temp+sqrt(1+temp^2)));
    temp_R=(Spiral_radius_step/(2*pi)*temp)/2;
    Spiral_length=2*Spiral_s+2*pi*temp_R;
    % stop at the first turns that larger than, then -1
    if Spiral_length > L_partial
        %roll back to the last one
        fprintf('%.0f turn total length: %6.3f mm. \n',Spi-
ral_turns,Spiral_length*1e3);
        Spiral_turns=Spiral_turns-1;
        temp=Spiral_phase_0-Spiral_turns*2*pi;
        Spiral_s=Spiral_s0-0.5*Spiral_ra-
dius_step/(2*pi)*(temp*sqrt(1+temp^2)+log(temp+sqrt(1+temp^2)));
        Spiral_circ_R=(Spiral_radius_step/(2*pi)*temp)/2;
        Spiral_length=2*Spiral_s+2*pi*Spiral_circ_R;
        Spiral_circ_count=round(pi*Spiral_circ_R/delta_z);
        Spiral_in_count=round(Spiral_s/delta_z);
        Spiral_start_count=round((count-Spiral_circ_count*2-Spi-
ral_in_count*2)/2);
        Spiral_end_count=count-Spiral_circ_count*2-Spiral_in_count*2-
Spiral_start_count;
        break;
    end
    Spiral_turns=Spiral_turns+1;
end
```

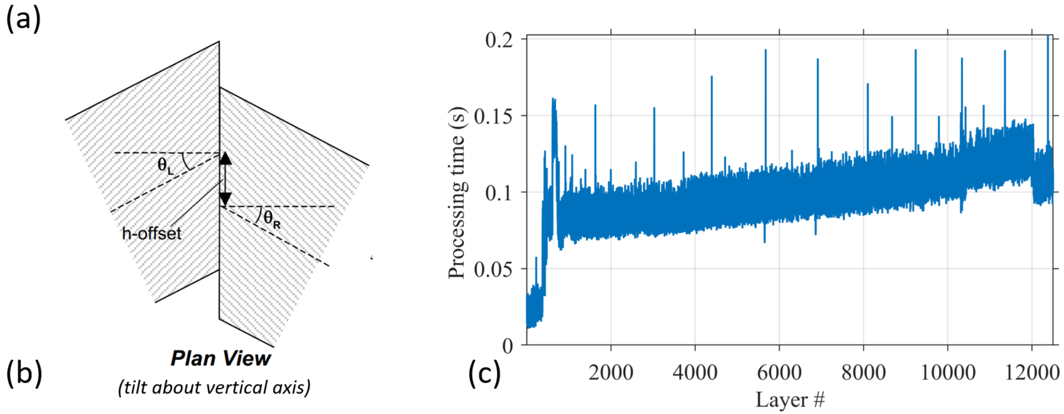

Figure 4.7 (a) Console commands for the 726-th grating section executed in FIMMPROP. (b) Plan view illustration of the section joint showing tilt angle θ_L and θ_R. (c) Assembly processing time for each grating layer (section).

In Figure 4.7(a), we show a typical block of console commands which is sent and executed to FIMMWAVE by the above MATLAB script. It includes 6 lines with explanations listed below

(1) Add a joint for the 756-th grating section

(2) Copy an unspecified grating section

(3) Insert this section after the joint

(4) Define the grating section's width profile

(5) Define left tilt angle θ_L

(6) Define right tile angle θ_R

For the 5-cm-long complex spiral grating with Δ = 4 μm which we are assembling here, there are 12500 grating pieces and 12499 joints connecting them, with a total number of elements 24999.This command block determines the 1510-th (a joint) and 1511-st (a grating piece) elements in the device. Line (1), (5), (6) determines the parameters for the 755-th joint, and line (2), (3), (4) determines the parameters for the 756-th grating

piece. There are two angles θ_L and θ_R related with section tilting, which is defined as the angle between the normal direction of joint interface and waveguide cross-section (on the left and right side). They are set equal with each other, and their sum defines the tilt between grating sections. The plan view (view of the layout as projected on a horizontal plane) illustration for their geometrical meaning is shown in Figure 4.7 (b).

4.5.3 Reducing Grating Assembly Time

Compared with our previous work on complex gratings [22], [85], I use a continuous sinusoidal structure instead of sampled discrete rectangular pieces. The sampled discretization approach was very inefficient, and led to long layout generation time. Consider the example that each 4-μm-long section is sampled with 100 nm resolution. The number of elements N_e in FIMMPROP will be 40 times of the number of grating sections N. The grating assembly time should be around O(N) (actually larger, possibly due to memory and optimization issues), which is also supported by Figure 4.7(c). This means that the 1200 s total assembly time shown in Figure 4.7(c) would become more than 13 hours.

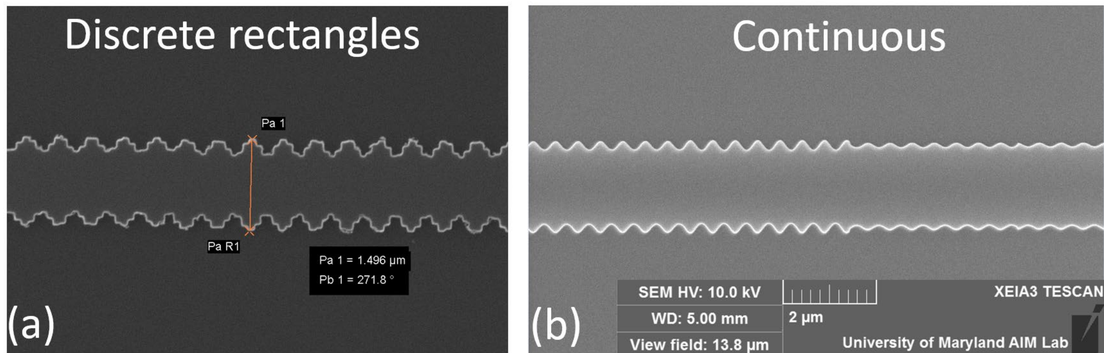

Figure 4.8 SEM of fabricated grating segments defined by the sampled discrete rectangles (a) and continuous sinusoidal expression (b).

SEM demonstrating their differences are shown in Figure 4.8. Other than the substantially reduced assembly time, this optimization made in Figure 4.8(b) makes the grating design more consistent with the DLP model. It can provide much smoother grating boundary, reduced on-chip loss, and improved spectrum accuracy. Technically, this optimization is made possible by utilizing an analytical sinusoidal expression (rather than a constant value) to define a waveguide section in FIMMPROP. As can be seen from line (4) Figure 4.7(a), the width profile for a grating section is defined as $w_n(z) = \bar{w}_n + \delta_n \cos(2\pi z/\Lambda + \phi_n)$. Here z is the curve distance measured from the start of the grating, and other coefficients are all obtained from layer peeling algorithm. This was a hidden script-only feature which I found accidentally in the older versions of FIMMWAVE. In recent versions, it can be set up in the *Path Parameters* of *Planar Section Editor.*

4.6 Experimental Results

4.6.1 Device Characterization

Limited by the field of view of SEM, we could only capture a small portion of the curved grating as shown in Figure 4.9(a). A slight bend can still be observed. Enlarged view in Figure 4.9(b,c,d) shows that the grating sidewall corrugation is well defined. Note that this figure is the same with Figure 2.6 when we discuss about ma-N EBL recipe.

We have fabricated a 55-dip CWBG spiral and a reference spiral on a single chip and the measured insertion loss is shown in Figure 4.10(a). The insertion loss is defined as the difference of the measured transmission with and without the chip coupled. This

CWBG is designed with the modified *f*-DLP with grating length 50 mm and total length 63 mm. Waveguide core dimension is 3 μm × 100 nm. This sample is also annealed at 1150 °C before EBL to get a flat transmission. The reference waveguide has an identical spiral structure as the spiral CWBG, but does not have any sidewall corrugations. For the reference spiral, the insertion loss (from input fiber to output fiber) is 1.6 dB – 2.8 dB across the full spectrum. Such a high throughput is achieved with a Nufern UHNA3 fiber, which can realize a fiber-to-chip coupling efficiency > 90% per cleaving facet [42]. For the spiral CWBG, the lowest insertion loss is 2.5 dB near 1580 nm but increases to ~ 11 dB near 1450 nm. By subtracting the lowest losses of the two spirals and dividing it by the spiral length, we obtain that the average CWBG loss is 0.18 dB/cm higher than for a uniform waveguide (~ 0.10 dB/cm from Figure 3.5). Furthermore, this sample does not exhibit any obvious non-uniformity. Most of the notch depths are around 28 dB, and all are between 25 dB and 30 dB.

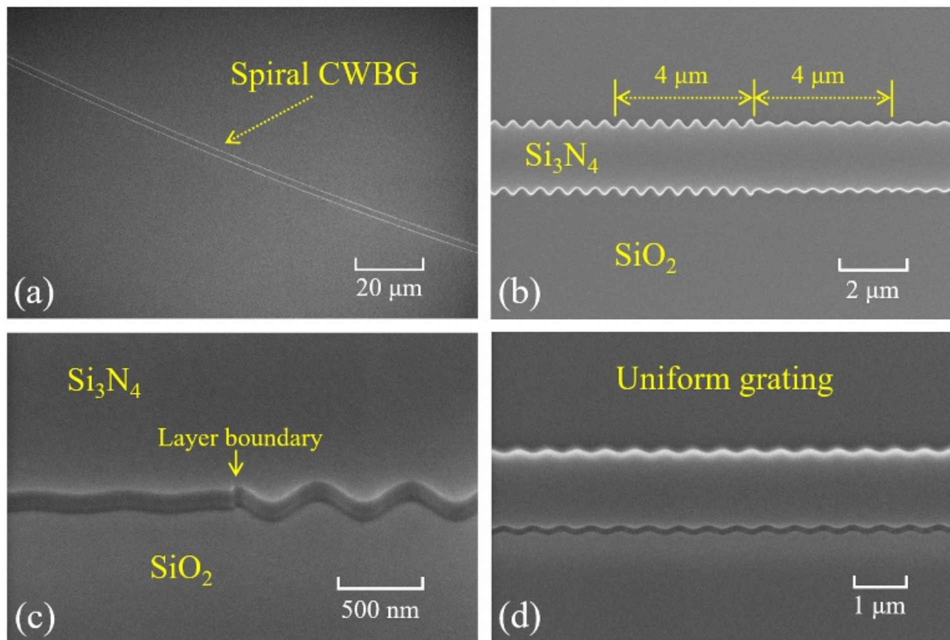

Figure 4.9 SEM of two fabricated devices. (a) A segment of the spiral CWBG. (b) Zoomed-in view of (a). (c) Tilted and further zoomed-in view of (a). (d) Tilted view of another uniform grating used as an FPBG mirror.

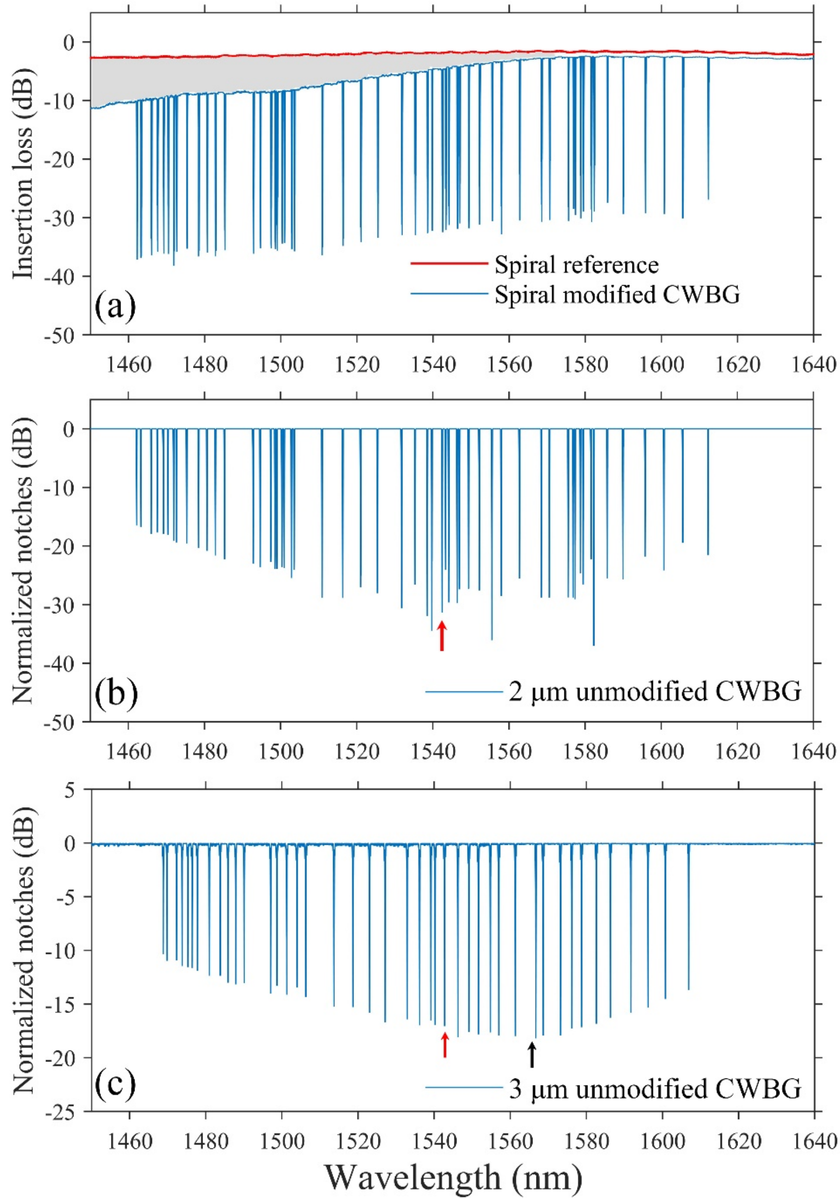

Figure 4.10 (a) Experimentally measured transmission of a reference spiral and a CWBG spiral with 3 μm average width. (b) 2 μm average width CWBG with 55-notch design showing that the deepest notches lie near the bandwidth center. (c) 3 μm average width CWBG with 43-notch design showing that the deepest notches are shifted to the right from the bandwidth center. Note that the notches in (b) and (c) are all normalized to 0 dB to compare notch depths.

As a comparison to Figure 4.10(a), we design and fabricate two spiral filters with the unmodified *f*-DLP with 2 μm and 3 μm wide waveguide, i.e without the sinc function adjustment in Eq. (4.9). The results are shown in Figure 4.10(b, c). Note that

in these two plots all notches are normalized to 0 dB so that individual notch depth can be easily compared. Both curves indeed have the non-uniformity issue. The notch bottom contour is very similar with CMT validation plots in Figure 4.3. Compared with Figure 4.10(a), it clearly shows that the non-uniformity issue can be well resolved with the sinc function adjustment. These graphs also confirm that our CMT and ABCD validation models match the actual experiment pretty well.

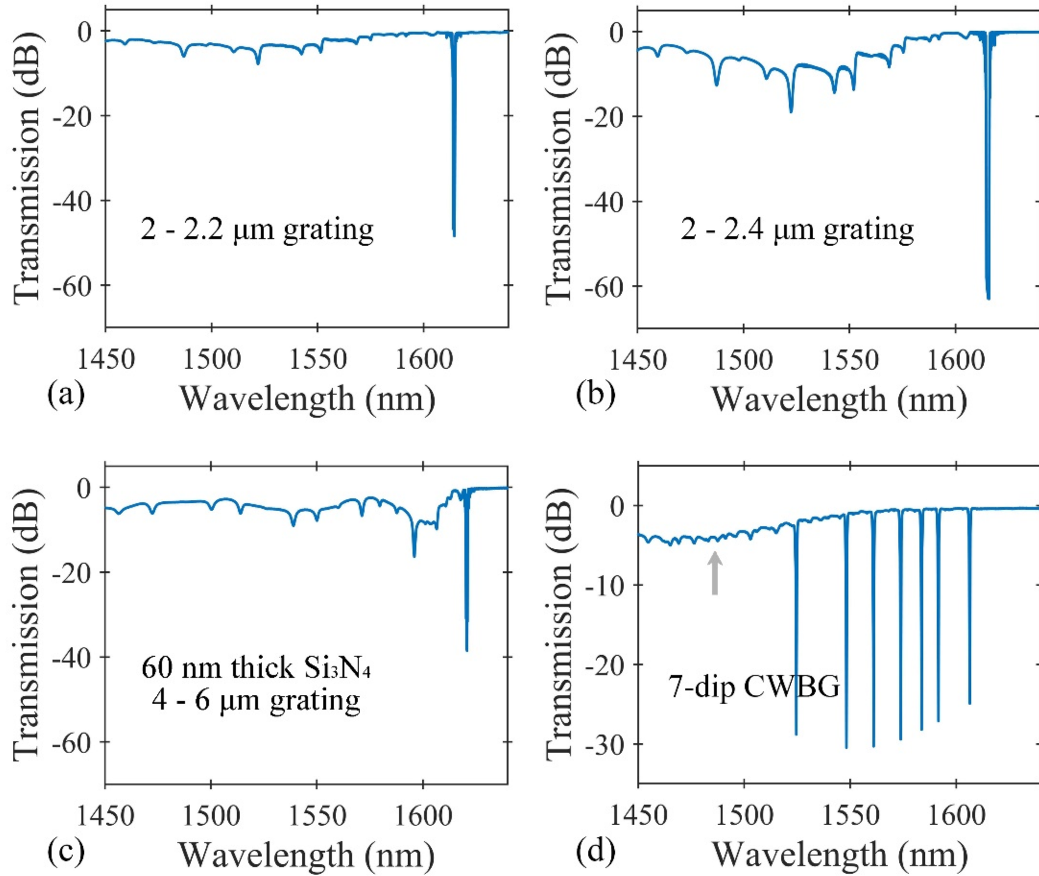

Figure 4.11 The study on cladding-mode coupling. Transmission of (a) 100 nm thick Si_3N_4 with 2 – 2.2 µm wide single-notch grating; (b) 100 nm thick Si_3N_4 with 2 – 2.4 µm wide single-notch grating; (c) 60 nm thick Si_3N_4 with 4 – 6 µm wide single-notch grating; (d) 7-notch CWBG with FWHM ~ 0.8 nm.

4.6.2 Effect from Cladding Mode Coupling

As shown in the grey region of Figure 4.10(a), there is an obvious intensity drop for the spiral CWBG transmission at shorter wavelengths. This drop pattern is mostly caused by the grating structures, more specifically the coupling between the forward guided mode and the backward cladding mode in CWBG. It is a quite common phenomenon for Bragg grating devices. It was first observed and studied in FBGs and then in SOI gratings [86]–[88]. A detailed discussion of cladding mode coupling on the Si_3N_4/SiO_2 platform can be found in our recent paper [89].

This effect will typically result in some distinct dips on the higher-frequency side of the main stopband, as seen in Figure 4.11(a, b, c), which are experimentally measured transmission for specified simple Bragg gratings. We notice that the drop pattern is more obvious for stronger gratings, and it will move closer to the main stopband when Si_3N_4 is thinner. For a CWBG, which can be regarded as a combination of some simple Bragg gratings, many more distinct dips could appear and overlap, as seen in Figure 4.11 (d). If a CWBG contains too many dips, we could see a continuous drop pattern as seen in Figure 4.10 (a).

Since cladding mode coupling could significantly decrease the complex filter throughput, for our application it is undesired and should be avoided. For CWBG in this work, one promising method might be adopting a weaker grating design. Note that even if the target spectrum is unchanged, we can still decrease the maximum grating strength by introducing different group delay terms for different notches [76]. It will stretch the pulse response h in time and lead to a longer grating in space, which needs to be considered as a trade-off factor in practice. In fact, this method assumes that for

a given target spectrum, a weaker but longer grating will introduce weaker cladding mode coupling. Although it seems to be a solid assumption, more convincing validation in both theory and experiment needs to be found. Further discussions on how to avoid this drop pattern can be found in [69], [89].

4.6.3 Effect from Waveguide Dispersion

Dispersion is always an important factor for multi-notch filter design. In our grating structure, the waveguide mode index $n_{eff}(\lambda, d)$ is a function of both wavelength λ and waveguide width d. To precisely align each notch to the target spectrum, one usually needs to take care of the first-order partial derivative $\partial n_{eff}/\partial\lambda$. If it is not accurately determined, the whole spectrum will look like expanded or compressed along the horizontal axis. Moreover, there is another effect also caused by waveguide dispersion, which is related with the second-order partial derivative $\partial^2 n_{eff}/\partial\lambda\partial d$. The fact that this derivative is not zero implies that, for a given width variation, the coupling coefficient is different for light with different wavelengths. In Table 4-1, we simulate several simple Bragg gratings designed at three different wavelengths with the rigorous coupled-mode theory (RCMT) algorithm in FIMMPROP. For 2-2.1 μm and 2.4-2.5 μm width variations, the notch depths differ by 1.1 dB and 1.3 dB. However, for 3-3.1 μm width variations, the notch depths variation can reach 3.5 dB.

	2μm - 2.1μm[a]	2.4μm - 2.5μm	3μm - 3.1μm
1450 nm	29.5 dB	29.3 dB	28.8 dB
1550 nm	29.4 dB	30.4 dB	31.0 dB
1640 nm	28.4 dB	30.6 dB	32.3 dB

Table 4-1 Grating notch depth differences caused by dispersion.
[a] denotes the widths of narrow – wide part of a simple Bragg grating.

This effect is observed in our experiments. Recall that without sinc function adjustment, the deepest notch will always lie near the bandwidth center due to the non-uniformity issue. In Figure 4.10(b, c), we mark the bandwidth center position with the red arrow. For 2 μm unmodified CWBG, the red arrow indeed corresponds to the deepest notch position. For 3 μm unmodified CWBG, however, the deepest notch position (black arrow) differ from the bandwidth center (red arrow). We should also mention that, for our waveguide configuration, this effect is generally much weaker than the non-uniformity issue.

4.6.4 Effect from Fabrication Imperfections

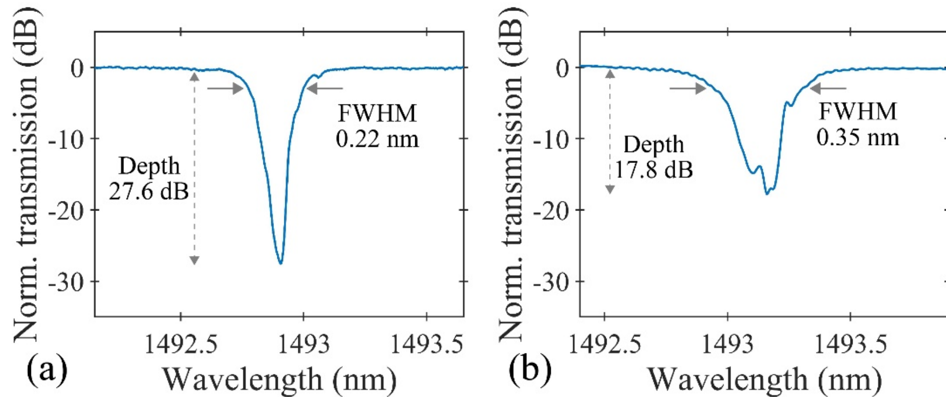

Figure 4.12 Normalized transmission of a well-defined notch and a disturbed notch. (a) The zoomed-in view of a single notch in Figure 4.10(a). (b) The transmission of a 2 μm width spiral CWBG with fabrication errors.

We characterized the notch FWHM as 0.22 nm and the notch depth as 27.6 dB from (a), which is a zoomed-in view of Figure 4.10(a). Both values are close to the target values of 0.20 nm and 30 dB, respectively. However, we notice that the notch shape errors could exist in experiment. In Figure 4.12 (b), the zoomed-in transmission of a 2 μm width spiral CWBG is shown, where the notch is shallower and wider than

designed. This effect can also be seen by comparing Figure 4.10(b) and Figure 4.10(c), where the 2 μm CWBG spectrum has more noises.

These errors are found to vary from waveguide to waveguide, even with the same design. Therefore, we attribute them to fabrication imperfections. EBL current drift, EBL beam/stage movement error or etching rate non-uniformity would all cause this type of error. A wider waveguide design would increase the device tolerance to this effect, because the mode profile of a wider waveguide is less sensitive to width inaccuracy.

Another general concern of integrated photonics platform for wavelength-sensitive applications is wavelength shift due to fabrication imperfections. The wavelength inaccuracy for our device is generally < 100 pm, similar with our previous work [22]. Part of this inaccuracy is due to the systematic error in the fabrication, which results in an overall shift of all the notches. The thermal tuning technique could help to reduce this inaccuracy. For the Si_3N_4/SiO_2 platform, this technique is mostly based on the material's thermal-optic effect [6]. For our specific waveguide configuration, much of the optical mode resides in the SiO_2 cladding, which has a thermal-optic coefficient of about 10^{-5}/K. We could derive that the required temperature variation range for a 100 pm shift would be only about 6 K.

4.7 Summary

To conclude this chapter, we have designed and characterized an on-chip arbitrary spiral filter with 55 uniform notches with insertion loss as low as 2.5 dB (throughput ~ 56%). Notch FWHMs are about 0.22 nm and depths are about 28 dB. The whole device is 63 mm long, but with a footprint of only ~ 1.5 mm thanks to the spiral design. The

filter spectral range is also broadened to over 150 nm. Suffering from the additional loss caused by cladding mode coupling at shorter wavelengths, the overall throughput from 1450 to 1640 nm decreases to 35%. This is still close to the 39% throughput achieved in the most recent OH suppression filter fabricated with FBG [71]. Compared with the typical FBG notch depth 30 dB and notch FWHM 0.2 nm, our integrated device's performance is also on the same level. On the other hand, the integrated arbitrary filter we demonstrate here has a much more compact device size and potentially much lower mass-production cost. It could also provide stronger tuning capabilities when compared to optical fiber devices.

The arbitrary filter in this work is specially designed for astronomical observations, yet its successful demonstration also paves the road for many other applications from optical communications to quantum light control. It relies on layout patterning across a long distance with sub-10 nm resolution. Coherent grating interaction over a length of 50-mm is achieved with relatively small errors. This is a very positive sign for the R&D of large-scale photonic circuits with increasing flexibility and complexity.

Chapter 5: On-chip Astronomical Spectroscopy with Arrayed Waveguide Gratings

5.1 Basic Principles of AWG

Arrayed waveguide grating (AWG), also known as PHASAR because it is based on optical phased arrays, is widely used as multiplexers, demultiplexers, and routers in optical communication systems. In astrophotonics, it can be used for on-chip spectroscopy, which is expected to play an important role in next-generation astronomical infrared spectroscopy [71], [90] for the research on exoplanets and cosmology.

A typical layout of AWG is illustrated in Figure 5.1. The light propagates from the input waveguide and diverges in the free propagation region (FPR). This diverged beam is then coupled into an array of waveguides and propagates independently in each arm of the array. For the mostly commonly used Rowland-type AWG configuration, the lengths of the array waveguides are chosen so that the adjacent waveguide's length differ by an integer multiple of the center operating wavelength divided by the effective mode index, i.e. $\Delta L = m\lambda_c/n_{\mathrm{wg}}$. At the center wavelength, the wave in each arm of the array will arrive with the same relative phase, producing a mirror image at the second FPR in the first coupler. At other wavelengths, as the field propagates along the arrays, the path length differences will cause the phase front to tilt. As a result, these wavelengths will be focused at an angle to path of the center wavelength. The output waveguides are positioned on the output start in such a way as to properly guide and confine the output light.

On the output plane of the second FPR, different orders of the spectrum overlap. For an application requiring a complete spectroscopy, these spectral orders need to be separated using a further dispersion set-up. It can be a free space cross disperser, or another on-chip grating device. For the choice of a free space disperser, the chip is cleaved at the focal plane and cross-dispersed in the perpendicular direction. For the on-chip spectroscopy design discussed in this chapter, the AWG performs fine dispersion, and the cross-dispersive optics do a coarse dispersion [90].

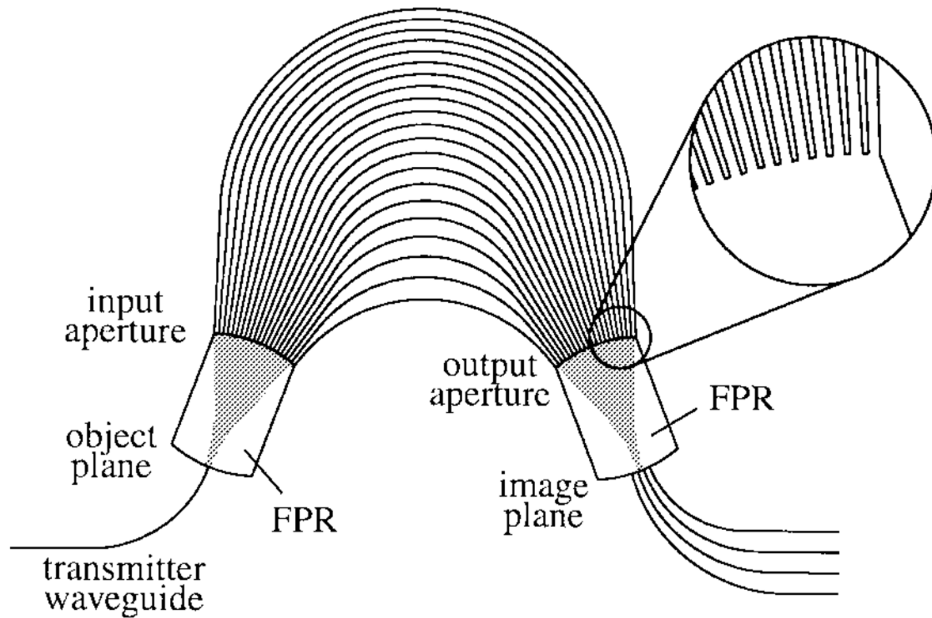

Figure 5.1 Layout of a typical AWG. Figure reproduced with permission from ref. [91], © 1996 IEEE.

In the above discussion, we mentioned a cross disperser, which is an optical module widely used in astronomical spectroscopy [92]. Traditionally, astronomers use Echelle spectrograph to obtain high-resolution spectra using the higher orders of an echelle grating. Because of the high order numbers, light from different orders overlaps in the beam dispersed by the echelle grating. In order to resolve this overlapping and achieve a large spectral range (in astronomy, $\Delta\lambda \sim \lambda$ is typically required), a lower

dispersion grating (a so-called cross disperser) that disperses light in the direction perpendicular to the dispersion direction of the echelle is used [93], [94]. The same principle holds for on-chip AWG spectrometer as well. Generally, cross disperser is a necessary part to overcome imaging problems with broadband, high-resolution spectroscopic devices.

5.2 Theoretical Framework

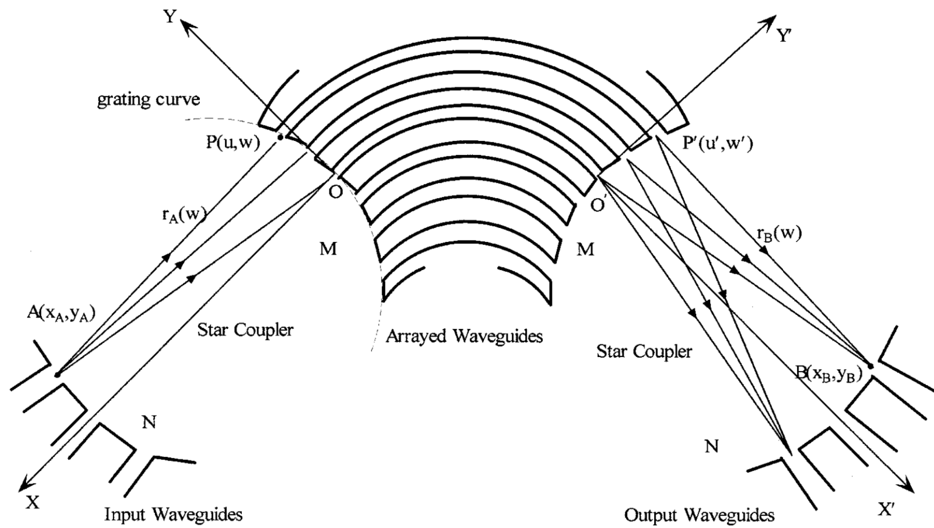

Figure 5.2 Illustration of the geometry design of an $N \times N$ AWG. Figure reproduced with permission from ref. [95], © 2001 IEEE.

In 2001, Wang et al. proposed an efficient and accurate approach to study the aberration properties of AWG [95]. The theoretical framework used in this chapter is generally based on that paper. As shown in Figure 5.2, two coordinate systems are built, XOY for the input FPR and X'O'Y' for the output FPR. The two FPRs and coordinate systems are designed to be exactly symmetrical.

Now we consider the optical path from the input waveguide at $A(x_A, y_A)$, coupled into the arrayed waveguides at $P(u, w)$, propagating through an array waveguide with

length of $L(w)$, and diffracted by the output end-face of the arrayed waveguides at P', finally reaching the focal plane at $B(x_B, y_B)$, the optical path function is

$$F(w) = n_{\text{slab}} r_A(w) + n_{\text{wg}} L(w) + G(w) m\lambda + n_{\text{slab}} r_B(w) \tag{5.1}$$

where n_{slab} and n_{wg} are the effective refractive index of the FPR and arrayed waveguide, respectively; $L(w)$ is the geometrical length of the waveguide between P and P'. The $G(w)$ term does not really exist for the actual optical path, but is added such that $F(w)$ would be a constant for different w in an aberration free optical system. $G(w)$ itself is the number of waveguides counted from the origin O to the point P; m is the grating order; $r_A(w), r_B(w)$ are the geometrical length of AP and $P'B$

$$r_A = \sqrt{(u - x_A)^2 + (w - y_A)^2}$$

$$r_B = \sqrt{(x_B - u)^2 + (y_A - w)^2}. \tag{5.2}$$

The function in 5-1 and 5-2 can all be expanded into a Taylor series,

$$\phi(w) = \phi(0) + \phi'(0)w + \phi''(0)\frac{w^2}{2} + \cdots + \phi^{(n)}(0)\frac{w^n}{n!} + \cdots \tag{5.3}$$

where $\phi = F, L, G, u, r_A, r_B$. The n-th aberration coefficient $F^n(0)$ is

$$F^n(0) = n_{\text{slab}}\left[r_A^{(n)}(0) + r_B^{(n)}(0)\right] + n_{\text{wg}} L^{(n)}(0) + G^{(n)} m\lambda \tag{5.4}$$

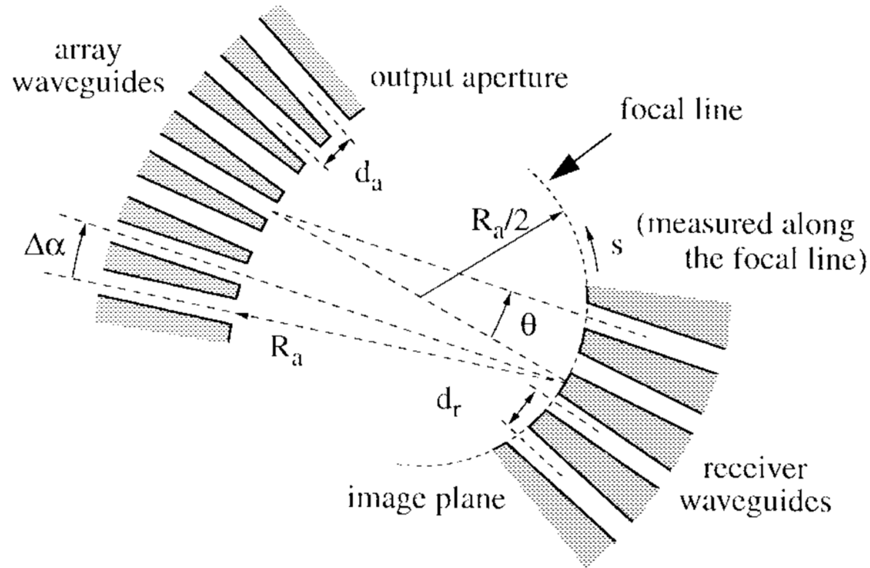

Figure 5.3 FPR region in a Rowland-type AWG. Figure reproduced with permission from ref. [91], © 1996 IEEE.

For a strictly aberration free AWG design, $F^n(0)$ needs to be zero for all $n = 1,2,3 \ldots$ However, taking the lowest few orders into consideration would be good enough for most practical applications. For example, in the Rowland-type configuration, the grating curve (u, w) is an arc centered at the input/output aperture center with radius R_a; the input/out aperture is an arc centered at the FPR center and has a radius $R_a/2$. The illustration is shown in Figure 5.3. With this design, it could be derived that $F'(0) = F''(0) = 0$ [95].

5.3 Experiment Results of Rowland-Type AWG

As we have just introduced, Rowland-type AWG can minimize the optical aberration coefficient to the 2-nd order. It is the most commonly used AWG configuration due to its convenience for both design and fabrication. Here we use the commercial photonics package Synopsys RSoft to generate a Rowland-type AWG layout with the following specifications:

- Nin = 3 (number of input waveguides)
- Nout = 5 (number of output waveguides)
- Nchan = 10 (number of wavelength channels within one FSR)
- Narray = 25 (number of arrayed waveguides)
- DLambda = 10 nm (wavelength channel spacing)
- Waveguide dimension 2 μm (3 μm) × 100 nm
- Total AWG footprint ~ 9 mm × 3 mm

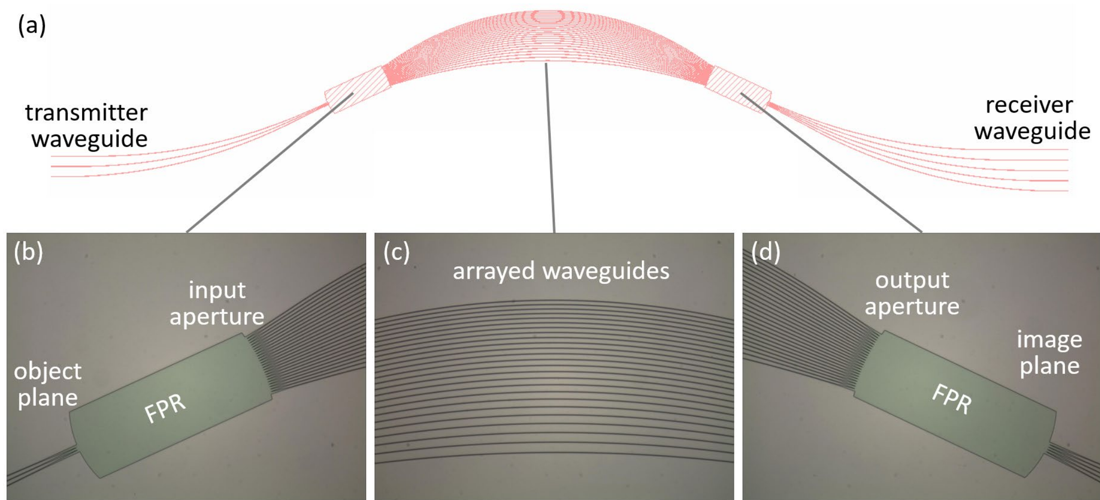

Figure 5.4 (a) A typical AWG design with dimension 2 μm × 100 nm. (b-d) Optical images of the fabricated AWG as designed in (a). Images are taken after ICP etching and before PECVD SiO_2 deposition.

The layout structure is shown in Figure 5.4(a). This device was fabricated with the 10 kV Raith EBL system with PMMA resist. Top cladding material is PECVD silane oxide. Details on the fabrication can be found in Chapter 2. The optical images of the input FPR, arrayed waveguides, and output FPR are shown in Figure 5.4(b), (c), and (d), respectively.

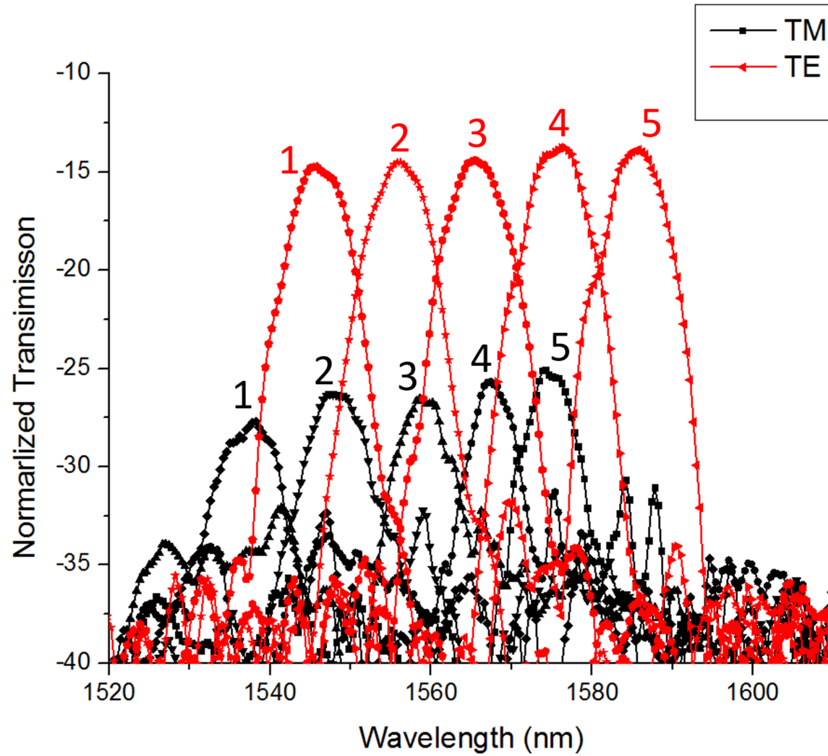

Figure 5.5 TE and TM of AWG transmission for the AWG in Figure 5.2. The waveguide dimension is 2 µm x 100 nm. 3-dB channel width is measured as 7nm.

The measurement results are shown in Figure 5.5, which is normalized with fiber to fiber coupling. PM1550-XP fiber is used for edge coupling. The fiber-to-chip coupler is not optimized for this device, resulting in a high TE (red) insertion loss -13.8 dB mostly from coupling loss from two facets. The transmission for TM mode (red) is even lower due to the TM bending loss for 100 nm SiN platform. Horizontally, the TM curve is blue shifted compared with TE for about 7 nm, which corresponds to a mode index difference for about 0.0065 RIU. The 3-dB width for each channel is also 7 nm.

5.4 Flattened Rowland-Type AWG

5.4.1 Comparison of the Standard and Flattened Rowland AWG

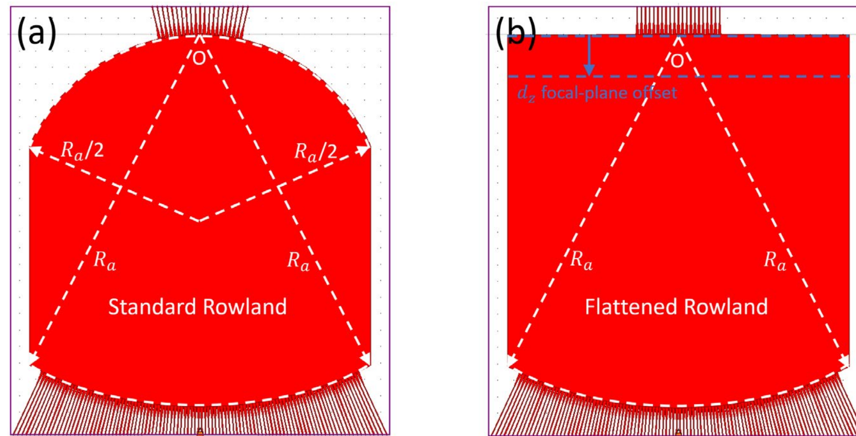

Figure 5.6 FPR layout of (a) a standard Rowland AWG and (b) a flattened Rowland AWG.

Although the Rowland-Type AWG would work well within the designed grating order, it cannot separate different orders of light. To solve this issue and obtain a large spectral range, a cross disperser is needed, which requires a flat focal-plane in the AWG design. As it is mentioned in 5.2, the output FPR of a Rowland-Type AWG is a circle with radius $R_a/2$. The simplest idea is to modify the geometry such that it is a straight line in the FPR, as shown in Figure 5.6.

These two AWG share the same parameters, except that the curvature of the output focal plane. They are both designed with the following parameters:

- Nin = 1
- Nout = 21
- Nchan = 21
- Narray = 100
- DLambda = 3.2 nm

- Dio = 5 μm (input/output waveguide spacing along the object/image plane curve)
- Darray = 4 μm (arrayed waveguide spacing along the aperture plane curve)
- Waveguide dimension 1 μm × 300 nm
- Total AWG footprint ~ 2 mm × 1.5 mm

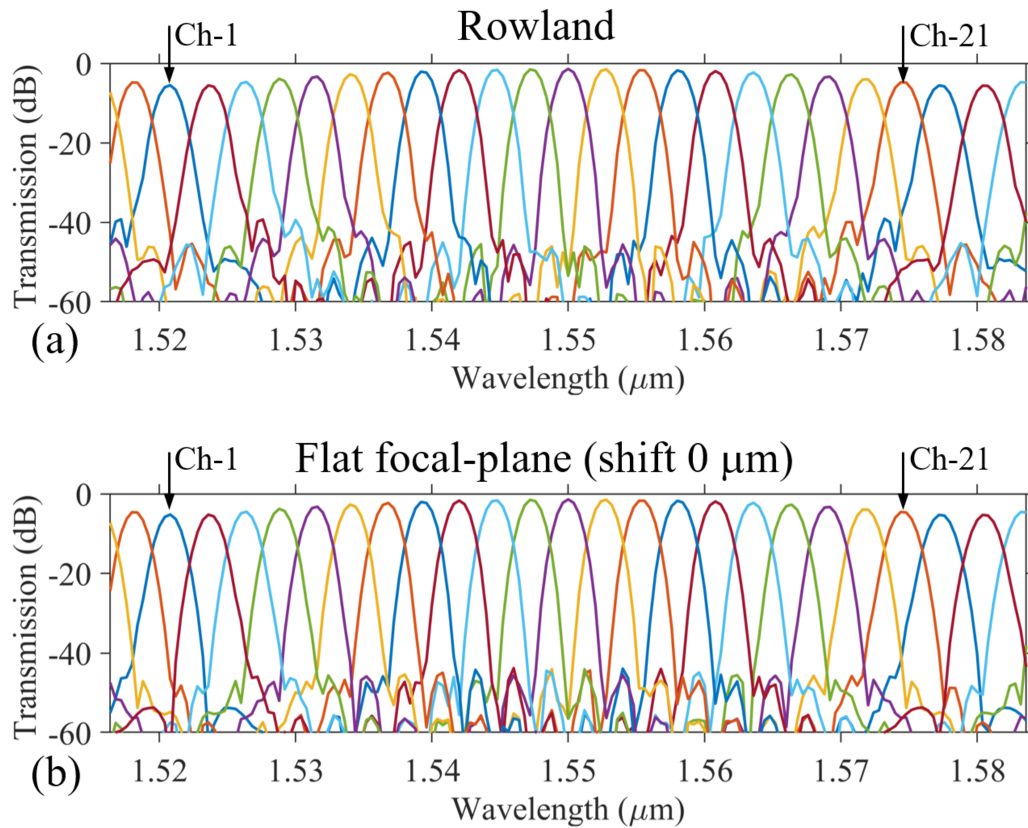

Figure 5.7 AWG simulation for (a) a Rowland-type AWG and (b) a flat focal-plane AWG. The first channel Ch-1 and the last channel Ch-21 are labeled. The two transmissions are very similar with negligible differences.

Synopsys RSoft simulation results are shown in Figure 5.7. Surprisingly, the two transmission are very similar with each other. In fact, they both have an insertion loss -1.4 dB in the center of FSR, with non-uniformity (defined as the largest insertion loss difference between different channels) -4 dB and crosstalk below -50 dB. Although the

flat focal-plane is not optimal (more details in 5.5.1), it only has 0-5 μm distance offset compared to the optimal Rowland design. Compared with the Rowland radius $R_a \sim 450$ μm, this difference is almost negligible.

5.4.2 Effect of Focal-Plane Offset

The above discussion holds for the ideal case that the focal plane can be precisely determined. In an actual experiment, we need to design a larger FPR region and try to cleave the device at the right position. Inacurate cleaving will shift the focal-plane in the positive or negative direction, as shown by the d_z term in Figure 5.6(b). The positve offset will result in a shorter FPR, and a negative offset will result in a longer FPR. Both will introduce a defocus aberration.

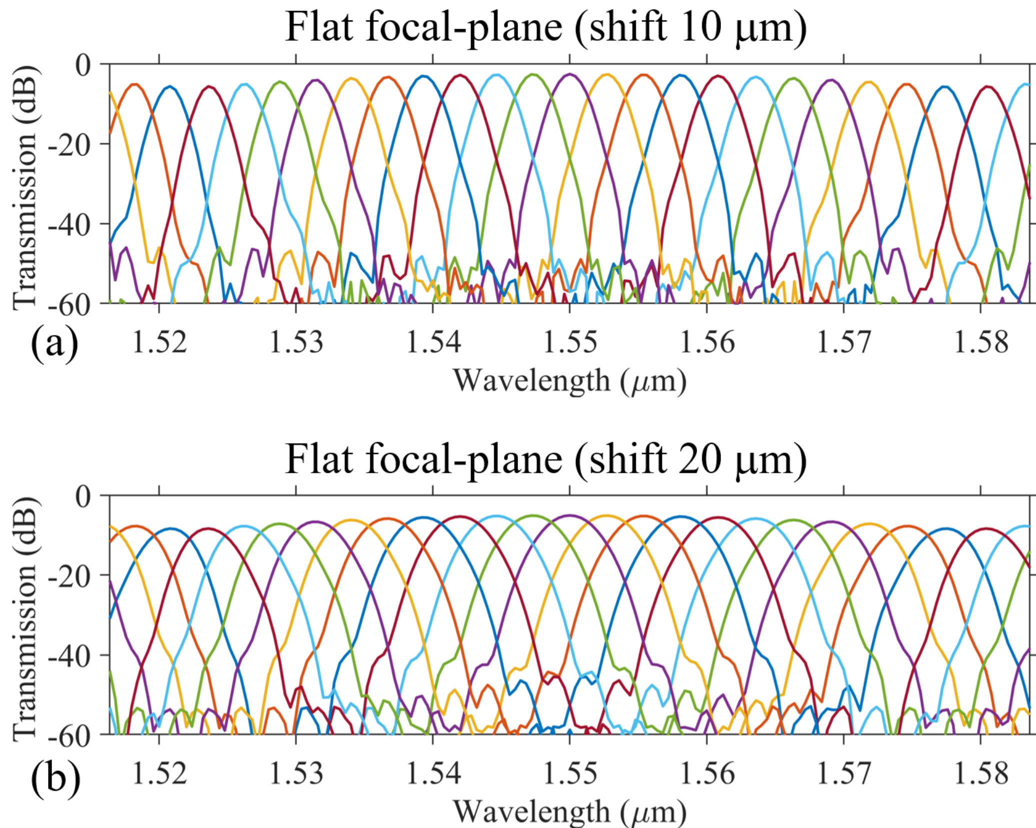

Figure 5.8 AWG simulation for a flat focal-plane AWG with shift (a) 10 μm and (b) 20 μm. The defocus aberration causes broader channel width and larger crosstalk.

As shown in Figure 5.8, the most obvious effects in transmission are the broader channel width and larger crosstalk. Besides, the insertion loss increases and the non-uniformity (see 5.4.1 for definition) slightly improves when compared with 0 μm shift design. With a +10 μm shift, we get -2.6 dB insertion loss; -21.2 dB crosstalk; -3.0 dB non-uniformity. With a +20 μm shift, we get -5.1 dB insertion loss; -7.1 dB crosstalk; -3.3 dB non-uniformity.

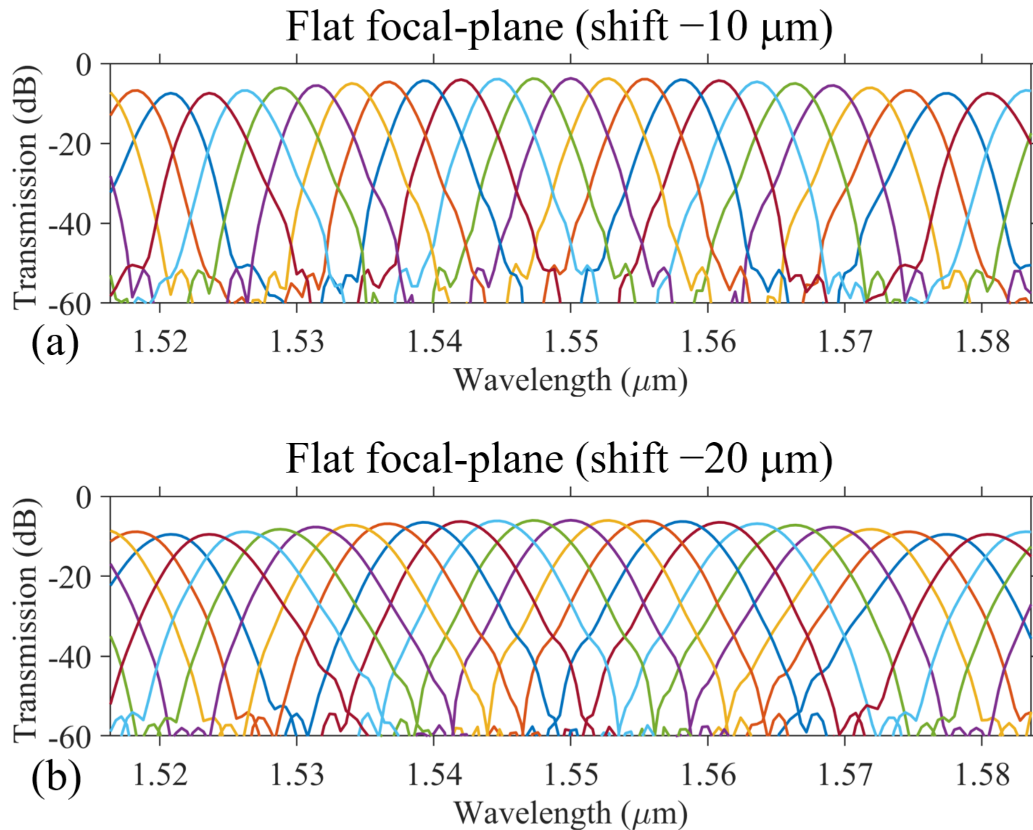

Figure 5.9 AWG simulation for a flat focal-plane AWG with shift (a) -10 μm and (b) -20 μm.

For the negative offset, the simulated transmission is shown in Figure 5.9. Similar effects are observed and larger shift comes with lower quality imaging. With a -10 μm shift, we get -3.7 dB insertion loss; -14.2 dB crosstalk; -3.7 dB non-uniformity. With a +20 μm shift, we get -6.0 dB insertion loss; -5.5 dB crosstalk; -3.5 dB non-uniformity.

It can be seen that with the same amount of offset, negative shift will have stonger effect of defocusing, which can be understood by considering the shape of Rowland circle itself.

5.5 Three-Stigmatic-Point AWG

5.5.1 Aberration Study of Rowland-Type AWG

From our discussions in 5.4, we need a cleaving accuracy within ± 10 μm to get a decent AWG with crosstalk above 15 dB. To improve the cleaving tolerance, first we can have a look at the aberration behavior of the standard Rowland-type AWG. Here we use the following AWG parameters

- Nin = 1
- Nout = 21
- Nchan = 21
- Narray = 61
- DLambda = 3.2 nm

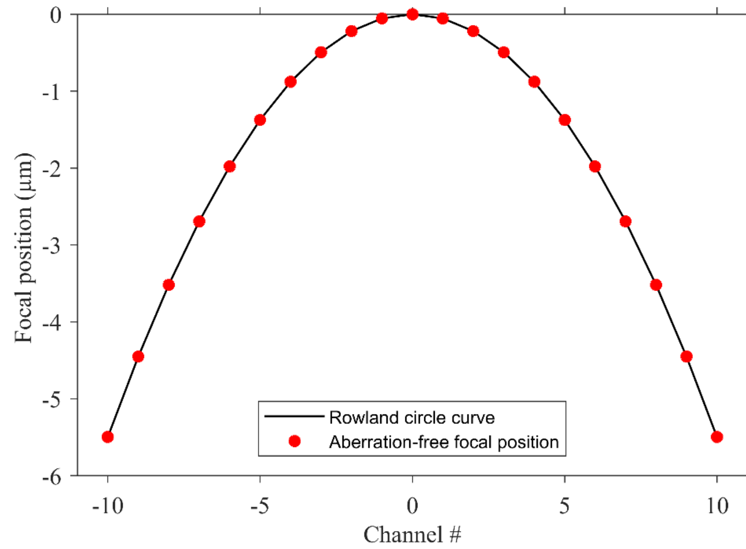

Figure 5.10 Aberration-free focal positions of the Rowland-type AWG. The aberration-free focal positions all fall on the Rowland curve.

We use the mathematical framework discussed in Section 5.2 to study the aberration behavior. The Rowland circle radius $R_a = \frac{N_s D_i D_o N_{chan}}{\lambda_c} \sim 452\ \mu\text{m}$. The aberration free focal positions are obtained for each channel's center wavelength. They are calculated based on the fact that the optical path function $F(w)$ needs to be a constant for all w along the grating curve u. The results in Figure 5.10 showed that the aberration-free focal positions all fall on the circle curve with $R_a/2$. When we flatten the curve to a straight line, as is done in 5.4, the aberration error will kick in.

5.5.2 Three-Stigmatic-Point AWG

In 2003, Lu et al. proposed a new type of AWG with 3 stigmatic points, which is based on the aberration theory [96]. In Eq. (5.1), for the given points of A and B, there are three unknow functions $u(w)$, $L(w)$, and $G(w)$. $u(w)$ determines the grating curve; $L(w)$ determines the waveguide length for arrayed waveguides; $G(w)$ determines the position of arrayed waveguides on the grating curve. As a result, a

maximum of three constraints can be added to design the AWG. For the Rowland-type AWG, the three constraints are: equal length difference between neighboring arrayed waveguides; uniformly distributed arrayed waveguide along the grating curve; one stigmatic point for $\lambda = \lambda_c$ at (X, Y) = (0, R_a). If we replace the first two constraints with $\lambda = \lambda_c - \delta\lambda$ at (X, Y) = (0, $R_a - \Delta$) and $\lambda = \lambda_c + \delta\lambda$ at (X, Y) = (0, $R_a + \Delta$), we will get 3 stigmatic points and a much more flattened aberration curve.

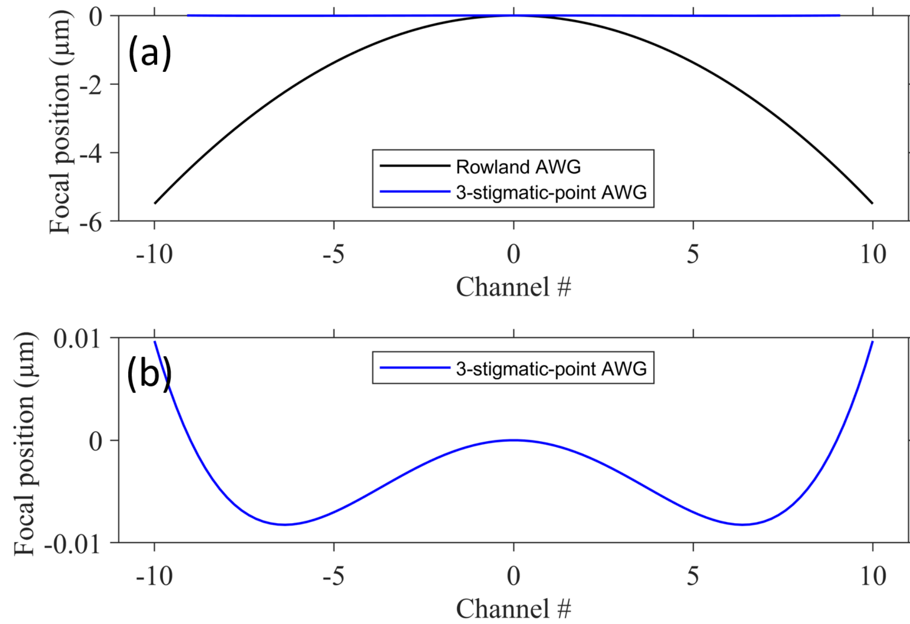

Figure 5.11 Aberration-free focal positions of the Rowland-type AWG and 3-stigmatic-point AWG.

We set $\pm\delta\lambda$ as the wavelength shift of the wavelength channel ±9, which is ±28.8 nm. Dio is set as 5 μm such that Δ is 45 μm. The Taylor series of $F(w)$, $u(w)$, $L(w)$, and $G(w)$ are all expanded to $n = 3$. The simulation results are shown in Figure 5.11(a). Compared with the Rowland AWG, the aberration curve for the 3-stigmatic-points AWG is almost 0. The enlarged view is put in (b), demonstrating a focal position range between -10 nm and 10 nm. The aberration reduction is more than 2 orders of magnitude.

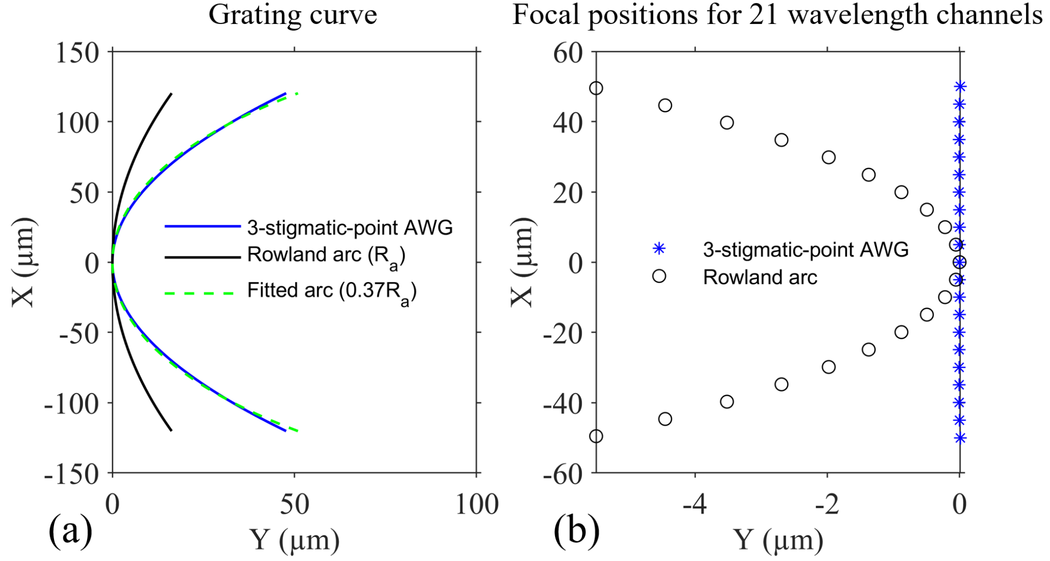

Figure 5.12 (a) Grating curve comparison in X-Y coordinate system. (b) Focal positions comparison for the center wavelength of the 21 wavelength channels.

The grating curve $u(w)$ is shown blue in Figure 5.12(a). Since we expanded the series to $n = 3$, $u(w) = u(0) + u^{(1)}(0)w + u^{(2)}(0)\frac{w^2}{2} + u^{(3)}(0)\frac{w^3}{6}$. For the symmetrical design and coordinate system considered here, it is obvious that $u(0) = u^{(1)}(0) = u^{(3)}(0) = 0$. As a result, the grating curve is a parabolic function. Its shape is close to a circular curve with radius $0.37R_a$, as shown in the green dotted plot. The black curve stands for the standard Rowland circle with radius R_a. In Figure 5.12(b), we set λ to the 21 center wavelengths for each output channel, and calculate their focal positions in X-Y for both the 3-stigmatic-point and Rowland AWG.

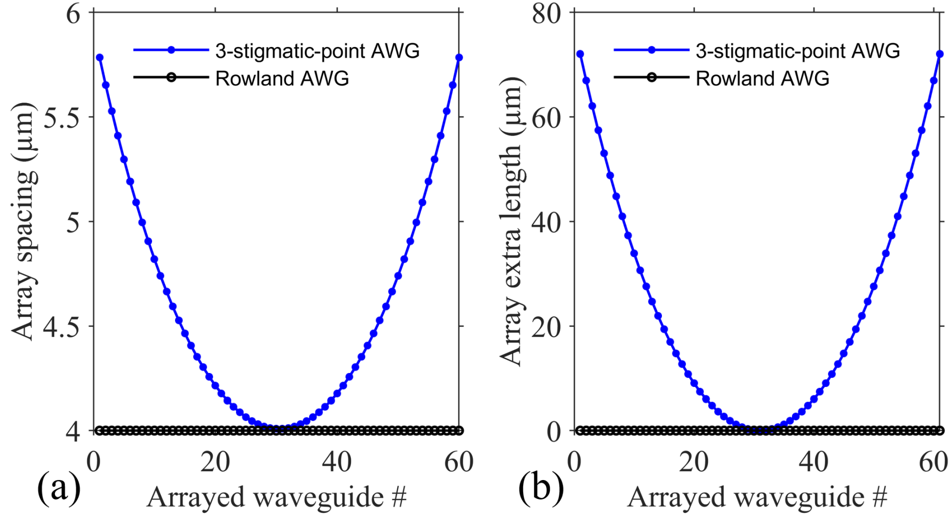

Figure 5.13 Comparison of the arrayed waveguide properties for 3-stigmatic-point (blue) and Rowland (black) AWG. (a) The distance between neighboring arrayed waveguide, measured as the curve length along $u(w)$. (b) The extra length for each arrayed waveguide, in excess of the standard Rowland length difference $\Delta L = m\lambda_c/n_{\mathrm{wg}}$.

For the other two functions $G(w)$ and $L(w)$, the 3-stigmatic-point AWG also shows significant differences. For the Rowland AWG, the arrayed waveguides are uniformly distributed along the output circle of FPR. In our design, it is set as 4 μm, as shown in the black line of Figure 5.13(a). Note that there are 60 array spacing values for the total 61 waveguides. For the 3-stigmatic-point AWG, this spacing varies from 5.8 mm to 4 mm. The smallest spacing is at the array center, and largest spacing is for the outermost waveguides. The length differences between neighboring arrayed waveguides are also not a constant anymore, as shown in Figure 5.13(b). These non-standard AWG parameters makes the layout design more difficult. In fact, Synopsys RSoft doesn't support the design for non-Rowland AWG, so we can't directly validate the transmission behavior with beam propagation method. However, from the previous aberration study, we can already conclude that the 3-stigmatic-point AWG is superior than the Rowland AWG for spectrometer applications.

5.6 Summary

In this last chapter, I discussed the basic theory and experimental demonstration of AWG based astrophotonic spectrometer. To realize a flat focal-plane AWG, two designs are proposed. The first design is based on the Rowland-type AWG and shows good performance in simulation. However, it has a strict requirement on the cleaving accuracy. The second design, on the other hand, is based on the aberration theory and is a fully customizable. It could realize 3 stigmatic points such that aberration error is minimized along a straight line.

It is worth noting that both designs cannot completely solve the optical aberration issue. Undoubtedly, the functionality of aberration correction could be incorporated into the cross-disperser. However, a chip-integrable solution is to employ active optical component for realizing a configurable focal plane. For example, micro-heaters can adjust the index of a selected region of the FPR with thermal-optic effect [97], [98]. These heaters can either be fabricated on the top cladding or be embedded by proper doping.

Chapter 6: Conclusions and Outlook

In this dissertation, I have demonstrated efforts to realize ultra-low-loss waveguide Bragg gratings on the silicon nitride platform. The lowest linear loss extracted with the Bragg grating Fabry-Perot cavity is 0.10 dB/cm, with cavity *Q* 2.3 million. Up to now, these values are the best reported for on-chip grating devices, although they are not as good as the state-of-the-art values of ring resonators, which are about 0.01 dB/cm and $Q > 10$ million. An important reason is that the Bragg grating devices inherently possess higher scattering loss than a uniform waveguide or micro-ring. However, further improvement is still possible for the waveguide grating platform. For the device design, a thicker nitride platform will allow the optical mode to be more confined inside the wavguide core and to experience less interface roughness; for the device fabrication, each step discussed in Chapter 2 can still be improved with the advancement of semiconductor manufacturing technology. It should also be noted that some low-loss fabrication method might not work well for grating devices. For example, the multi-pass EBL technique [8] is not suitable for complex structures because it will introduce additional phase variations.

The Bragg grating Fabry Perot (BGFP) cavity discussed in Chapter 3 provides an alternative approach to characterize low loss waveguide and waveguide grating devices. BGFP itself is also a unique type of on-chip high-*Q* resonator. Recently, our group has demonstrated its application in on-chip four-wave-mixing generation. Compared with the commonly used ring resonators, it has as an adjustable photonic stopband which is useful for eliminating unwanted four-wave-mixing sidebands [97].

It is envisaged that BGFP could have a great potential for entangled photon-pair generation for quantum information applications.

In Chapter 4, I focused on the study of on-chip OH suppression filters. Before our work, these filters have only been available to astronomers with FBGs. Many challenges in both the design and fabrication exist to transfer this technology to the integration platform. I have successfully realized a spiral complex WBG filter, which can match the performance of state-of-the-art FBGs. It has 55 notches from 1450 nm to 1640 nm, with uniform notch depth 28 dB and notch width 0.22 nm. The overall optical throughput is 35%, about 4.6 dB. There are still room for improvement, such as on the filter spectral range and loss. The 190 nm filter spectral range I have demonstrated is the broadest ever for a single OH emission filter. However, the target range for an ideal suppression filter is from 0.8 μm to 1.7 μm, as discussed in Section 4.1. To increase the spectral range, the easiest way is to combine several filters in series, as is used in FBG complex filters [75]. Another way is to adopt a smaller segment size in DLP algorithm (see Section 4.2), which can have a shortest grating length possible with layer peeling. For the experimental demonstrations in this dissertation, layer size is chosen as 4 μm, corresponding to the 190 nm range. Much higher layer resolution is needed to extend the range to cover for the whole OH emission band. Algorithm optimization work on the layout generation will definitely be needed, such as taking advantage of CPU or GPU's parallel computing capability.

On-chip spectroscopy is a very attractive aspect in astrophotonics. Although related topics have been extensively studied for telecommunication applications, it is still almost unexplored to achieve ultra-high resolution and ultra-broad spectral range

for on-chip astronomical spectroscopy. In Chapter 5, the design and experimental implementation of AWG spectrograph is discussed. Within our target scope, a flat image-plane AWG design is preferred, which could facilitate the coupling with free-space cross disperser or 1-D detector array. Two schemes are proposed to achieve this flat image-plane design, flattened Rowland AWG and 3-stigmatic-point AWG. 3-stigmatic-point AWG is based on the aberration study and can reduce the imaging aberration error to the minimum. The 3-stigmatic-point AWG is more complicated in geometry, and its layout design is usually not readily available with commercial solutions such as the AWG utility in Synopsys RSoft. This, however, can be resolved by developing a deeply customized AWG module with a more general process-design-kit (PDK) tool, such as Synopsys OptoDesigner. The proposed 3-stigmatic-point AWG can also improve the cleaving tolerance, but it would still require a cleaving accuracy of about 10-20 μm to not significantly impair the channel crosstalk. This accuracy is challenging but is within the capability range for a delicated silicon chip cleaving tool.

There exists another AWG design approach, which is to design the FPR such that the focal plane is sitting outside of the chip. In this case, the chip cleaving will be done before the device patterning. With a precise lithography alignment, the FPR shall be placed near the output facet. A proper design could allow the light of different wavelengths to focus in the free space. The optical path function $F(w)$ in Section 5.2 would involve another term to include the optical path in air. Thereafter, the theoretical framework discussed can be generalized and applied for this versatile design. This approach could potentially reduce the impact of cleaving-related error to the minimum.

Bibliography

[1] D. J. Moss, R. Morandotti, A. L. Gaeta, and M. Lipson, "New CMOS-compatible platforms based on silicon nitride and Hydex for nonlinear optics," *Nat. Photonics*, vol. 7, no. 8, pp. 597–607, 2013.

[2] R. Soref, "The past, present, and future of silicon photonics," *IEEE J. Sel. Top. Quantum Electron.*, vol. 12, no. 6, pp. 1678–1687, 2006.

[3] A. E.-J. Lim *et al.*, "Review of silicon photonics foundry efforts," *IEEE J. Sel. Top. Quantum Electron.*, vol. 20, no. 4, pp. 405–416, 2013.

[4] D. Thomson *et al.*, "Roadmap on silicon photonics," *J. Opt.*, vol. 18, no. 7, p. 73003, 2016.

[5] G. Cocorullo, F. G. Della Corte, and I. Rendina, "Temperature dependence of the thermo-optic coefficient in crystalline silicon between room temperature and 550 K at the wavelength of 1523 nm," *Appl. Phys. Lett.*, vol. 74, no. 22, pp. 3338–3340, 1999.

[6] A. Arbabi and L. L. Goddard, "Measurements of the refractive indices and thermo-optic coefficients of Si3N4 and SiOx using microring resonances," *Opt. Lett.*, vol. 38, no. 19, pp. 3878–3881, 2013.

[7] Y. Xuan *et al.*, "High-Q silicon nitride microresonators exhibiting low-power frequency comb initiation," *Optica*, vol. 3, no. 11, p. 1171, 2016.

[8] X. Ji *et al.*, "Ultra-low-loss on-chip resonators with sub-milliwatt parametric oscillation threshold," *Optica*, vol. 4, no. 6, pp. 619–624, 2017.

[9] T. Huffman, G. Brodnik, C. Pinho, S. Gundavarapu, D. Baney, and D. Blumenthal, "Integrated Resonators in an Ultralow Loss Si3N4/SiO2 Platform

for Multifunction Applications," *IEEE J. Sel. Top. Quantum Electron.*, vol. 24, no. 4, 2018.

[10] H. El Dirani *et al.*, "Ultralow-loss tightly confining Si3N4 waveguides and high-Q microresonators," *Opt. Express*, vol. 27, no. 21, pp. 30726–30740, 2019.

[11] Z. Ye, K. Twayana *et al.*, "High-Q Si3N4 microresonators based on a subtractive processing for Kerr nonlinear optics," *Opt. Express*, vol. 27, no. 24, pp. 35719–35727, 2019.

[12] D. T. Spencer, J. F. Bauters, M. J. R. Heck, and J. E. Bowers, "Integrated waveguide coupled Si3N4 resonators in the ultrahigh-Q regime," *Optica*, vol. 1, no. 3, p. 153, 2014.

[13] M. J. R. Heck, J. F. Bauters, M. L. Davenport, D. T. Spencer, and J. E. Bowers, "Ultra-low loss waveguide platform and its integration with silicon photonics," *Laser Photon. Rev.*, vol. 8, no. 5, pp. 667–686, 2014.

[14] H. Lee *et al.*, "Chemically etched ultrahigh-Q wedge-resonator on a silicon chip," *Nat. Photonics*, vol. 6, no. 6, p. 369, 2012.

[15] B. Little, "A VLSI photonics platform," in *Optical Fiber Communication Conference*, 2003, p. ThD1.

[16] R. Adar, M. R. Serbin, and V. Mizrahi, "Less than 1 dB per meter propagation loss of silica waveguides measured using a ring resonator," *J. Light. Technol.*, vol. 12, no. 8, pp. 1369–1372, 1994.

[17] J. F. Bauters *et al.*, "Planar waveguides with less than 0.1 dB/m propagation loss fabricated with wafer bonding," *Opt. Express*, vol. 19, no. 24, p. 24090, 2011.

[18] H. Lee, T. Chen, J. Li, O. Painter, and K. J. Vahala, "Ultra-low-loss optical delay

line on a silicon chip," *Nat. Commun.*, vol. 3, no. 1, pp. 1–7, 2012.

[19] T. Huffman, M. Davenport, M. Belt, J. E. Bowers, and D. J. Blumenthal, "Ultra-low loss large area waveguide coils for integrated optical gyroscopes," *IEEE Photonics Technol. Lett.*, vol. 29, no. 2, pp. 185–188, 2016.

[20] R. Moreira, S. Gundavarapu, and D. J. Blumenthal, "Programmable eye-opener lattice filter for multi-channel dispersion compensation using an integrated compact low-loss silicon nitride platform," *Opt. Express*, vol. 24, no. 15, pp. 16732–16742, 2016.

[21] E. F. Burmeister *et al.*, "Photonic integrated circuit optical buffer for packet-switched networks," *Opt. Express*, vol. 17, no. 8, pp. 6629–6635, 2009.

[22] T. Zhu, Y. Hu, P. Gatkine, S. Veilleux, J. Bland-hawthorn, and M. Dagenais, "Arbitrary on-chip optical filter using complex waveguide Bragg gratings," *Appl. Phys. Lett.*, vol. 108, no. 10, 2016.

[23] Y.-W. Hu, Y.-F. Xiao, Y.-C. Liu, and Q. Gong, "Optomechanical sensing with on-chip microcavities," *Front. Phys.*, vol. 8, no. 5, pp. 475–490, 2013.

[24] J. Bland-Hawthorn *et al.*, "A complex multi-notch astronomical filter to suppress the bright infrared sky," *Nat. Commun.*, vol. 2, no. 1, pp. 1–7, 2011.

[25] K. O. Hill, Y. Fujii, D. C. Johnson, and B. S. Kawasaki, "Photosensitivity in optical fiber waveguides: Application to reflection filter fabrication," *Appl. Phys. Lett.*, vol. 32, no. 10, pp. 647–649, 1978.

[26] K. O. Hill *et al.*, "Chirped in-fiber Bragg gratings for compensation of optical-fiber dispersion," *Opt. Lett.*, vol. 19, no. 17, pp. 1314–1316, 1994.

[27] M. Kulishov, J. M. Laniel, N. Bélanger, J. Azaña, and D. V Plant,

"Nonreciprocal waveguide Bragg gratings," *Opt. Express*, vol. 13, no. 8, pp. 3068–3078, 2005.

[28] J. Skaar, L. Wang, and T. Erdogan, "On the synthesis of fiber Bragg gratings by layer peeling," *IEEE J. Quantum Electron.*, vol. 37, no. 2, pp. 165–173, 2001.

[29] M. K. Smit, "New focusing and dispersive planar component based on an optical phased array," *Electron. Lett.*, vol. 24, no. 7, pp. 385–386, 1988.

[30] P. Cheben, "Wavelength dispersive planar waveguide devices: echelle and arrayed waveguide gratings," in *Optical Waveguides*, CRC Press, 2007, pp. 193–250.

[31] J. Bland-Hawthorn and P. Kern, "Astrophotonics: a new era for astronomical instruments," *Opt. Express*, vol. 17, no. 3, pp. 1880–1884, 2009.

[32] J. W. Hardy, *Adaptive optics for astronomical telescopes*, vol. 16. Oxford University Press on Demand, 1998.

[33] D. J. Schroeder, *Astronomical optics*. Elsevier, 1999.

[34] C. Lovis *et al.*, "An extrasolar planetary system with three Neptune-mass planets," *Nature*, vol. 441, no. 7091, pp. 305–309, 2006.

[35] C. H. Li *et al.*, "A laser frequency comb that enables radial velocity measurements with a precision of 1 cm s-1," *Nature*, vol. 452, no. 7187, pp. 610–612, 2008.

[36] P. Rousselot, C. Lidman, J.-G. Cuby, G. Moreels, and G. Monnet, "Night-sky spectral atlas of OH emission lines in the near-infrared," *Astron. Astrophys.*, vol. 354, pp. 1134–1150, 2000.

[37] F. G. Watson, "Multifiber waveguide spectrograph for astronomy," in *Fiber*

Optics in Astronomical Applications, 1995, vol. 2476, pp. 68–74.

[38] J. Bland-Hawthorn and A. Horton, "Instruments without optics: an integrated photonic spectrograph," in *Ground-based and Airborne Instrumentation for Astronomy*, 2006, vol. 6269, p. 62690N.

[39] N. Cvetojevic, N. Jovanovic, J. Lawrence, M. Withford, and J. Bland-Hawthorn, "Developing arrayed waveguide grating spectrographs for multi-object astronomical spectroscopy," *Opt. Express*, vol. 20, no. 3, pp. 2062–2072, 2012.

[40] T. Tsuchizawa *et al.*, "Microphotonics devices based on silicon microfabrication technology," *IEEE J. Sel. Top. quantum Electron.*, vol. 11, no. 1, pp. 232–240, 2005.

[41] Y. Saito, K. Shikama, T. Tsuchizawa, H. Nishi, A. Aratake, and N. Sato, "Tapered Self-Written Waveguide between Silicon Photonics Chip and Standard Single-Mode Fiber," in *Optical Fiber Communication Conference*, 2020, pp. W1A--2.

[42] T. Zhu, Y. Hu, P. Gatkine, S. Veilleux, J. Bland-Hawthorn, and M. Dagenais, "Ultrabroadband high coupling efficiency fiber-to-waveguide coupler using Si3N4/SiO2 waveguides on silicon," *IEEE Photonics J.*, vol. 8, no. 5, pp. 1–12, 2016.

[43] F. Duerinckx and J. Szlufcik, "Defect passivation of industrial multicrystalline solar cells based on PECVD silicon nitride," *Sol. energy Mater. Sol. cells*, vol. 72, no. 1–4, pp. 231–246, 2002.

[44] Q. Li, A. A. Eftekhar, M. Sodagar, Z. Xia, A. H. Atabaki, and A. Adibi, "Vertical integration of high-Q silicon nitride microresonators into silicon-on-insulator

platform," *Opt. Express*, vol. 21, no. 15, pp. 18236–18248, 2013.

[45] P. Gatkine, S. Veilleux, Y. Hu, J. Bland-Hawthorn, and M. Dagenais, "Arrayed waveguide grating spectrometers for astronomical applications: new results," *Opt. Express*, vol. 25, no. 15, pp. 17918–17935, 2017.

[46] C. Kaspar *et al.*, "Adjustable sidewall slopes by electron-beam exposure layout," *J. Vac. Sci. Technol. B, Nanotechnol. Microelectron. Mater. Process. Meas. Phenom.*, vol. 35, no. 6, p. 06G501, 2017.

[47] M. H. P. Pfeiffer *et al.*, "Photonic damascene process for low-loss, high-confinement silicon nitride waveguides," *IEEE J. Sel. Top. Quantum Electron.*, vol. 24, no. 4, pp. 1–11, 2018.

[48] X. Zhang, K. S. Chen, R. Ghodssi, A. A. Ayón, and S. M. Spearing, "Residual stress and fracture in thick tetraethylorthosilicate (TEOS) and silane-based PECVD oxide films," *Sensors Actuators, A Phys.*, vol. 91, no. 3, pp. 373–380, 2001.

[49] Y.-W. Hu, Y. Zhang, P. Gatkine, J. Bland-hawthorn, S. Veilleux, and M. Dagenais, "Characterization of low loss waveguides using Bragg gratings," *IEEE J. Sel. Top. Quantum Electron.*, vol. 24, no. 4, pp. 1–8, 2018.

[50] S. P. Mukherjee and P. E. Evans, "The deposition of thin films by the decomposition of tetra-ethoxy silane in a radio frequency glow discharge," *Thin Solid Films*, vol. 14, no. 1, pp. 105–118, 1972.

[51] H. Sunami, Y. Itoh, and K. Sato, "Stress and Thermal-Expansion Coefficient of Chemical-Vapor-Deposited Glass Films," *J. Appl. Phys.*, vol. 41, no. 13, pp. 5115–5117, 1970.

[52] H. K. Pulker, “Stress measurements and calculations for vacuum-deposited MgF2 films,” *Thin Solid Films*, vol. 58, no. 2, pp. 371–376, 1979.

[53] A. Shintani, S. Sugaki, and H. Nakashima, “Temperature dependence of stresses in chemical vapor deposited vitreous films,” *J. Appl. Phys.*, vol. 51, no. 8, pp. 4197–4205, 1980.

[54] I. Blech and U. Cohen, “Effects of humidity on stress in thin silicon dioxide films,” *J. Appl. Phys.*, vol. 53, no. 6, pp. 4202–4207, 1982.

[55] E. P. de Ven, I.-W. Connick, A. S. . Harrus, E. P. van de Ven, I.-W. Connick, and A. S. . Harrus, “Advantages of dual frequency PECVD for deposition of ILD and passivation films,” in *Seventh International IEEE Conference on VLSI Multilevel Interconnection*, 1990, pp. 194–201.

[56] D. Guan, A. R. Bruccoleri, R. K. Heilmann, and M. L. Schattenburg, “Stress control of plasma enhanced chemical vapor deposited silicon oxide film from tetraethoxysilane,” *J. Micromechanics Microengineering*, vol. 24, no. 2, p. 27001, 2013.

[57] K. Luke, A. Dutt, C. B. Poitras, and M. Lipson, “Overcoming Si3N4 film stress limitations for high quality factor ring resonators,” *Opt. Express*, vol. 21, no. 19, pp. 22829–22833, 2013.

[58] R. G. Walker, “Simple and accurate loss measurement technique for semiconductor optical waveguides,” *Electron. Lett.*, vol. 21, no. 13, pp. 581–583, 1985.

[59] T. Feuchter and C. Thirstrup, “High precision planar waveguide propagation loss measurement technique using a Fabry-Perot cavity,” *IEEE photonics*

Technol. Lett., vol. 6, no. 10, pp. 1244–1247, 1994.

[60] A. Grieco, B. Slutsky, and Y. Fainman, "Characterization of waveguide loss using distributed Bragg reflectors," *Appl. Phys. B*, vol. 114, no. 4, pp. 467–474, 2014.

[61] A. Yariv and P. Yeh, *Photonics: optical electronics in modern communications (the oxford series in electrical and computer engineering)*. Oxford University Press, Inc., 2006.

[62] D. Hillerkuss *et al.*, "26 Tbit s-1 line-rate super-channel transmission utilizing all-optical fast Fourier transform processing," *Nat. Photonics*, vol. 5, no. 6, pp. 364–371, 2011.

[63] K. Kikuchi, "Fundamentals of coherent optical fiber communications," *J. Light. Technol.*, vol. 34, no. 1, pp. 157–179, 2015.

[64] A. E. Willner, S. Khaleghi, M. R. Chitgarha, and O. F. Yilmaz, "All-optical signal processing," *J. Light. Technol.*, vol. 32, no. 4, pp. 660–680, 2013.

[65] W. Liu *et al.*, "A fully reconfigurable photonic integrated signal processor," *Nat. Photonics*, vol. 10, no. 3, pp. 190–195, 2016.

[66] O. Frazao, J. L. Santos, F. M. Araujo, and L. A. Ferreira, "Optical sensing with photonic crystal fibers," *Laser Photon. Rev.*, vol. 2, no. 6, pp. 449–459, 2008.

[67] N. C. Harris *et al.*, "Integrated source of spectrally filtered correlated photons for large-scale quantum photonic systems," *Phys. Rev. X*, vol. 4, no. 4, pp. 1–10, 2014.

[68] L. De Santis *et al.*, "A solid-state single-photon filter," *Nat. Nanotechnol.*, vol. 12, no. 7, pp. 663–667, 2017.

[69] J. Thomas, C. Voigtlaender, R. G. Becker, D. Richter, A. Tuennermann, and S. Nolte, "Femtosecond pulse written fiber gratings: a new avenue to integrated fiber technology," *Laser Photon. Rev.*, vol. 6, no. 6, pp. 709–723, 2012.

[70] M. Gagné, S. Loranger, J. Lapointe, and R. Kashyap, "Fabrication of high quality, ultra-long fiber Bragg gratings: up to 2 million periods in phase," *Opt. Express*, vol. 22, no. 1, pp. 387–398, 2014.

[71] S. C. Ellis *et al.*, "First demonstration of OH suppression in a high efficiency near-infrared spectrograph," *Mon. Not. R. Astron. Soc.*, vol. 2806, pp. 2796–2806, 2020.

[72] I. W. Frank, Y. Zhang, and M. Loncar, "Nearly arbitrary on-chip optical filters for ultrafast pulse shaping," *Opt. Express*, vol. 22, no. 19, pp. 22403–22410, 2014.

[73] R. Cheng and L. Chrostowski, "Apodization of silicon integrated Bragg gratings through periodic phase modulation," *IEEE J. Sel. Top. Quantum Electron.*, vol. 26, no. 2, pp. 1–15, 2019.

[74] J. Bland-Hawthorn, M. Englund, and G. Edvell, "New approach to atmospheric OH suppression using an aperiodic fibre Bragg grating," *Opt. Express*, vol. 12, no. 24, pp. 5902–5909, 2004.

[75] C. Q. Trinh *et al.*, "Gnosis: The first instrument to use fiber bragg gratings for oh suppression," *Astron. J.*, vol. 145, no. 2, 2013.

[76] A. D. A. G. Badebo, E. L. G. T. Uritsyna, and J. A. R. Ohn, "Fabrication of precise aperiodic multichannel fibre Bragg grating filters for spectral line suppression in hydrogenated standard telecommunications fibre," *Opt. Express*,

vol. 26, no. 2, pp. 165–173, 2018.

[77] A. D. Simard, Y. Painchaud, and S. LaRochelle, "Integrated Bragg gratings in spiral waveguides," *Opt. Express*, vol. 21, no. 7, pp. 8953–8963, 2013.

[78] S. Paul, T. Saastamoinen, S. Honkanen, M. Roussey, and M. Kuittinen, "Multi-wavelength filtering with a waveguide integrated phase-modulated Bragg grating," *Opt. Lett.*, vol. 42, no. 22, pp. 4635–4638, 2017.

[79] M. Ma *et al.*, "Apodized spiral Bragg grating waveguides in silicon-on-insulator," *IEEE Photonics Technol. Lett.*, vol. 30, no. 1, pp. 111–114, 2017.

[80] L. Poladian, "Simple grating synthesis algorithm," *Opt. Lett.*, vol. 25, no. 11, p. 787, 2000.

[81] R. Feced, M. Durkin, and M. Ibsen, "An efficient inverse scattering algorithm for the synthesis of the response of fibre-gratings," *IEEE J. Quantum Electron.*, vol. 33, no. 8, pp. 101–105, 1999.

[82] A. Buryak, J. Bland-Hawthorn, and V. Steblina, "Comparison of Inverse Scattering Algorithms for Designing Ultrabroadband Fibre Bragg Gratings," *Opt. Express*, vol. 17, no. 3, pp. 2040–2045, 2009.

[83] J. Skaar and R. Feced, "Reconstruction of gratings from noisy reflection data," *JOSA A*, vol. 19, no. 11, pp. 2229–2237, 2002.

[84] A. V. Buryak, K. Y. Kolossovski, J. Bland-Hawthorn, A. V. Buryak, and K. Y. Kolossovski, "Optimization algorithm for ultrabroadband multichannel aperiodic fiber Bragg grating filters," *J. Opt. Soc. Am. A*, vol. 25, no. 1, p. 153, 2008.

[85] S. Xie *et al.*, "Add-drop filter with complex waveguide Bragg grating and

multimode interferometer operating on arbitrarily spaced channels," *Opt. Lett.*, vol. 43, no. 24, p. 6045, 2018.

[86] T. Erdogan, "Cladding-mode resonances in short- and long-period fiber grating filters," *J. Opt. Soc. Am. A*, vol. 14, no. 8, p. 1760, 1997.

[87] K. O. Hill and G. Meltz, "Fiber Bragg grating technology fundamentals and overview," *J. Light. Technol.*, vol. 15, no. 8, pp. 1263–1276, 1997.

[88] T. E. Murphy, J. T. Hastings, and H. I. Smith, "Fabrication and characterization of narrow-band Bragg-reflection filters in silicon-on-insulator ridge waveguides," *J. Light. Technol.*, vol. 1, pp. 1938–1942, 2001.

[89] J. Zhan, Y. Zhang, Y. Hu, S. Xie, S. Veilleux, and M. Dagenais, "Investigation of backward cladding-mode coupling in Bragg gratings implemented on a Si3N4 waveguide platform," *J. Opt. Soc. Am. B*, vol. 36, no. 12, p. 3442, 2019.

[90] P. Gatkine, S. Veilleux, and M. Dagenais, "Astrophotonic spectrographs," *Appl. Sci.*, vol. 9, no. 2, p. 290, 2019.

[91] M. K. Smit and C. Van Dam, "PHASAR-based WDM-devices: Principles, design and applications," *IEEE J. Sel. Top. quantum Electron.*, vol. 2, no. 2, pp. 236–250, 1996.

[92] R. G. Tull, P. J. MacQueen, C. Sneden, and D. L. Lambert, "The high-resolution cross-dispersed echelle white pupil spectrometer of the McDonald Observatory 2.7-m telescope," *Publ. Astron. Soc. Pacific*, vol. 107, no. 709, p. 251, 1995.

[93] E. al Oliva *et al.*, "Concept and optical design of the cross-disperser module for CRIRES+," in *Ground-based and Airborne Instrumentation for Astronomy V*, 2014, vol. 9147, p. 91477R.

[94] R. al Follert *et al.*, “CRIRES+: a cross-dispersed high-resolution infrared spectrograph for the ESO VLT,” in *Ground-based and Airborne Instrumentation for Astronomy V*, 2014, vol. 9147, p. 914719.

[95] D. Wang, G. Jin, Y. Yan, and M. Wu, “Aberration theory of arrayed waveguide grating,” *J. Light. Technol.*, vol. 19, no. 2, p. 279, 2001.

[96] S. Lu *et al.*, “Design of flat-field arrayed waveguide grating with three stigmatic points,” *Opt. quantum Electron.*, vol. 35, no. 8, pp. 783–790, 2003.

[97] S. Xie, Y. Zhang, Y. Hu, S. Veilleux, and M. Dagenais, “On-chip Fabry-Perot Bragg grating cavity enhanced four-wave mixing,” *ACS Photonics*, vol. 7, no. 4, pp. 1009–1015, 2020.

[98] J. Sun, E. Timurdogan, A. Yaacobi, E. S. Hosseini, and M. R. Watts, “Large-scale nanophotonic phased array,” *Nature*, vol. 493, no. 7431, pp. 195–199, 2013.